INVESTIGATING HIPPOCAMPAL-NEOCORTICAL INTERACTIONS AROUND SHARP-WAVE RIPPLES

JAVAD KARIMI ABADCHI
Master of Science, Sharif University of Technology, 2013

A thesis submitted
in partial fulfilment of the requirements for the degree of

DOCTOR OF PHILOSOPHY

in

NEUROSCIENCE

Department of Neuroscience
University of Lethbridge
LETHBRIDGE, ALBERTA, CANADA

INVESTIGATING HIPPOCAMPAL-NEOCORTICAL INTERACTIONS AROUND SHARP-WAVE RIPPLES

Javad Karimi Abadchi

Date of Defence: December 14, 2021

Dr. M. Mohajerani Dr. B. McNaughton Thesis Co-Supervisors	Associate Professor Professor	Ph.D. Ph.D.
Dr. R. Sutherland Thesis Examination Committee Member	Professor	Ph.D.
Dr. D. Euston Internal External Examiner Department of Neuroscience Faculty of Arts and Science	Associate Professor	Ph.D.
Dr. G. Buzsaki External Examiner Department of Neuroscience New York University	Professor	Ph.D.
Dr. I. Whishaw Chair, Thesis Examination Committee	Professor	Ph.D.

DEDICATION

To my family for their unbounded love and support.

ABSTRACT

Coordinated activity in the hippocampal-neocortical network around hippocampal sharp-wave ripples (SWRs) plays an instrumental role in memory processing in the brain. SWRs occur in both sleep and awake states, though under two significantly different behavioural and chemical circumstances. Previous studies have reported different patterns of peri-SWR neocortical modulations between these states; however, their findings have been limited to one or a few discrete regions of the neocortex. To extend previous findings, we conducted wide-field optical imaging of the mouse neocortical voltage and glutamate activity combined with hippocampal electrophysiological recording. We found topographically- and temporally-organized patterns of neocortical glutamate and voltage activity around sleep and awake SWRs, though with pronounced differences. These findings highlight the state-dependency of the hippocampal-neocortical network's computations and possibly functions. Moreover, they provide a spatiotemporal map of the neocortex around SWRs that could guide future studies on the role of hippocampal-neocortical interactions in memory consolidation.

PREFACE

The work presented in chapters 2 and 3 have been conducted in Dr. Mohajerani's and McNaughton's laboratories at Canadian Centre for Behavioural Neuroscience. The work in chapter 2 has been published in the journal of eLife (eLife 2020;9:e51972), and the work in chapter 3 is being prepared as a manuscript to be submitted to a decent journal in near future. I have been the sole lead author on both manuscripts. I have designed both studies with help from my advisers, collected the majority of the data, analyzed the data, prepared figures, written the first version of the manuscripts, and addressed the reviewer's comments.

ACKNOWLEDGEMENT

I would like to thank my supervisors Drs. Majid Mohajerani and Bruce McNaughton for their support and encouragement throughout my Ph.D. journey. I would also like to thank my Ph.D. committee members, Dr. Masami Tatsuno and Dr. Robert Sutherland, as well as my thesis examination committee members, Dr. David Euston, Dr. Gyorgy Buzsaki, and Dr. Ian Whishaw, for their constructive feedback on my dissertation.

I am deeply grateful for being fortunate to have the opportunity to work with excellent colleagues and collaborators whose names are listed below:

Dr. Sandra Gattas, Dr. Zahra Rezaei, Dr. Michael Eckert, Dr. Edgar Bermudez-contreras, Dr. Jianjun Sun, Mojtaba Nazari MSc, Milad Naghizadeh MSc., Dr. Sam Inayat.

TABLE OF CONTENT

LIST OF FIGURES

LIST OF ABBREVIATIONS

RSCd	Dorsal retrosplenial cortex
aRSC	Agranual retrosplenial cortex
mPFC	Medial prefrontal cortex
HPC	Hippocampus
NTCX	Neocortex
AI	Asymmetry index
QR	Quartile range
LFP	Local field potential
MUA	Multi-unit activity
SWR	Sharp-wave ripple
SVD	Singular value decomposition
VSFP	Voltage-sensitive fluorescent protein
SEM	Standard error of the mean

1. General Introduction

1.1. Theoretical foundations

The theoretical roots of this dissertation lie in two pioneering theories/models, hippocampal memory indexing theory (T J Teyler and DiScenna, 1986) and two-stage model of memory formation (Buzsáki, 1989), whose substrates could be found in theories of memory consolidation (Buzsáki, 2015; Goode et al., 2020; McClelland et al., 1995; Teyler and Rudy, 2007). In the following subsections, I briefly introduce these theories.

1.1.1. Hippocampal memory indexing theory

Hippocampal memory indexing theory assumes that experiencing an event is represented in spatiotemporal patterns of activity among neocortical modules, the smallest units of information processing, as well as among other brain structures. These patterns of activity hierarchically converge to the hippocampus through the association, perirhinal and entorhinal cortices. The theory proposes that the hippocampus's role in memory is to generate and store an index code, using synaptic plasticity mechanisms, that maps the sequential order of activation of all the neocortical and other brain structures (i.e. spatiotemporal patterns of brain activity) evoked by the experience. Indeed, the hippocampus maps the cortical activation space. Recent data on structural connectivity of the hippocampus and the neocortex suggest that the hippocampus accesses the neocortical patterns of activity via a hierarchy of association areas (Lavenex and Amaral, 2000). From this angle, the hippocampus could be seen as an "association cortex for association cortices" that indexes association cortices indexing the rest of the neocortex. Thus, according to the theory, no content of the experience is encoded and stored in the hippocampus, and the memory trace is nothing but the index code.

The theory asserts that spontaneous reactivation of a hippocampal memory index evokes the neocortical representation of the indexed experience that could lead to retrieval of the experience memory. Furthermore, after an index is formed and stored in the hippocampus, a partial reactivation of the neocortical representation of the corresponding experience provided that it is complete enough to activate a sufficient portion of the index code in the hippocampus leads to complete activation of the code (this process is called pattern completion), which in turn, invokes the complete neocortical representation of the experience.

Motivated by explaining the observation of intact remote memories in patient HM (Scoville and Milner, 1957), the theory suggested that the repeated reactivation of hippocampal indices might have a "slowly incrementing effect" on the neocortical modules they map, in a way that the neocortex gradually becomes capable of "auto-indexing", i.e. the capability of retrieving the experience-activated spatiotemporal patterns of activity on its own and independent of the hippocampus. Therefore, according to the theory, repeated reactivation of hippocampal indices is crucial for the consolidation of memories in the neocortical networks. Such reactivations could be initiated by re-exposure to or by the replay of the event during offline periods like quiet wake or sleep. Indeed, for the neocortical "auto-indexing" to possibly occur, multiple re-exposures, distributed in time, and/or multiple bouts of replay might be required (Sutherland et al., 2010).

The hippocampal memory indexing theory proposed that the main candidate mechanism for the formation of the index codes is the long-term synaptic potentiation (LTP). Since synaptic potentiation induced by LTP decays over time, the index codes were predicted to gradually decay if they were not repeatedly reactivated. This prediction bolds the role of memory reactivation during offline periods for maintenance of the hippocampus-dependent memories.

1.1.2. Two-stage model of memory formation

The theory of hippocampal memory indexing theory was proposed mainly based on known hippocampus anatomy, structural connectivity of the hippocampus with neocortical and subcortical regions, and synaptic physiology of the hippocampus (Teyler and Rudy, 2007). Thus, the theory did not attempt to provide neurophysiological details about its proposed thesis. Such details were provided by another theory, called the two-stage model of memory formation (Buzsáki, 1989), which was proposed shortly after the publication of the indexing theory. This new theory utilized the correspondence between neurophysiological signatures of the hippocampal network activity and behavioral state of animals. During active explorative behavior (preparatory behavior; first stage), the hippocampus shows a rhythmic activity called theta rhythm (4-10 Hz) which modulates a concurrently-occurring faster rhythm, called gamma (40-100 Hz). On the other hand, during consummatory behaviours (second stage), such as eating and grooming, as well as during slow-wave sleep, the hippocampus shows a haphazard pattern of activity, called large irregular activity (LIA), during which intermittent bursts of neuronal firing occurs. Such intermittent bursts, called sharp-waves, play the central role in the two-stage theory.

The theory posits that, during learning, the neocortical representations of the experience reach the hippocampus via the neocortex/entorhinal cortex, and modify the synaptic matrix of the CA3 collaterals. Later during consummatory behavior or slow-wave sleep, sharp-waves are spontaneously initiated in CA3, mainly by the same neurons whose synaptic connections were modified during the encoding phase, and spread throughout the CA3 via the collateral connections. These activity waves exert strong excitatory drives on both pyramidal neurons and interneurons in CA1 which leads to the generation of a high-frequency (150-250 Hz) transient pattern, called ripple. Ripples, in turn, potentiate the neocortical neurons mainly via the subiculum. According to

the theory, the sharp-wave ripple (SWR) complexes that occur in both awake and sleeping states, are the main candidate for consolidating memories by reconfiguring synaptic connectivity of the recipient neocortical circuits (Buzsaki, 1998; Buzsáki, 1996).

There are important points in the theory that are worth being emphasized. First, the CA3 subfield of the hippocampus plays a key role in storing and retrieving mnemonic information, brought about by the neocortex into the hippocampus. The storage and retrieval capabilities of the CA3 are attributed to its vast recurrent synaptic connections which endow the CA3 with auto-associative property (McNaughton and Morris, 1987). Auto-associative networks are able to store patterns and retrieve them even if the stored patterns are partially presented. The process of retrieving a complete pattern starting from a partial version is called pattern completion (McNaughton and Morris, 1987). The auto-associativity and pattern completion property of the CA3 network are the main reasons that make CA3 the key player in both indexing and two-stage models of memory formation. Second, as the two-stage model emphasizes, the hippocampus output generally targets the neocortical regions from which it receives inputs (Buzsáki, 1989). This is the reason the hippocampus could be conceived as an association-feedback system that could bind neocortical representations and feed them back to the neocortex. Moreover, the fact that hippocampus input and output are generally the same, the hippocampus could also be conceived as an auto-encoder compressing the incoming information for storage (during learning) and decompressing it for broadcasting back to the neocortex during offline periods (McClelland et al., 1995).

1.2. Evidence for the involvement of sleep SWRs in memory processing

1.2.1. Reactivation of experience-dependent neuronal activity patterns during sleep SWRs

The first evidence supporting the role of SWRs in memory came from a pioneering study (Wilson & McNaughton, 1994) in which the activity of an ensemble of pyramidal CA1 neurons was monitored during three successive epochs, pre-behaviour sleep, behaviour (running on a familiar open field or linear track), and post-behaviour sleep. The authors found that the firing patterns of neurons with overlapping place fields during behaviour showed a high correlation, and importantly, the same neuron pairs showed higher correlation during the post-behaviour compared with pre-behaviour sleep epochs, specifically during SWRs.

The correlation structure of the firing activity of an ensemble of neurons does not necessarily inform about the spatiotemporal activity patterns of the ensemble. To test if the detailed spatiotemporal patterns of ensemble activity also reactivate during post-behaviour sleep, Lee and Wilson (Lee and Wilson, 2002) generated a template of activity pattern by averaging multiple rounds of stereotyped behaviour and then looking for its reactivation during post-behaviour sleep. They found that the template replayed more frequently than what was expected from the chance level, and the reactivations tended to coincide with SWRs.

The relevance of reactivation of experience-dependent patterns of neuronal activity during sleep SWRs on subsequent memory performance was supported by showing a positive correlation between the number of times a particular reward location was visited in a probe trial, conducted 2 hours after the learning session, and the number of times the spatial representation of that location was reactivated during SWRs in sleep period occurred between the learning and probe trial sessions (Dupret et al., 2010). In the same study, a positive relationship between the number of reactivations of rewarded locations during exploratory SWRs, which occurred during short pauses

on the maze while learning was ongoing, was also observed. Interestingly, the administration of an NMDA receptor antagonist during learning demolished the positive relationship for both sleep and exploratory SWRs.

1.2.2. SWR incidence rate increases during post-learning sleep

One of the predictions of the two-stage model posits that behavior and SWRs are related, and modification of either impacts the other (Buzsáki, 2015). Compatible with this prediction, studies have shown that the probability of SWR occurrence increases after learning and is more sustained after encoding a novel than a familiar experience (Eschenko et al., 2008; Ramadan et al., 2009). Moreover, the increase in SWR incidence was correlated with future memory performance (Ramadan et al., 2009). An intervention study found that post-leaning interruption of SWRs by electrical stimulation of the ventral hippocampus commissure increases the probability of initiation of SWRs in the hippocampus, suggesting a homeostasis-like process regulates the occurrence of SWRs. Importantly, this effect was not observed after foraging for food in a familiar environment where no learning was required (Girardeau et al., 2014), and when an NDMA receptor antagonist was administered prior, but not after, learning sessions. It suggests that learning-induced NMDA receptor-mediated synaptic plasticity affects the post-learning SWR activity.

1.2.3. Interrupting SWRs during post-learning sleep impairs memory performance

The evidence for the necessity of SWRs in memory consolidation comes from the intervention studies in which SWRs were aborted upon their initiation. The first of such studies was conducted by Girardeau et al. in rats (Girardeau et al., 2009). They trained rats daily in a radial

arm maze for spatial reference memory. SWRs were detected and electrically aborted for an hour during post-task sleep after each daily training session. Two control groups, one without stimulation and the other with delayed-ripple-triggered electrical stimulation were used; the former to establish the normal performance and the latter to control for any effect that the mere electrical stimulation would have on the memory performance. The experimental group consistently showed a lower level of memory performance compared with the control groups each day. Even though the experimental group eventually showed an above-chance performance, it took longer to reach this level compared with the control groups. Moreover, the unstimulated and delayed-stimulation groups did not show any difference in their daily performance.

In another study, rats were trained daily for spatial memory on two identical modified four-arm radial mazes (Ego-Stengel and Wilson, 2010). The daily training on each maze was temporally separated and was followed by a post-task sleep. On each day, SWRs were detected and electrically disrupted during post-task sleep only for one of the mazes. Interestingly, the rats showed slower learning only for the maze after which SWRs were truncated.

Van de ven et al. (van de Ven et al., 2016) tested the necessity of rest/sleep SWRs for consolidation of recently formed neuronal assemblies after exploration of novel and familiar open fields in mice. They used a rest/sleep – exposure - rest/sleep - re-exposure paradigm. An independent component analysis-based method was used to detect cell assemblies co-activating repeatedly throughout the exploration. They found that the reactivation of the detected assemblies was strongest during rest/sleep SWRs, and the reactivation of the majority of the assemblies was stronger during post- versus pre-exploration. They also found that the same assemblies reinstate when the mice were re-exposed to the same environment (reactivation of the index code in the hippocampus), and the rest/sleep reactivation and re-exposure reinstatement were positively

correlated. To test whether SWR activity was related to the reinstatements, CA1 neurons were optogenetically silenced, triggered by the incidence of SWRs, during rest/sleep after exposure. They found that the assembly reinstatements encoding the novel, but not the familiar environment, were impaired during re-exposure as a result of SWR disruption. Moreover, randomly silencing CA1 neurons independently of SWRs did not affect the reinstatement of the assemblies.

In another recent study, post-experience SWR activity was shown to be necessary for the synaptic down-regulation of CA1 neurons (Norimoto et al., 2018). Mice explored a novel environment for 30 minutes and then were returned to their homecages where SWRs were detected and aborted by optogenetically activating somatostatin-positive interneurons in CA3. Similar to previous studies, the rate of SWR incidence increased as a result of exploration (Eschenko et al., 2008; Ramadan et al., 2009) as well as SWR interruption (Girardeau et al., 2014). To measure the synaptic strength during the SWR interruption period, excitatory post-synaptic potentials (fEPSCs), induced by electrically stimulating Schaffer collaterals, were recorded from the CA1 stratum radiatum. The slope of the fEPSPs was used as a measure of synaptic strength. The authors observed that the fEPSPs slope gradually declined in two control groups, one of which did not receive light stimulation, and the other received light stimulation with a delay after detection of SWRs. However, the SWR-interrupted group did not show a gradual decrease suggesting that SWR activity plays a crucial role in down-regulating synapses in CA1. The follow-up in vitro experiment revealed that the SWR-mediated synaptic down-regulation was NMDA receptor-dependent. Interestingly, the retrieval of the object-place memory, encoded shortly after SWR interruption period and tested 2 hours after encoding, was impaired. This observation is consistent with the idea that over-potentiated/saturated synaptic matrix might impair new learning (Yoo et

al., 2007; Bulduzzi & Tononi 2013), and SWR activity aids the restoration of synaptic weights to prepare the brain for new learning.

All previous intervention works disrupted SWR activity in a content-unspecific way and therefore, cannot demonstrate the necessity of offline replay of a specific memory for its consolidation. A recent study (Gridchyn et al., 2020) addressed this caveat by utilizing an online clusterless decoding method allowing the detection of reactivation of a specific memory and disrupting neuronal activity associated with it. Rats were trained for different goal locations in two separate cheeseboard mazes. During post-learning sleep/rest, lasting ~4 hours, the neuronal spiking patterns initiated by "high synchrony events (HSE)" (and not necessarily SWRs) were decoded and disrupted only if they reactivated a specific maze. Subsequently, the goal location memory was tested in a probe trial, and interestingly, only the memory, associated with the specific maze, was impaired. Although the reactivation patterns were manipulated during HSEs, around %70 of the HSEs were followed by an SWR within ~100 ms. Thus, it is fair to assume that the reactivation interruption was locked to SWR activity.

1.3. Evidence for the involvement of awake SWRs in memory processing

Awake, compared with sleep, SWRs occur in dramatically different brain and behavioral states. During sleep, the brain is disengaged from the external world and sensory processing. However, during active wakefulness, animals show a vast repertoire of behaviors such as deliberation, decision-making, and planning. Moreover, the activity level of subcortical neuromodulatory systems, signaling the valence of experiences as well as internal states of the animal, are quite different between sleep and wakefulness. The abovementioned factors along with several interesting observations (some of which will be reviewed shortly) have led to the proposal

of multiple, yet related, hypothetical roles for awake SWRs including credit assignment (Davidson et al., 2009a), planning (Diba and Buzsáki, 2007; Dupret et al., 2010; Pfeiffer and Foster, 2013; Wu et al., 2017; Xu et al., 2019), retrieval (Roumis and Frank, 2015), memory maintenance/consolidation (Gillespie et al., 2021), stabilization of hippocampal spatial representations (Roux et al., 2017), and a mixture of retrieval/planning/consolidation (HF et al., 2017; Joo and Frank, 2018).

1.3.1. Replay of experience-dependent neuronal activity patterns during awake SWRs

The first peculiar observation about awake SWRs was made by Foster et al. (Foster and Wilson, 2006). The researchers noticed when rats stopped to consume a food reward at one end of a linear track, the firing of hippocampal place cells replayed in the reverse order starting from where the animal was located and moving backward to the other end of the track. The authors suggested that reverse replays during awake SWRs, paired with slowly decaying reward-induced dopaminergic activity, might be involved in backward propagation of value along the traversed trajectory. Later, this finding was replicated and extended by Diba et al. (Diba and Buzsáki, 2007). They found that replay during awake SWRs occurs in both forward and backward (reverse) order, and the probability of the forward is twice that of the backward replays on a linear track. Importantly, the majority of the forward and backward replays occurred right before the rats started running toward the other end and right after they had arrived at one end of the track, respectively. The representation of upcoming trajectory during the forward replays led the authors to suggest that awake forward replay might assist planning.

The planning hypothesis was further supported by studying awake replays in a two-dimensional open field where the rats had the flexibility to choose between multiple routes and

presumably plan accordingly (Pfeiffer and Foster, 2013). The investigators found a stronger correspondence between the replayed trajectories and the routes taken by animals immediately after than before the replay event. Predictability of immediate future path from replayed content during awake SWRs was further supported by a recent study conducted by Xu et al. (Xu et al., 2019). Three variants of the 8-arms radial arm maze with different loads of spatial reference and working memory were used in this study. The authors reported that the replay content, occurring at the central area (choice point) of the maze during awake SWRs while rats were learning which arms were baited, favored the immediate next and immediate past traversed arms, respectively, on the spatial reference and working memory versions of the task. Moreover, in all three variants of the task, the preferred replay effect was not observed on the error trials where rats chose a wrong arm to visit. This was considered a support for the involvement of awake SWRs in planning future paths.

On the other hand, a recent study (Gillespie et al., 2021) made a strong case in favor of the maintenance/consolidation versus planning role of the awake replay. The authors argued that if awake replay is involved in planning, it should affect or be correlated with the subsequent behaviour. Indeed, some of the studies, reviewed above (Pfeiffer and Foster, 2013; Xu et al., 2019), reported such a correlation. However, Gillespie et al. argued that the task structure of previous studies had not allowed for disambiguating between the role of the awake relay in future and past behaviour, and therefore, had limited the interpretations of the results. The problem with the tasks used in previous studies, the authors believe, has been the fact that the tasks have required a repetitive navigation toward a limited number of unchanging reward locations. In addition, there have not been any spatially and temporally remote option available to the animals in those tasks. To address these caveats, they designed a dynamic memory task called eight-arm spatial version

of win-stay, lose-switch task. In each block of the task, the rats were supposed to search the arms to identify the only baited arm, and then repeatedly visit that arm to collect the reward. After the baited arm was visited for a certain number of times, another arm was randomly chosen to be baited, and the rats were supposed to start a new block and repeat the same procedure as before. In each day, each rat underwent multiple successive blocks, and this provided different reward and recency history for each arm. This dynamic task allowed the authors to study the relationship between the replay content with past and future choices as well as potential modulation of this relationship with reward and recency history of the past choices. Importantly, they found that the replayed location did not influence the tendency of rats to visit that location no matter what the reward and visit history of the location were. Additionally, they reported that the replay content was dominated with representations of the past visits to the rewarded arms (even after they were not rewarded anymore) as well as representations of the arms that have not been visited recently. Based on their findings, the authors suggested that awake replay better serves the memory maintenance, storage, and integration than guiding upcoming behaviour.

1.3.2. Interrupting SWP-Rs during learning impairs memory performance

The necessity of awake SWRs, occurring during the task performance, for memory was tested in a study (Jadhav et al., 2012) with the same experimental and control groups as used in the Girardeau et al. study (Girardeau et al., 2009). Awake SWRs were disrupted while rats were performing a spatial alternation task in a W-track each day. The task had two components, outbound and inbound motions. For the inbound component, rats were supposed to return to the central arm starting from either of the two outer arms. For the outbound component, rats started from the central arm and were supposed to move toward the arm opposite to the most recently

visited outer arm. Interestingly, SWRs interruption impaired only the memory for the outbound component of the task (working memory component), and the impairment was not observed in the control groups. Similar to Girardeau et al. study (Girardeau et al., 2009), SWR-disrupted rats eventually achieved above-chance performance in the outbound component of the task; however, it took them longer than it did for control groups.

Another study examined the necessity of intact awake SWR activity for the stability of hippocampal spatial representations and therefore cognitive map. Roux et al. (Roux et al., 2017) trained mice daily on a cheeseboard maze with 177 wells while only 3 of them were rewarded. Each training day session consisted of ~50 trials during which mice learned the location of three baited wells. During the learning trials, a subset of CA1 neurons was optogenetically and focally silenced upon the detection of SWRs that occurred around three rewarded locations. The training epoch was situated between two sleep and two exploration epochs (exploration-sleep-training-sleep-exploration). The two exploration epochs were conducted on the same cheeseboard maze but without any rewarded well. The purpose of using exploration epochs was to characterize the spatial map of CA1 neurons and to test the spatial memory of mice for previously-rewarded wells. Mice showed a tendency to visit the previously-baited wells during the post-training than pre-training exploration epochs indicating that the memory retrieval was not impaired, at least severely, by the intervention. However, the spatial representation of the silenced, but not unaffected recorded place cells, was different in pre- versus post-training exploration epochs. Importantly, the observed effect vanished if the rewarded wells were marked by visual cues. Given that the described intervention destabilizes the hippocampal spatial maps in the memory-, but not cue-guided-version, of the task, the authors suggested that awake SWR activity is needed for stabilization of the hippocampal map when new spatial configurations are being learned.

Manipulating some features, such as duration, amplitude, and frequency of SWRs could provide insight into their role in memory processing. To test this idea, Fernandez-Ruiz et al. (Fernández-Ruiz et al., 2019) detected and optogenetically prolonged the spontaneously occurring SWRs while the rats were performing a spatial alternation task on a W-maze. The task and maze were the same as those in Jadhav et al. (reviewed above). They used two control groups, one without any stimulation and one with delayed stimulation. The delayed (400-1000 ms) stimulation of CA1 pyramidal neurons induced a ripple-like event in the LFP signal which, in almost all the cases, were separated from the previous spontaneous SWR. Thus, this procedure reliably induced ripples in the population of stimulated CA1 neurons, although the sharp-wave component of them appeared to be disrupted. Then, the effect of these manipulations on the memory performance of the animals was tested. The ripple prolongation, but not delayed induction of ripples, improved the performance in the outbound segment of the task (working memory component). The number of days to reach the threshold performance criterion was also smaller for the SWR-prolonged group compared with the other two control groups. Moreover, the prolonged, compared to spontaneous or induced, ripples contained more spatial information and recruited a more diverse set of place cells.

1.4. Evidence for the involvement of HPC-NCTX interactions in memory processing

1.4.1. Coordinated HPC-NCTX reactivation during sleep

Coordinated activity between the neocortex and hippocampus during slow-wave sleep, in the form of coupling between delta waves, spindles, and SWRs, has been abundantly reported (Isomura et al., 2006; Mölle et al., 2006; Siapas and Wilson, 1998; Sirota et al., 2003). In addition, it has been shown that the strength of the coordination between the two structures increases as a

function of learning (Khodagholy et al., 2017), and artificially locking SWRs and neocortical delta waves compensates for the lack of sufficient training resulting in memory performance improvement (Maingret et al., 2016). Despite the reports on the existence and functional relevance of coordinated activity between the two structures, neocortical (Euston et al., 2007; Hoffman and McNaughton, 2002; Johnson et al., 2010; Tatsuno et al., 2020) and hippocampal (see the literature reviewed above) reactivation/replay during post-task sleep have been studied mainly independent of each other. As a result, reports on the coordinated HPC-NCTX reactivation and evolution of such reactivation as a function of learning are rare. Here, I review some of these reports.

Short after observation of reactivation of neuronal pair correlation structure in the hippocampus (Wilson and McNaughton, 1994), the findings were extended to the hippocampal-neocortical network (Yu-Lin Qin et al., 1997) by showing that, during post-maze slow-wave sleep, the correlation between the firing of pairs of neurons between the hippocampus and posterior parietal cortex as well as within each region were more linearly related to those during maze exploration than to those during pre-maze slow-wave sleep. It was the first evidence that neuronal patterns associated with behavior coherently reactivate in the hippocampal-neocortical circuits later during sleep. However, no relationship between the reactivations and SWRs was reported.

Later, the observation of coherent reactivation of co-firing between HPC and NCTX was extended to the observation of coherent replay of sequential activation of neurons (Ji and Wilson, 2007). The authors reported a higher probability of repetition of behaviour-induced sequential activity of the visual cortex as well as hippocampus neurons during post-running than during pre-running slow-wave sleep. In addition, they reported a very low, but significant, number of coherent replays of sequential activity, representing the same trajectories, between the two structures. Again, no relationship between such coherent replays and SWRs was reported.

The evidence for the coordination of SWRs and neocortical reactivation of behaviour-evoked ensemble of neurons was first reported by Peyrache et al. (Peyrache et al., 2009). The authors introduced a new method of detecting ensemble-level reactivation of behaviour-evoked patterns of neuronal activity. Using this method and a rule-switching spatial task, they found that medial prefrontal cortex (mPFC) neuronal activity associated with task performance reactivated more strongly during post- than pre-task sleep. Moreover, almost all the reactivations occurred in the vicinity of SWRs. The authors reported that, on average, the peak mPFC reactivations occurred ~40 ms after the SWR peaks. However, the neocortical reactivation strength began to elevate ~ 200 ms before the SWR peaks. This observation provided strong evidence for coordinated, and possibly bidirectional, HPC-NCTX interactions in close vicinity of SWRs. Interestingly, it was found that mPFC neuronal activity around SWRs mainly reactivated the patterns of activity associated with the times at which the rats were located at the choice point and were supposed to choose the upcoming trajectory. Additionally, the choice-point reactivations emerged after the rats learned the new rule on the task which implies the learning-dependence of the reactivations. A follow-up study (Benchenane et al., 2010) showed that the mPFC neuronal ensembles, active during high synchronous theta activity between HPC and mPFC, reactivated more strongly during post- than pre-task sleep, and there was a close temporal relationship between the reactivations in mPFC and SWRs in HPC.

The auditory cortex was the next neocortical region to be reported to show coordinated reactivations with HPC SWRs (Rothschild et al., 2016). The PCA-based method of reactivation detection, introduced by Peyrache et al., revealed that reactivation strength of auditory cortex (AC) neuronal ensembles increases in the close vicinity of HPC SWRs in post-task sleep. Moreover, the pre-SWR AC neuronal activity was predicative of the firing of CA1 neurons during SWRs, and

firing patterns of CA1 neuronal ensembles during SWRs was in turn predictive of upcoming AC neurons' firing. This pattern of successive predictions was suggestive of a neocortical-hippocampal-neocortical loop of information flow in the close vicinity of SWRs.

1.4.2. Coordinated HPC-NCTX reactivation during wakefulness

Investigations of coordinated hippocampal-neocortical reactivation in the awake state are infrequent and have mainly been focused on the interactions of the hippocampus and medial prefrontal cortex (mPFC).

In contrast to the previous research on sleep SWRs reporting peri-SWR elevated firing rate for a significant proportion of mPFC neurons as the dominant mode of activity modulation, Jadhav et al (Jadhav et al., 2016) reported that both elevated and suppressed patterns of firing rate modulation of mPFC neurons equally existed during SWRs occurred in learning sessions. Despite some differences in the encoding properties, the authors asked whether these two subpopulations show a coordinated reactivation with CA1 neurons. To test this idea, the similarity between spatial maps of CA1-mPFC cell pairs was correlated with their co-firing during awake SWRs. The results revealed that both subpopulations showed a significant coordinated cell-pair-reactivation with CA1 neurons.

The observation of both elevated and suppressed patterns of peri-awake-SWR activity in mPFC neurons suggested potential differences in HPC-NCTX interactions around awake and sleep SWRs. Such differences were then investigated in a follow-up study by Tang et al. (Tang et al., 2017). They replicated the result reported by Jadhav et al. and extended them by providing a comparison between awake and sleep SWRs. In this study, rats were trained in multiple daily

learning sessions, interleaved with sleep epochs, to perform a spatial alternation task in a W-maze. The neuronal activity of CA1 and mPFC was continuously recorded during all the learning and sleep sessions in each day which allowed the coordinated replay of activity associated with past experiences to be compared across awake and sleep SWRs. First, the authors compared the pattern of mPFC cells modulation around awake and sleep SWRs, and found an equal proportion of SWR-excited and SWR-inhibited mPFC neurons during awake state (similar to the findings in Jadhav et al.). However, the proportion of SWR-excited was significantly larger than that of SWR-inhibited mPFC neurons during sleep. Interestingly, they did not find a relationship between patterns of sleep and awake modulations of mPFC neurons. More importantly, they compared the coordinated reactivation between the hippocampus and mPFC during awake and sleep SWRs. To measure the reactivation events, multiple methods including 1) correlation between co-firing of cell pairs (CA1-CA1 and CA1-PFC pairs) during SWRs and similarity of their spatial representations (O'Neill et al., 2008), 2) PCA-based ensemble-reactivation method (Peyrache et al., 2009), and 3) explained variance (Kudrimoti et al., 1999) were used. By all three measures, awake-SWR-reactivations were stronger than sleep-SWR-reactivations. This observation led the authors to suggest that the more accurate representation of past experiences by HPC-mPFC reactivations during awake SWRs might be well-suited for memory-guided behaviour while the coordinated reactivations during sleep might be involved in the integration of multiple experiences.

An important advancement in understanding behavioral relevance of peri-awake-SWR HPC-mPFC interactions was made by a recent study conducted by Shin et al. (Shin et al., 2019). They used a mass training paradigm where multiple successive learning sessions, interleaved with rest periods, were conducted. Concurrently, the activity of the same CA1 and mPFC neuronal population was recorded as rats were improving in performing a spatial alternation task on a W-

maze. Both reverse and forward CA1 replay during awake SWRs, occurring mainly at the reward endpoints, were reported. Importantly, regardless of performance level and stage of learning, neither of the two replay types were predicative of the upcoming choice (turn left or right) when the rats were located at the central arm and were to choose one of the two side-arms which was opposite of the one they had visited most recently. It meant that both side-arms were equally reactivated at the choice point. However, when the coherent reactivations of CA1-mPFC populations were considered, the authors found that these reactivations were stronger when CA1 was replaying the path that was going to be actually taken or had just been taken by the animals. This led the authors to propose that, during awake SWRs, the hippocampus replays multiple paths that could be potentially taken by the animal, and downstream regions like mPFC then choose one of them to be taken.

Although replay of sequential mPFC neuronal activity has been reported during sleep (Euston et al., 2007), such observation during awake state has been missing. This gap was filled with a recent study in which rats were trained on a rule-switching spatial task while the simultaneous activity of single cells in mPFC and CA1 were being recorded (Kaefer et al., 2020). It was found that the sequential positions on the maze (i.e. trajectories) could be decoded from the activity of mPFC as well as from HPC neurons during immobility periods on the maze. Interestingly, the authors reported that only %5 of replay events in the two structures co-occurred. However, about half of the replay events in each structure occurred during awake SWRs. This observation led the authors to suggest that the coordinated mPFC-HPC replays might be involved in consolidation while independent replays might play a role in local processes in mPFC.

Investigating the selectivity of mPFC neurons to hippocampal replay content requires recording from a large ensemble of CA1 cells. This issue was addressed by Berners-Lee et al.

(Berners-Lee et al., 2021). They implanted rats with 40 independently movable tetrodes, a half into dorsal CA1 and a half into mPFC, and recorded a large number of CA1 cells allowing them to reliably decode the content of replay events. The recording was performed in the early learning stage of a spatial alternation task on a novel Y-maze. During awake SWRs, replay events in CA1 population activity, representing each of the three arms, were detected. Although mPFC neurons did not show a high spatial selectivity as CA1 place cells did, they were still selective to the replayed arm in a way that the replayed arm identity could be discriminated from the activity of mPFC neurons. Then the authors asked whether mPFC neuronal activity during replay of a particular arm by CA1 neurons resembled that during actual experience of the arm on the maze. In other words, did mPFC neurons reactivate the same experience replayed by the CA1 population? The answer interestingly was "No". Instead, it was found that mPFC neurons were more tuned to a component of CA1 activity which was not associated with the encoding of the currently-experienced location. They found that CA1 activity was split between the first and second half of each theta cycle, and the two halves were associated with local (classic place cells) and non-local spatial encoding, respectively. It was the second half to which mPFC neurons were tuned, and that explained why reactivation of CA1 and mPFC populations did not match. The authors took the mismatched reactivations as evidence against the hippocampal memory indexing theory.

1.5. My dissertation plan

The index theory posits that repeated reactivation of hippocampal-neocortical representations could lead to memory consolidation, and the two-stage model proposes that such reactivations, during offline periods including sleep and quiet wakefulness, mainly occur in the vicinity of SWRs. This hypothesis has been the center of theories of memory consolidation, and it

has been supported with a large body of research some of which were reviewed here. Although the experiences and their reactivations are believed to be represented in the spatiotemporal activity patterns of the entire neocortex, the previous studies on reactivations and coordinated hippocampal-neocortical interactions have been limited to recordings from one or a few discrete regions of the neocortex. Thus, I aimed to extend the previous findings by utilizing recording techniques allowing for monitoring activity of a large portion of the neocortex. Characterizing the dynamics of the hippocampal-neocortical interactions around SWRs over a large portion of the neocortex is an important step forward in the way of understanding system-level mechanisms involved in memory consolidation.

To obtain a large spatial coverage as well as a small (~20 ms) temporal resolution, wide-field optical imaging of glutamate- and voltage-sensitive fluorescent sensors in combination with hippocampal electrophysiological recording was used to investigate the dynamics of mesoscale peri-SWR neocortical activity and their relationship to hippocampal activity in both sleep and awake states. This investigation provided spatiotemporal maps of the neocortical activity around sleep and awake SWRs that could guide future studies on the role of hippocampal-neocortical interactions in memory processing across brain states. In chapters 2 and 3, respectively, the results of investigating the peri-SWR hippocampal-neocortical interactions during sleep and awake states are presented.

2. Spatiotemporal patterns of neocortical activity around hippocampal sharp-wave ripples during sleep[1]

2.1. Abstract

A prevalent model is that sharp-wave ripples (SWR) arise 'spontaneously' in CA3 and propagate recent memory traces outward to the neocortex to facilitate memory consolidation there. Using voltage and extracellular glutamate transient recording over widespread regions of mice dorsal neocortex in relation to CA1 multiunit activity (MUA) and SWR, we find that the largest SWR-related modulation occurs in retrosplenial cortex; however, contrary to the unidirectional hypothesis, neocortical activation exhibited a continuum of activation timings relative to SWRs, varying from leading to lagging. Thus, contrary to the model in which SWRs arise 'spontaneously' in the hippocampus, neocortical activation often precedes SWRs and may thus constitute a trigger event in which neocortical information seeds associative reactivation of hippocampal 'indices'. This timing continuum is consistent with a dynamics in which older, more consolidated memories may in fact initiate the hippocampal-neocortical dialog, whereas reactivation of newer memories may be initiated predominantly in the hippocampus.

2.2. Introduction

Beginning with the theoretical work of Marr(Marr, 1971), the idea that hippocampal-neocortical interactions during slow-wave sleep (SWS) play an important role in the process of systems memory consolidation has become a dominant paradigm in memory research(Buzsáki,

[1] This chapter has been publish in the journal of eLife (eLife 2020;9:e51972 DOI: 10.7554/eLife.51972) under the title "Spatiotemporal patterns of neocortical activity around hippocampal sharp-wave ripples".

1989; McClelland et al., 1995; Wilson and McNaughton, 1994). This idea is supported by observations of replay of recently active neural ensemble patterns in hippocampus(Kudrimoti et al., 1999; Nádasdy et al., 1999; Pavlides and Winson, 1989; Skaggs and McNaughton, 1996; Wilson and McNaughton, 1994) and neocortex(Euston et al., 2007; Hoffman and McNaughton, 2002; Ji and Wilson, 2007; Jiang et al., 2017; Y.-L. Qin et al., 1997), a key role of SWS in enabling structural rearrangements of neocortical synaptic connections(Yang et al., 2014), and effects of interruptions of SWS on memory (Gais et al., 2007). More specifically, replay of recent hippocampal patterns has been shown to be concentrated in SWR bursts (transient, 100-250 Hz, local field potential oscillations) and that SWRs significantly predict reactivation of neocortical ensembles during up-states (Peyrache et al., 2009). Finally, post-training, closed-loop interruption of SWR has a negative effect on memory for tasks that normally depend on the hippocampus for acquisition(Ego-Stengel and Wilson, 2010; Girardeau et al., 2009). Altogether, these works suggest that interactions between neocortex and hippocampus during SWS support memory processes.

A prevalent model is that SWRs arise ‘spontaneously’ in CA3, which could lead to memory retrieval due to attractor network dynamic, and propagate outward to the neocortex through CA1 to enable memory consolidation there(Buzsáki, 1989; Csicsvari et al., 2000; Shen and McNaughton, 1996). Moreover, the hippocampal memory indexing theory (HMIT) and the complementary learning systems theory (CLST) are two other prominent theories pointing to a functional relationship between neocortex and hippocampus for the retrieval of memories and their integration into neocortical connections. According to HMIT(McNaughton, 2010; Timothy J. Teyler and DiScenna, 1986), the hippocampus generates an "index code" which is stored within

weakly interacting neocortical processing modules at the time of the experience and serves to coordinate retrieval of complete memories either during behavior or sleep. According to the CLST, repetition of this reactivation process is believed to enable a consolidation process whereby the stored information is refined and eventually encoded by intra-neocortical connections in a form that is more categorically structured(McClelland et al., 1995; Winocur and Moscovitch, 2011) and relatively independent of the hippocampus. The increasing evidence favoring this memory-consolidation-by-replay theory suggests that a more detailed study of the spatiotemporal relationships between SWR and neocortical activation during sleep is of paramount importance.

Previous studies, using primarily electrophysiological methods, have focused on functional relationships between SWRs and a single or a few discrete neocortical regions(Alexander et al., 2018; Battaglia et al., 2004; Khodagholy et al., 2017; Mölle et al., 2006; Opalka et al., 2020; Siapas and Wilson, 1998; Sirota et al., 2003). These studies have shown that a given neocortical region can activate and deactivate around SWR times, which reflects the sleep-related neocortical slow oscillation (SO), and that SO can be spatially local or global propagating waves(Massimini et al., 2004; Mohajerani et al., 2010). Moreover, recently combined fast time-scale electrophysiological techniques with whole brain Blood Oxygen Level-Dependent (BOLD) fMRI imaging provided a snapshot of the cooperative patterns of the large numbers of brain structures involved either leading to or responding to hippocampal SWRs(Logothetis et al., 2012; Ramirez-Villegas et al., 2015). Although these studies have improved our understanding of hippocampal-neocortical interactions, their conclusions were limited because: (a) the electrophysiological approaches have been unable to resolve the regional structure and dynamics of HPC-NC interaction across a large neocortical area due to relatively sparse spatial sampling (b) fMRI studies generally rely on an

indirect measures of neuronal activity and the nature of the underlying neuronal activity correlate (i.e. synaptic and spiking activity) remain unclear. Given the physiological speed of neuronal communication, the cause-effect relationships are hard to decipher with certainty with the resolution at the scale of seconds of the fMRI method. In the present study we expand upon previous theoretical and experimental studies. We combined wide-field optical imaging of dorsal neocortex of mice, covering most of sensory and motor cortices and some association areas, with concurrent electrophysiological monitoring of hippocampal SWRs and MUA during natural sleep and under urethane anesthesia, which produces a state that is in many respects similar to natural sleep(Barthó et al., 2014; Clement et al., 2008; Pagliardini et al., 2013b).

We report both a spatial and temporal continuum in the degree and onset timing of modulation of neocortical activity around SWRs, thereby providing a spatiotemporal map of potential interactions between hippocampus and neocortex.

2.3. Results

2.3.1. Experimental protocol for investigating dynamics of hippocampal-neocortical interactions during sleep

Using in vivo wide-field of view mesoscale optical imaging and voltage-sensitive dye (VSD)(Bermudez-Contreras et al., 2018; Ferezou et al., 2007; Kyweriga et al., 2017; Mohajerani et al., 2013; Shoham et al., 1999) and genetically encoded sensor of extracellular glutamate (iGluSnFR)(Marvin et al., 2013a; Xie et al., 2016a)(**Figure 2.1 – S1**), we imaged neocortical activity dynamics from a large cranial window in the right hemisphere and combined it with electrophysiology in the ipsilateral hippocampus (**Figure 2.1A-C; Figure 2.1 – S1**) to capture

hippocampal SWRs and MUA. Unlike calcium reporters (e.g., GCaMP6) with slow kinetics, both VSD and iGluSnFR measures electrical activity with relatively high temporal resolution (Xie et al., 2016a). Due to the high level of synchrony in neocortical activity (Mohajerani et al., 2010) and

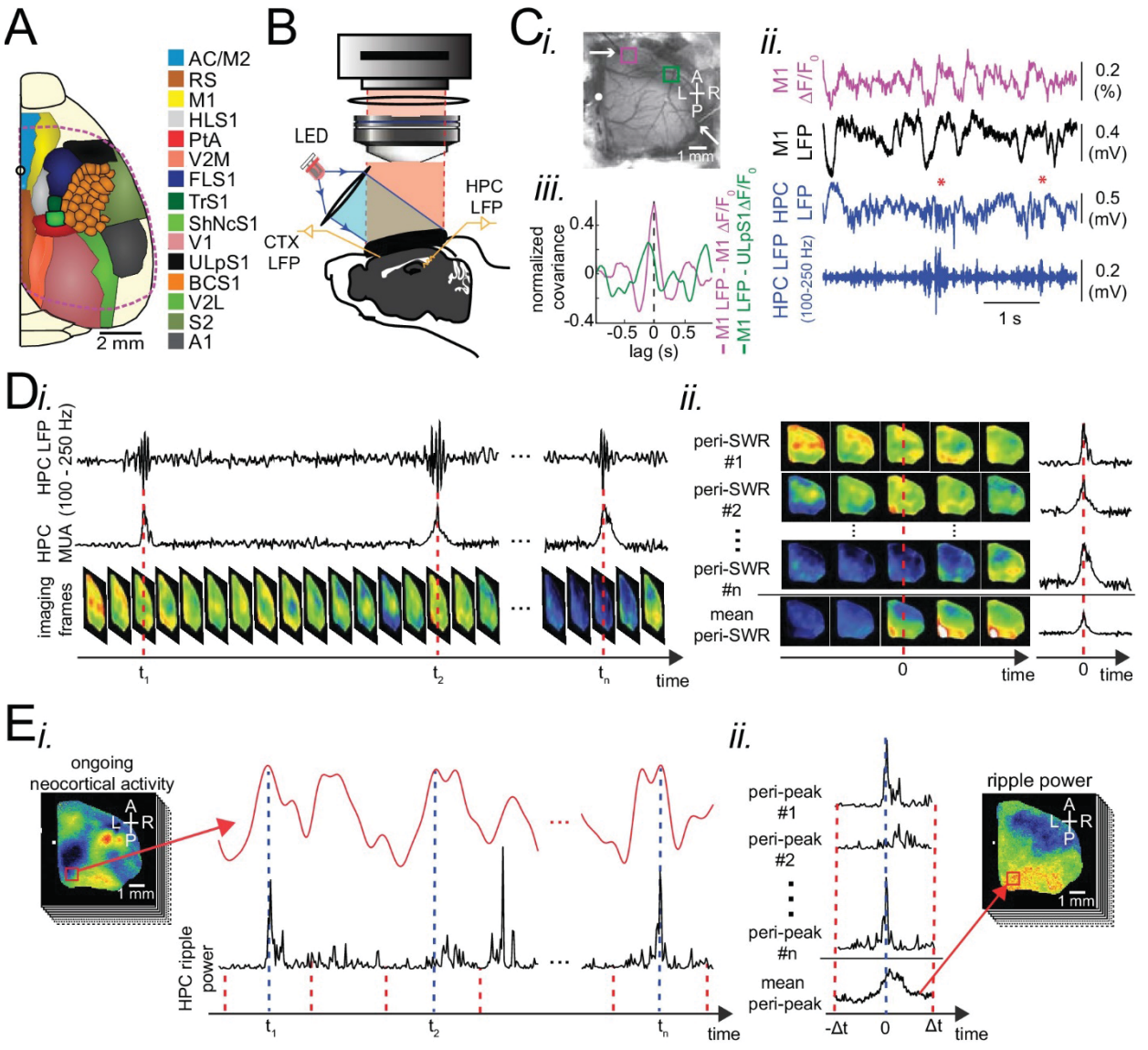

Figure 2.1. Experimental protocol for investigating dynamics of neocortical-hippocampal interactions during sleep**. (A)** Schematic of a cranial window for wide-field optical imaging of neocortical activity using voltage or glutamate probes. The voltage or glutamate signal was recorded from dorsal surface of the right neocortical hemisphere, containing the specified regions. The red dashed line marks the boundary of a typical cranial window. The abbreviations denote the following cortices AC/M2: anterior cingulate/secondary Motor, RS: retrosplenial, M1: primary motor, HLS1: hindlimb primary somatosensory, PtA: posterior parietal, V2M: secondary medial visual, FLS1: forelimb primary somatosensory, TrS1: trunk

primary somatosensory, ShNcS1: shoulder/neck primary somatosensory, V1: primary visual, ULpS1: lip primary somatosensory, BCS1: primary barrel, V2L: secondary lateral visual, S2: secondary somatosensory, A1: primary auditory. (**B)** Schematic of the experimental setup for simultaneous electrophysiology and wide-field optical imaging. A CCD camera detects reflected light coming from fluorescent indicators, in the superficial neocortical layers, which are excited by the red or blue LEDs. An additional infra-red camera recorded pupil diameter (not shown). Hippocampal LFP recordings were conducted for SWR and MUA detection. A neocortical LFP recording was also acquired to compare imaging and electrophysiological signals. **(C)** (i) Photomicrograph of the wide unilateral craniotomy with bregma indicated by a white circle in each image. Compass arrows indicate anterior (A), posterior (P), medial (M) and lateral (L) directions. The white arrow indicates a neocortical LFP electrode position. (ii) Exemplar voltage signal recorded from a region in the M1 indicated by a magenta square in Ci, aligned with neocortical and hippocampal LFPs, and a hippocampal trace filtered in the ripple band. Asterisks indicate detected SWRs. **(D)** Schematic figure demonstrating the peri-SWR averaging of neocortical activity. (i) Ripple band filtered LFP trace displaying three example SWRs (top row) and hippocampal multi-unit activity (MUA) trace (middle row), temporally aligned with concurrently recorded neocortical voltage activity (bottom row). (ii) For each detected SWR, corresponding neocortical imaging frames (left rows) and MUA traces (right rows) are aligned with respect to SWR centers and then averaged (bottom rows). **(E)** Demonstration of how peri-neocortical-peak-activation average ripple power was calculated. (i) The red trace is the voltage signal from the indicated region of interest (red square) shown in the image on the left. The black trace is the temporally aligned hippocampal ripple power time series. Blue dashed lines are the timestamps of three detected peak activations in the indicated neocortical region. (ii) For each detected peak activation, ripple power traces were aligned and averaged. This figure has two Ss.

i.

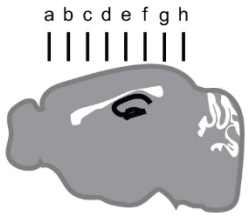

ii.

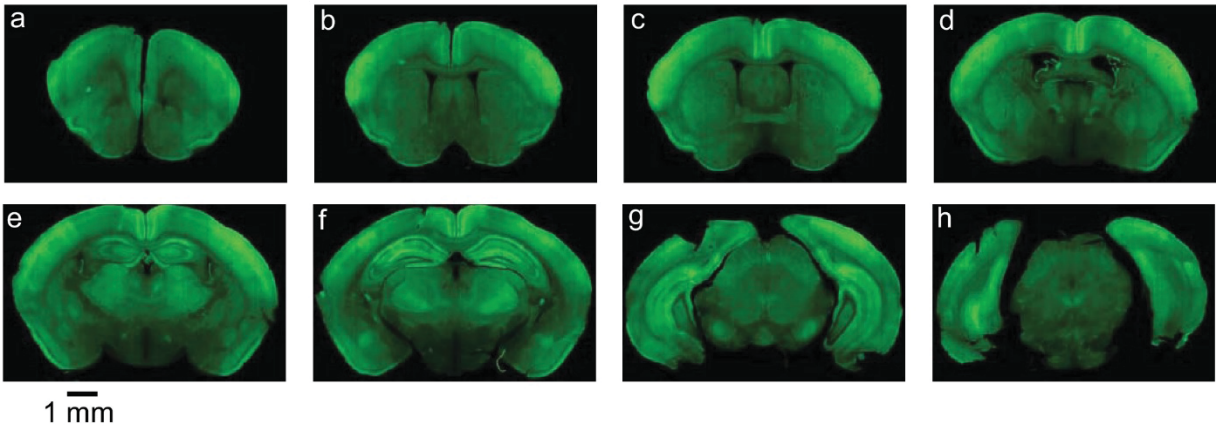

iii.

iv.

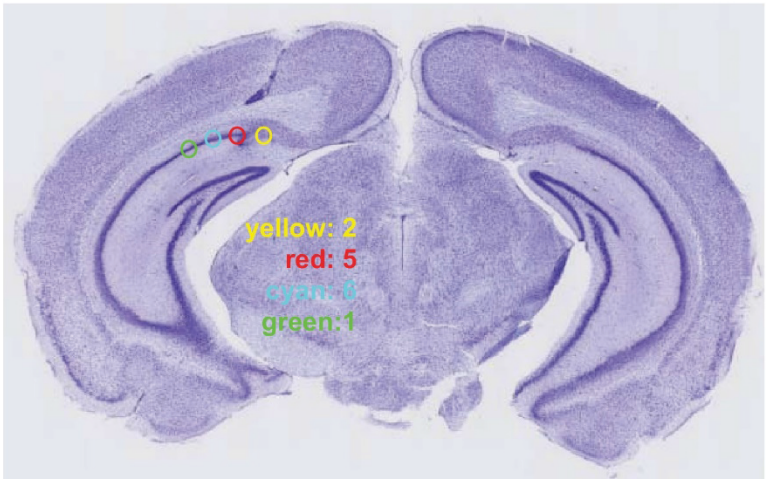

Figure 2.1 – S1. Expression level of iGluSnFR and electrode localization. (i) Schematic diagram representing the location of coronal sections presented here. (ii) Coronal sections showing the expression of iGluSnFR in the neocortex and hippocampus in EMX-CaMKII-Ai85 mouse. (iii) Coronal sections of the brain of a representative animal, stained with Nissl, showing the location of the tip of the hippocampal LFP electrode in the pyramidal layer of the CA1 subfield of the hippocampus. The sections are ordered from anterior to posterior from left to right. (iv) The distribution of HPC LFP electrode tips in 14 mouse brains is represented. The location of tips is categorized into 4 groups, each of which is colored differently. The number of animals in each colored category is reported on the figure.

hippocampal SWR activity(Chrobak and Buzsáki, 1996) across hemispheres, we decided to record unilaterally from neocortex and hippocampus. Imaging unilaterally has the advantage of larger coverage of neocortical regions, particularly more lateral ones like primary auditory cortex. In some of the conducted VSD imaging experiments, a bipolar electrode was utilized to record neocortical LFP. The wide-field optical imaging of membrane potential activity in a given region of interest was correlated with LFP activity recorded from the same neocortical site confirming that the optical voltage signal reflects underlying electrophysiological processes (Arieli et al., 1995) (**Figure 2.1C**). We conducted our experiments under both natural sleep and urethane anesthesia. Urethane anesthesia has been reported to model natural sleep; In particular, characteristic electrophysiological signatures of slow-wave sleep (SWS) including up- and down-states, delta waves, spindles, and hippocampal SWR are present under urethane anesthesia (Barthó et al., 2014; Clement et al., 2008; Pagliardini et al., 2013a; Wolansky et al., 2006) (**Figure 2.1Cii**). We confirmed that the quantities, reported in the following sections, were not different across urethane anesthesia versus sleep and VSD versus iGluSnFR imaging conditions (**Figure 2.2- S3; Figure 2.3- S1; Figure 2.4- S2; Figure 2.5- S2; Figure 2.6- S2; Figure 2.7- S2**). For natural sleep experiments, conducted on iGluSnFR mice under head-restrained condition, we used neck muscle electromyogram (EMG) recordings and hippocampal delta-to-theta band power ratio to score sleep state. Sleep scores were further validated by monitoring pupil diameter from each animal and

comparing the distribution of physiological measures in different sleep states (**Figure 2.1 – S2**). During the natural sleep experiments, pupil dilation measurement was possible since mice slept with eyelids partially open (Yüzgeç et al., 2018).

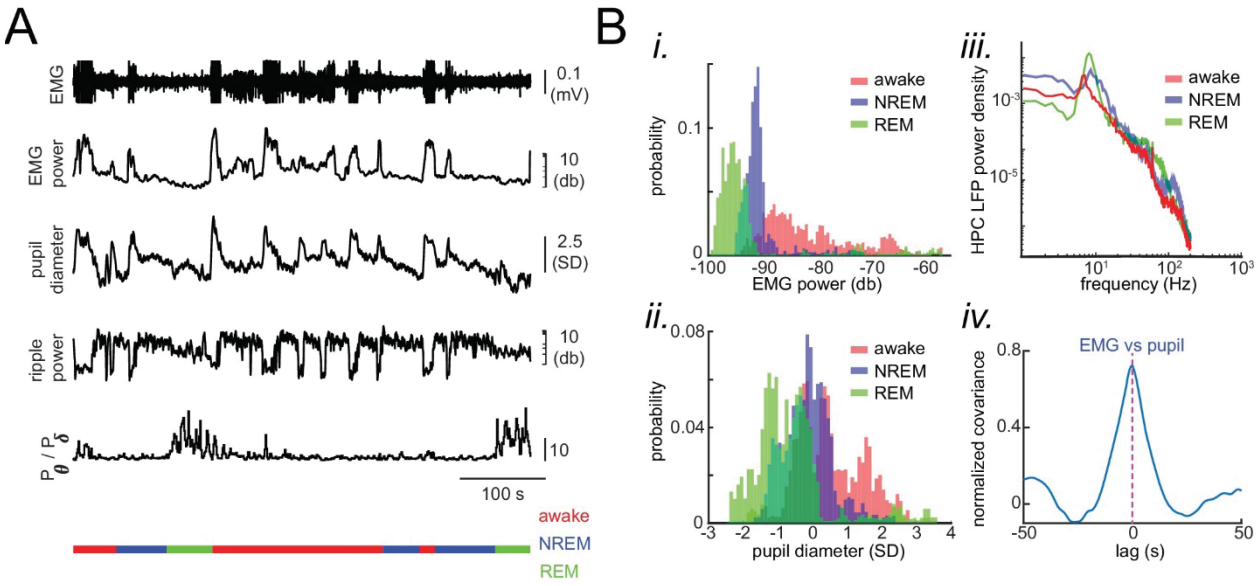

Figure 2.1 – S2. Physiological signatures of different brain states in the head-restrained mouse. (**A**) Representative traces of local field potentials (LFP) and electromyography (EMG) during waking, NREM and REM sleep. From top to bottom: raw EMG signal, EMG power measured at 30 - 1000 HZ, pupil diameter, hippocampal ripple power, theta-to-delta band power ratio trace calculated from hippocampal LFP signal, and hypnogram. In the hypnogram, REM, NREM, and awake represent states of animals i.e. REM sleep, NREM sleep, and wake periods, respectively, which were scored from EMG traces and hippocampal LFPs theta-to-delta band ratio. The EMG raw signal values are clipped for visualization purposes but the true values were used for scoring the sleep/wake period. (**B**) Histograms in (i) and (ii) show the distribution of EMG power and z-scored pupil diameter in a representative recording session across waking, NREM and REM sleep. Note the segregation of histograms across brain states. (iii) Exemplar hippocampal LFP power spectral density calculated for the same three states in a representative recording session. (iv) Representative normalized cross-covariance between EMG power and pupil diameter signals, showing a strong correlation at zero lag.

2.3.2. Patterns of activity in neocortical regions are differentially modulated around hippocampal SWRs

We began by investigating how different neocortical regions activate and deactivate around SWRs times. To do so, we performed SWR-triggered averaging of neocortical activity, (**Figure 2.1D; Figure 2.2A-B; Figure 2.2 – S1**). ~250 ms before the center of SWRs (t = 0; see *Methods*), most neocortical regions transiently deactivated. Deactivation was followed by a strong activation in most regions in close temporal proximity to SWRs (**Figure 2.2A-B**). Since these phenomena occurred in both head-restrained sleep and under urethane anesthesia, and the data exhibited a high degree of similarity (**Figure 2.2 – S2&3**), we pooled the urethane and head-restrained sleep data for group analysis. Out of all imaged regions, RSC was the most strongly modulated, showing the highest peak of activation (**Figure 2.2 – S3Ci**) and second highest peak of deactivation (**Figure 2.2 – S3Cii**). Interestingly, regions with comparable magnitudes of activations and deactivations tended to fall within previously identified neocortical structural subnetworks (Zingg et al., 2014) (**Figure 2.2Ci**). The medial subnetwork that includes RSC and posterior parietal cortex (PtA) along with the visual subnetwork showed the highest degrees of peri-SWR activation (**Figure 2.2Cii-iii;** n = 14 per subnetwrok; repeated measure ANOVA with Greenhouse-Geisser correction for sphericity: $F_{3,39} = 44.303$, $p = 2.2193\times10^{-10}$; post-hoc multiple comparison with Tuckey's correction: medial vs visual p = 0.11844, medial vs auditory $p = 7.8147\times10^{-5}$, medial vs somatomotor $p = 1.1128\times10^{-6}$, visual vs auditory p = 0.00024702, visual vs somatomotor $p = 2.9247\times10^{-05}$, auditory vs somatomotor p = 0.19802) and deactivation (**Figure 2D;** n = 14 per subnetwrok; repeated measure ANOVA with Greenhouse-Geisser correction for sphericity: $F_{3,39} = 15.508$, $p = 1.1009\times10^{-5}$; post-hoc multiple comparison with Tuckey's correction: medial vs visual p = 0.63021, medial vs auditory p = 0.014438, medial vs somatomotor p = 0.00076384,

visual vs auditory p = 0.0042707, visual vs somatomotor p = 0.0014657, auditory vs somatomotor p = 0.5317), respectively, followed by auditory and somatomotor networks.

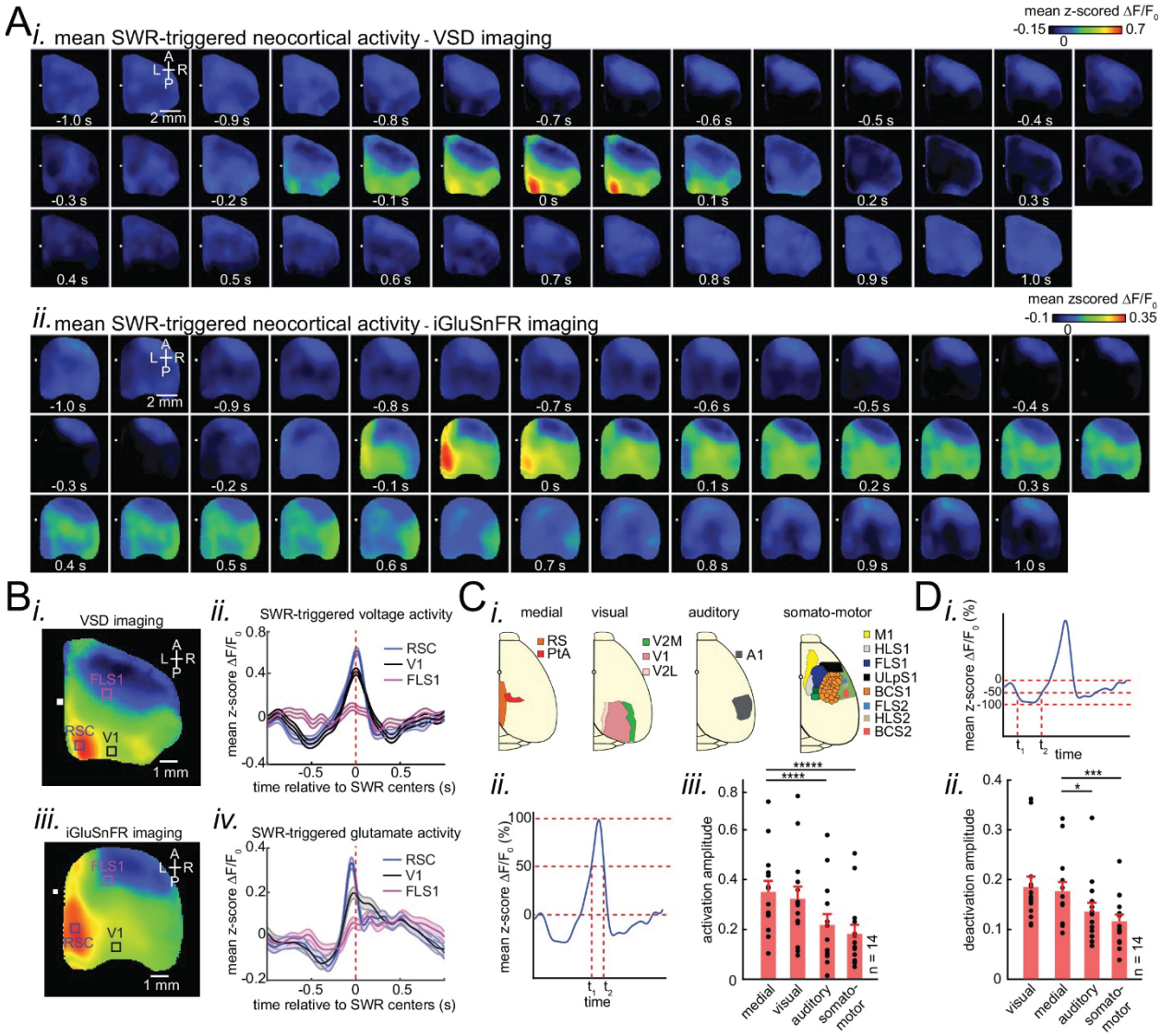

Figure 2.2. Patterns of activity in neocortical regions are differentially modulated around hippocampal SWRs**. (A)** Representative montage of mean peri-SWR neocortical activity measured using (i) voltage-sensitive dye and (ii) glutamate-sensing fluorescent reporter iGluSnFR under urethane anesthesia and head-restrained natural sleep, respectively. 0s-time indicates SWR centers. Images have been z-scored and scaled to the depicted color bars. **(B)** (i-iv) Example traces showing voltage or iGluSnFR signals from selected regions in (i) and (iii). Plots are the average of optical signals measured from 3 × 3 pixel boxes (~0.04 mm^2) placed within retrosplenial (blue), visual (black), and forelimb somatosensory (magenta) cortices. The thickness of the shading around each plot indicates SEM. 0 s-time indicates SWR centers. **(C)** (i) Four

major structurally defined neocortical subnetworks (medial, visual, auditory and somato-motor). (ii) Demonstration of how the activation amplitudes were quantified. The activation amplitude was defined as the mean of the signal across full-width at half maximum (t_1 to t_2). (iii) Grand average (n = 14 animals) of activation amplitudes across neocortical subnetworks, sorted in decreasing order. Each data point is the average of activation amplitudes of all regions in a given subnetwork and in a given animal. (repeated measure ANOVA with Greenhouse-Geisser correction for sphericity: $F_{3,39} = 44.303$, $p = 2.2193\times10^{-10}$; post-hoc multiple comparison with Tuckey's correction: medial vs visual p = 0.11844, medial vs auditory p = 7.8147×10^{-5}, medial vs somatomotor p = 1.1128×10^{-6}, visual vs auditory p = 0.00024702, visual vs somatomotor p = 2.9247×10^{-05}, auditory vs somatomotor p = 0.19802) **(D)** (i-ii) Same measurements as in C, but for neocortical deactivations preceding SWRs. Note that the deactivation peaks were rectified for group comparison in (ii). A higher value of deactivation amplitude indicates stronger deactivation. Bar graphs indicate mean ± SEM. (repeated measure ANOVA with Greenhouse-Geisser correction for sphericity: F3,39 = 15.508, p = 1.1009×10-5; post-hoc multiple comparison with Tuckey's correction: medial vs visual p = 0.63021, medial vs auditory p = 0.014438, medial vs somatomotor p = 0.00076384, visual vs auditory p = 0.0042707, visual vs somatomotor p = 0.0014657, auditory vs somatomotor p = 0.5317). This figure has five figure supplements.

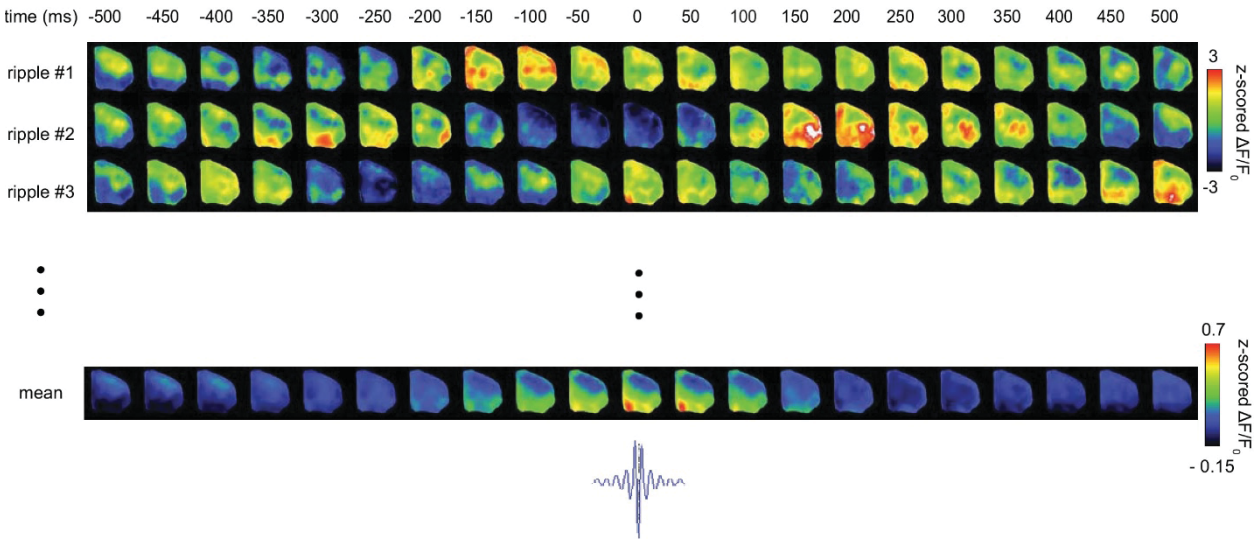

Figure 2.2 – S1. Representative spatiotemporal patters of neocortical activity around hippocampal SWRs. Neocortical activity centered (t = 0) on three randomly selected individual SWRs is represented.

Similar results were obtained using higher thresholds for detecting SWRs (**Figure 2 – S4**). In addition, we replicated some of these results using electrophysiology in unrestrained naturally sleeping mice in another cohort of animals (**Figure 2 – S5**).

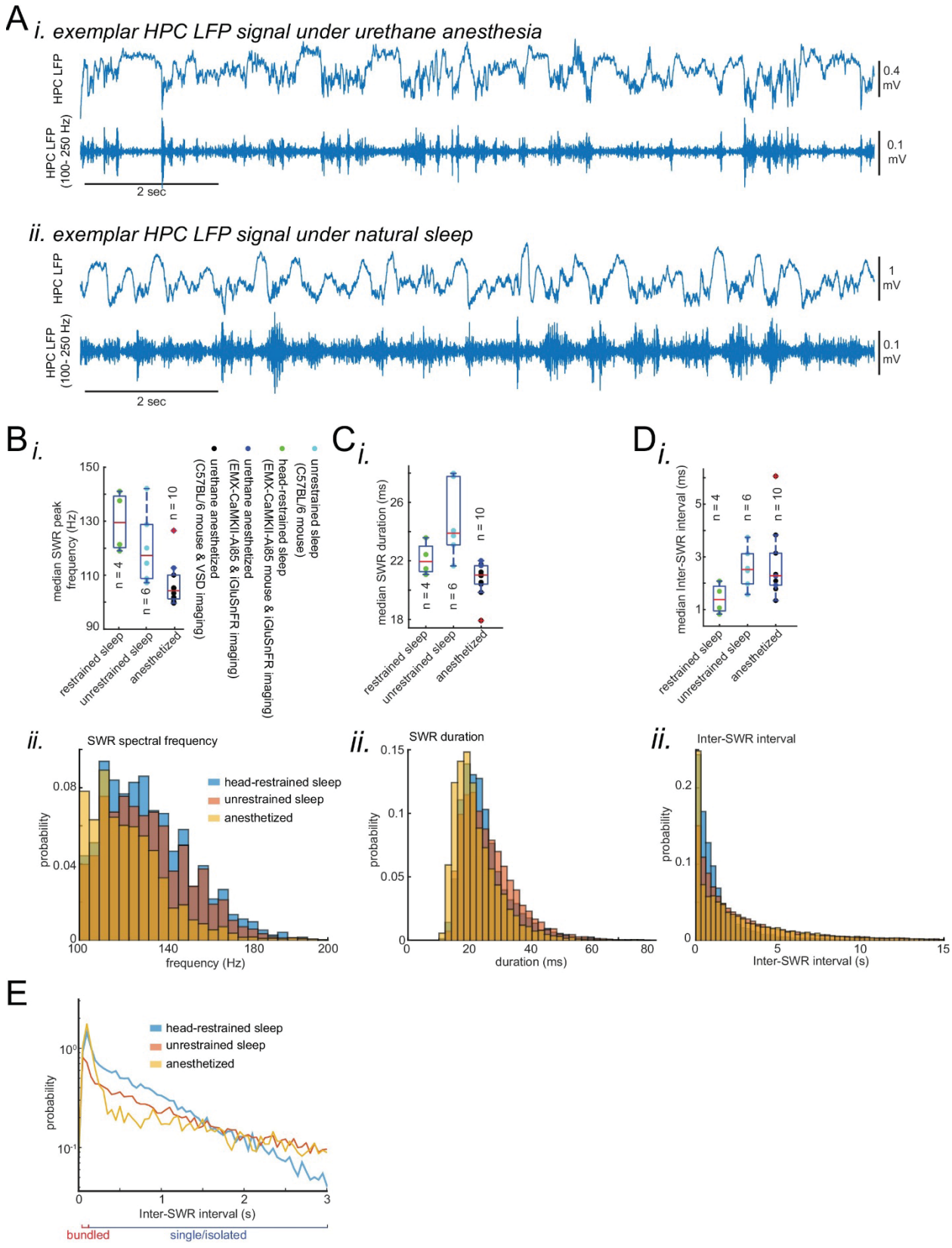
A
i. exemplar HPC LFP signal under urethane anesthesia
HPC LFP
HPC LFP (100- 250 Hz)
0.4 mV
0.1 mV
2 sec
ii. exemplar HPC LFP signal under natural sleep
HPC LFP
HPC LFP (100- 250 Hz)
1 mV
0.1 mV
2 sec
B i.
median SWR peak frequency (Hz)
n = 4
n = 6
n = 10
restrained sleep
unrestrained sleep
anesthetized
urethane anesthetized (C57BL/6 mouse & VSD imaging)
urethane anesthetized (EMX-CaMKII-Ai85 & iGluSnFR imaging)
head-restrained sleep (EMX-CaMKII-Ai85 mouse & iGluSnFR imaging)
unrestrained sleep (C57BL/6 mouse)
C i.
median SWR duration (ms)
D i.
median Inter-SWR interval (ms)
ii. SWR spectral frequency
head-restrained sleep
unrestrained sleep
anesthetized
probability
frequency (Hz)
ii. SWR duration
duration (ms)
ii. Inter-SWR interval
Inter-SWR interval (s)
E
head-restrained sleep
unrestrained sleep
anesthetized
probability
Inter-SWR interval (s)
bundled
single/isolated

Figure 2.2 – S2. Characteristics of SWRs recorded in urethane anesthesia, head-restrained and unrestrained naturally sleeping mice. (**A**) Exemplar HPC LFP signals recorded under urethane anesthesia (i) and natural sleep (ii). (**B**) (i) Median peak spectral frequency of hippocampal SWRs recorded under different experimental conditions: urethane anesthesia, head-restrained sleep, and unrestrained sleep. C57BL/6 mice were used in experiments in which the animals were either anesthetized with urethane for VSD imaging or unrestrained and naturally sleeping. EMX-CaMKII-Ai85 mice were imaged during head-restrained sleep or under urethane anesthesia. Each data point is the median value in a given animal. SWRs detected under urethane anesthesia tend to have slower peak frequencies. The red plus signs represent the data points outside the interval (centered on median value) which includes 99.3 percent of all data points. (ii) Similar to (i) but the histograms here is showing the distribution of peak spectral frequency of hippocampal SWRs pooled across all animals and across experimental conditions. (**C-D**) (i,ii) similar to A, duration (width) and inter-SWR time intervals of hippocampal SWRs are represented under different experimental conditions. Note that the SWRs detected under urethane anesthesia tend to have shorter durations. (**E**) The same as C (ii) but the histograms are plotted in the logarithmic scale.

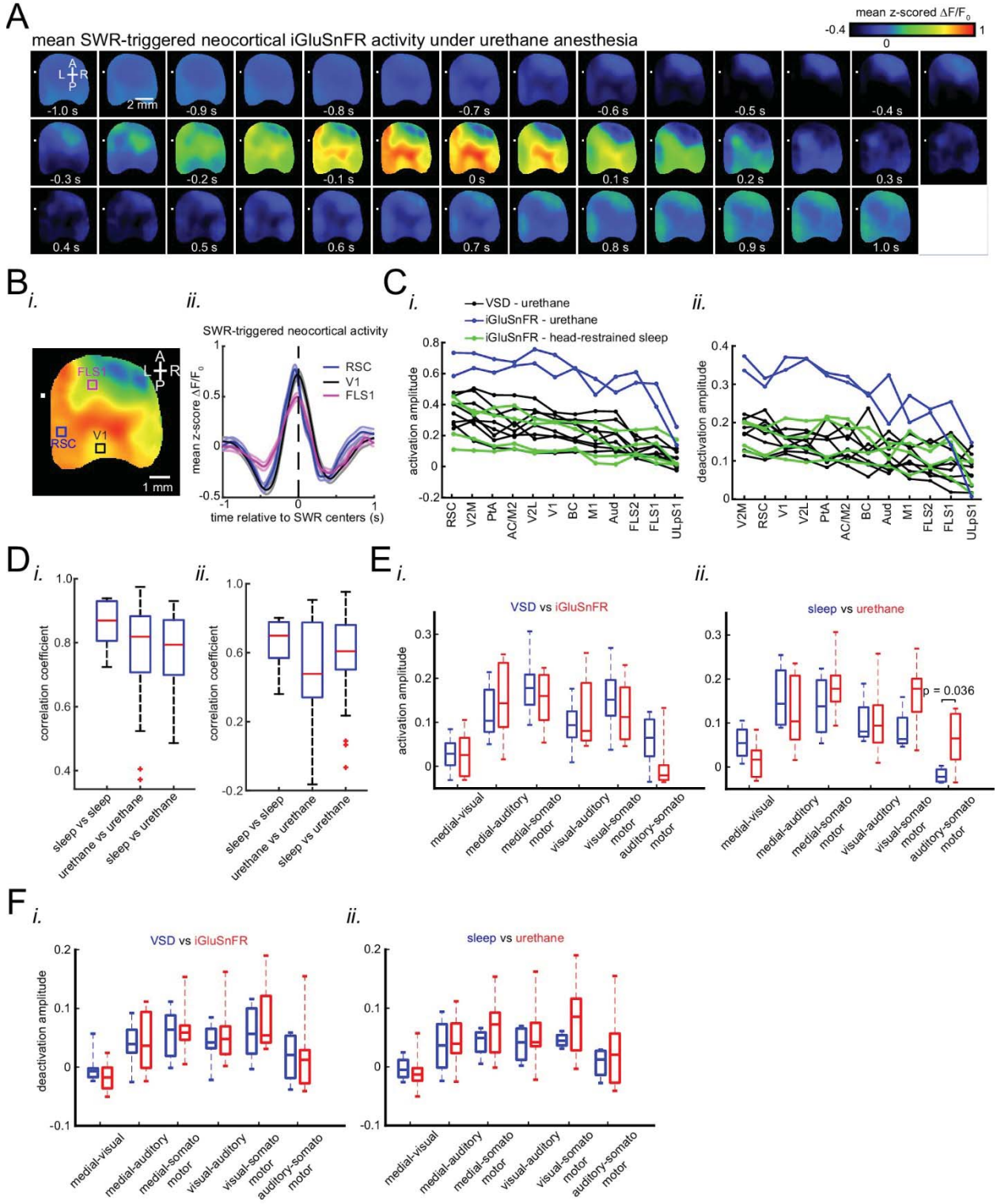
A
mean SWR-triggered neocortical iGluSnFR activity under urethane anesthesia
mean z-scored ΔF/F0
-0.4
0
1
-1.0 s
2 mm
-0.9 s
-0.8 s
-0.7 s
-0.6 s
-0.5 s
-0.4 s
-0.3 s
-0.2 s
-0.1 s
0 s
0.1 s
0.2 s
0.3 s
0.4 s
0.5 s
0.6 s
0.7 s
0.8 s
0.9 s
1.0 s
B i.
FLS1
RSC
V1
1 mm
ii.
SWR-triggered neocortical activity
RSC
V1
FLS1
mean z-score ΔF/F0
time relative to SWR centers (s)
C i.
VSD - urethane
iGluSnFR - urethane
iGluSnFR - head-restrained sleep
activation amplitude
RSC V2M PtA AC/M2 V2L V1 BC M1 Aud FLS2 FLS1 ULpS1
ii.
deactivation amplitude
V2M RSC V1 V2L PtA AC/M2 BC Aud M1 FLS2 FLS1 ULpS1
D i.
correlation coefficient
sleep vs sleep
urethane vs urethane
sleep vs urethane
ii.
correlation coefficient
sleep vs sleep
urethane vs urethane
sleep vs urethane
E i.
VSD vs iGluSnFR
activation amplitude
medial-visual
medial-auditory
medial-somato motor
visual-auditory
visual-somato motor
auditory-somato motor
ii.
sleep vs urethane
p = 0.036
medial-visual
medial-auditory
medial-somato motor
visual-auditory
visual-somato motor
auditory-somato motor
F i.
VSD vs iGluSnFR
deactivation amplitude
medial-visual
medial-auditory
medial-somato motor
visual-auditory
visual-somato motor
auditory-somato motor
ii.
sleep vs urethane
medial-visual
medial-auditory
medial-somato motor
visual-auditory
visual-somato motor
auditory-somato motor

Figure 2.2 – S3. Differential modulation of neocortical regions under sleep/urethane anesthesia and VSD/iGluSnFR imaging conditions are similar. (**A**) Representative mean peri-SWR neocortical activity (0-time indicates SWR centers) recorded in urethane-anesthetized EMX-CaMKII-Ai85 mice. This animal was also recorded under natural sleep (see Figure 2A ii). Mean peri-SWR neocortical activity patterns during head-restrained sleep are similar to spatiotemporal patterns of neocortical deactivation and activation around SWR times obtained under urethane-anesthesia. (**B**) Plots are the average of the iGluSnFr signals measured from 3 × 3 pixel boxes (~0.04 mm^2) placed within retrosplenial (blue trace), visual (black trace), and forelimb somatosensory (magenta trace) cortices. The thickness of the shading around each plot indicates SEM. Time-series representation of peri-SWR neocortical activity allows for better visualization of temporal differences in activation of different regions. (**C**) Peri-SWR activation (i) and deactivation (ii) amplitudes across distinct neocortical regions, sorted in decreasing order. Each piece-wise linear trace is associated with a particular animal (n = 14 mice). These data were used to generate bar graphs presented in Figure 2C iii and 2D ii by averaging the data points across regions in a given neocortical structural subnetwork. The color code represents different recording conditions. (**D**) Quantification of similarities between the trends of activation (i) and deactivation (ii) amplitudes across neocortical regions under urethane anesthesia and natural sleep. The box plot shows the distribution of correlation coefficients between all possible pairs of traces associated with natural sleep (green lines in C) and urethane anesthesia (blue and black lines in C). Horizontal red lines represent the median of each distribution. As measured by correlation coefficients, there is no significant difference between both activation and deactivation amplitude trends under urethane anesthesia and natural sleep. Therefore, we decided to pool the urethane and natural sleep data in this paper. The red plus signs represent the data points outside the interval (centered on median value) which includes 99.3 percent of all data points. **(E)** The difference of activation amplitudes (arithmetic subtraction) between all possible pairs of subnetworks is compared across VSD versus iGluSnFR (i) and sleep versus urethane conditions (ii). The only statistically significant result is from the difference auditory-somatosensory (auditory minus somatosensory) in sleep versus urethane comparison. **(F)** The same as E but for deactivation amplitude. There was no significant statistical difference across conditions.

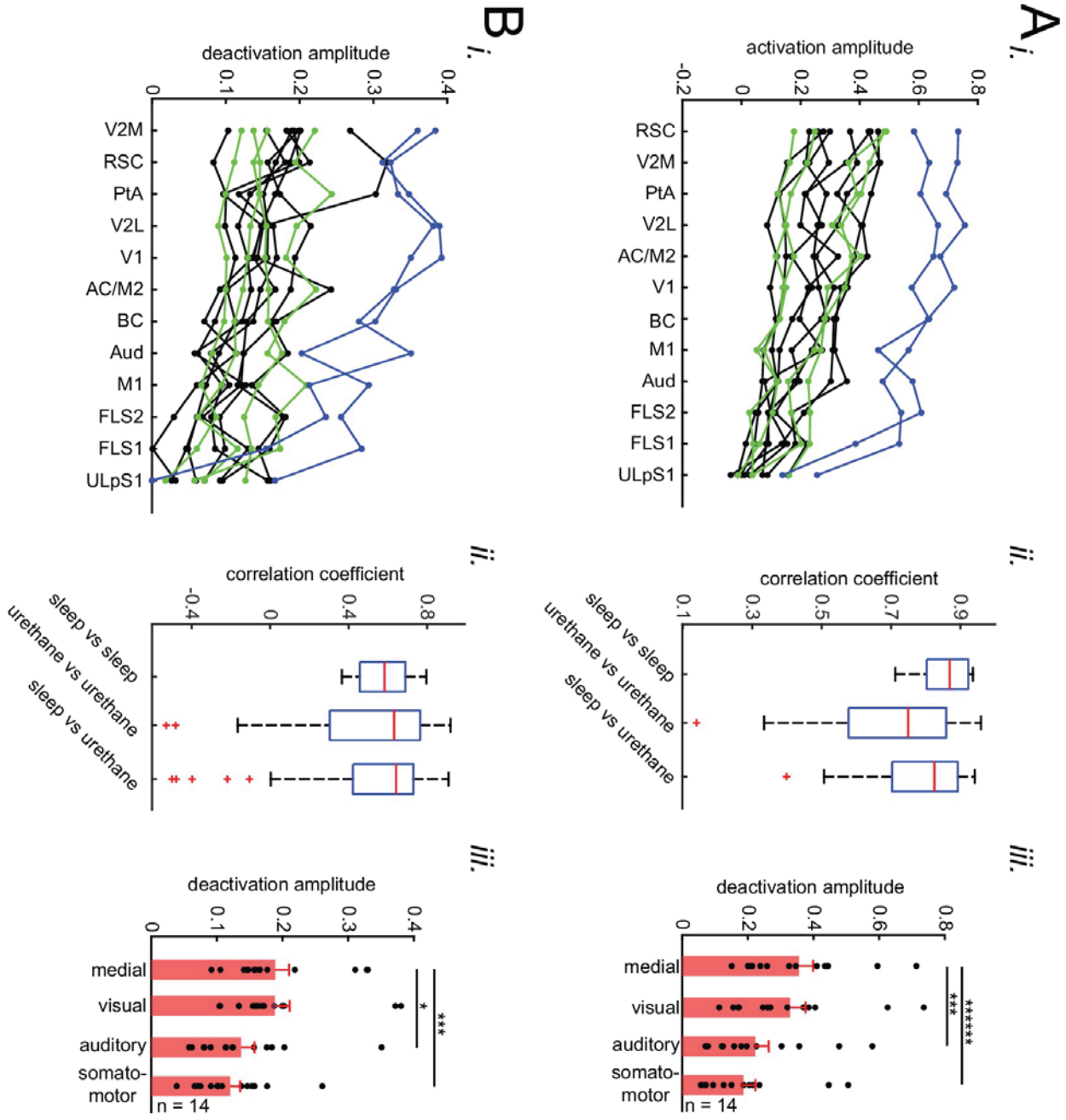

Figure 2.2 – S4. Differential modulation of neocortical regions does not depend on SWR detection threshold value. (**A**) (i) Peri-SWR activation amplitudes across neocortical regions sorted in the descending order. Each piece-wise linear curve connecting the activation amplitudes of neocortical regions is associated with a particular animal (n = 14). This data was generated using a higher SWR detection threshold (mean plus 3 (VSD) or 4 (iGluSnFR) times standard deviation of the ripple power signal) compared to that used to generate data presented in Figure 2 and Figure 2 – S 2 (mean plus 2 (VSD) or 3 (iGluSnFR) times standard deviation of the ripple power signal). (ii) Quantification of similarities between trends of peri-SWR activation amplitudes across neocortical regions under urethane anesthesia and natural sleep. The box plot shows the distribution of correlation coefficients between all possible pairs of traces associated with

natural sleep (green lines in i) and urethane anesthesia (blue and black lines in i). The Horizontal red lines represent the median of each distribution. As measured by correlation coefficients, there is no significant difference between peri-SWR activation amplitude trends under urethane anesthesia and natural sleep. (iii) Grand average (n = 14 animals) of peri-SWR activation amplitudes across neocortical subnetworks, sorted in decreasing activation amplitude. Each data point is the average of the activation amplitudes of all regions in a given subnetwork. (**B**) The same as in A but for peri-SWR deactivation amplitudes.

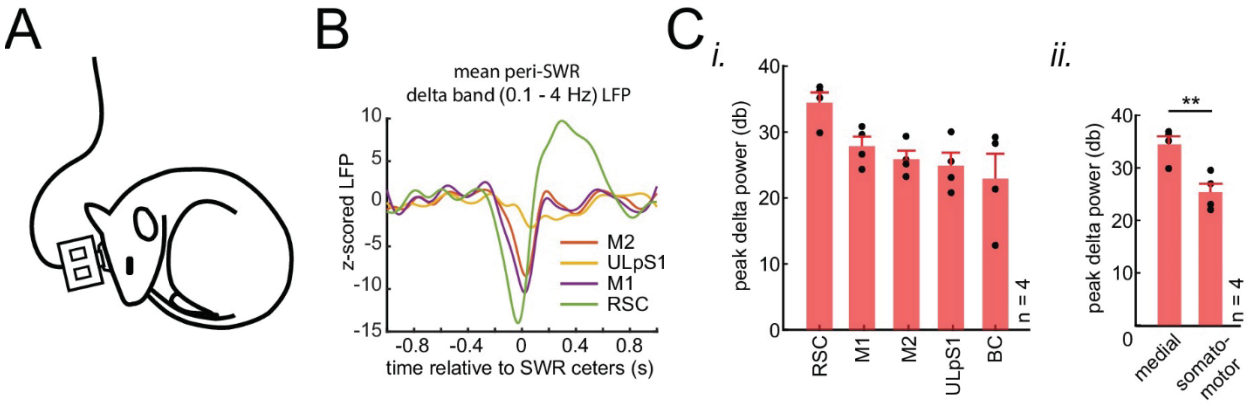

Figure 2.2 – S5. Differential modulation of neocortical activity, measured by LFP, around SWRs. (**A**) Schematic of electrophysiological recordings in naturally sleeping mice. (**B**) Example traces of mean peri-SWR neocortical LFP signals obtained during sleep. The neocortical LFP activity were filtered in delta band (0.1 - 4 Hz) across four neocortical regions including retrosplenial cortex (RCS), Primary and secondary motor cortex (M1 & M2), and upper lip somatosensory cortex (ULpS1). LFP filtered signal was z-scored with respect to a distribution of traces for each region, triggered around random timestamps generated by shuffling inter-SWR intervals. RSC, on average, shows the largest negative deflection (activation) and earliest onset around ripples times (0s). (**C**) (i) Group average (n = 4 animals) of delta-band peak power across neocortical regions, sorted in descending order. Z-scored delta power is reported in the logarithmic scale (decibels, db). RSC shows the largest delta power across all regions and animals. (ii) Grouping the data from four neocortical regions into neocortical subnetworks, defined in Figure 2C i, shows that medial subnetwork compared to the somatomotor subnetwork receive stronger modulation around hippocampal SWRs ($p < 0.01$, one-sided Wilcoxon signed-rank test).

2.3.3. Ripple power is distinctively correlated with peak activity in different neocortical subnetworks

Having observed that neocortical regions are strongly modulated around SWRs, we investigated whether the reverse is also the case, i.e. does ripple power increase when strong

activations take place in a given neocortical region? To address this question, the ripple power traces centered on peak activations (see Methods) in each neocortical pixel (or region of interest) were averaged and compared across neocortical subnetworks (**Figure 2.1E**). Ripple power indeed increased relative to peak neocortical activations, predominantly in regions that were most modulated around SWRs (**Figure 2.3A-B**). Ripple power increased most around peak activations in the visual and medial compared with auditory and somatomotor subnetworks (**Figure 2.3C;** n = 14 per subnetwrok; repeated measure ANOVA with Greenhouse-Geisser correction for sphericity: $F_{3,39} = 14.172$, $p = 1.8183\times10^{-5}$; post-hoc multiple comparison with Tuckey's correction: medial vs visual p = 0.99476, medial vs auditory p = 0.073032 [p = 0.0152 without Greenhouse-Geisser correction], medial vs somatomotor p = 0.00054029, visual vs auditory p = 0.030248, visual vs somatomotor p = 0.0010466, auditory vs somatomotor p = 0.17794).

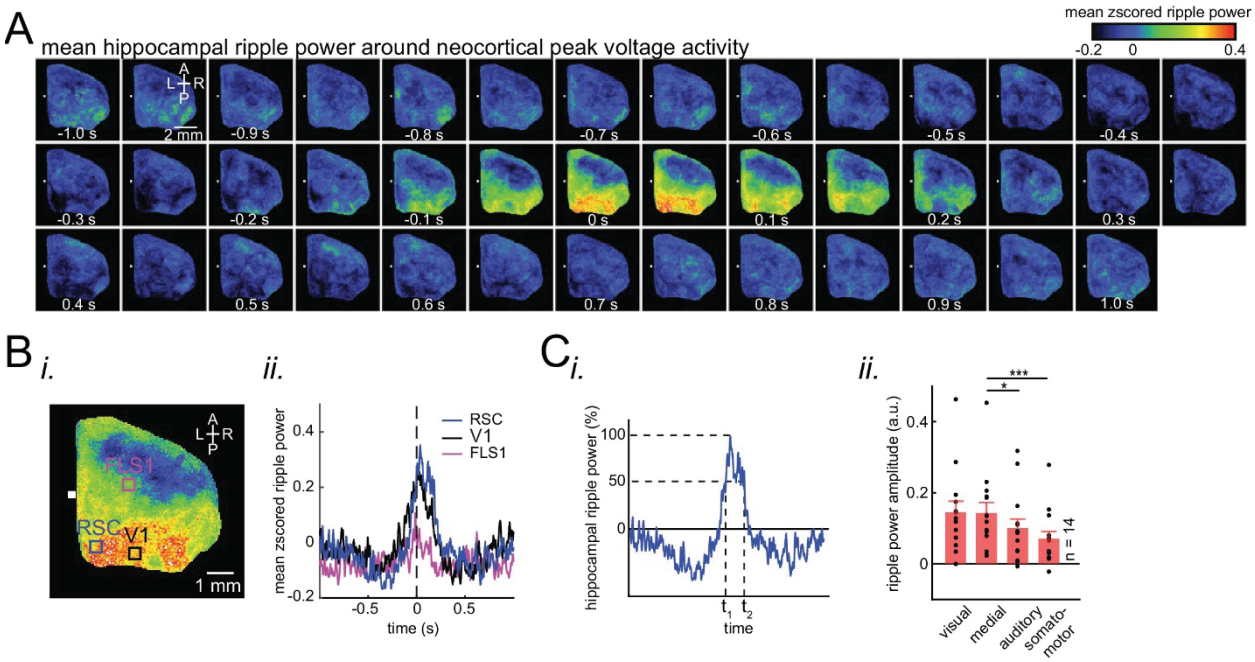

Figure 2.3. Ripple power is distinctively correlated with peak activity in different neocortical subnetworks. **(A)** Representative montage (50 ms intervals) showing spatiotemporal pattern of mean hippocampal ripple power fluctuations around the peak of neocortical activations. 0s-time indicates peak activation time in each neocortical pixel. Color bar represents the mean z-scored ripple power associated with peak activation in a given neocortical pixel. **(B)** (i-ii) A representative frame showing the spatial distribution of ripple power at neocortical peak activation time. Colored squares represent three regions of interest (retrosplenial, visual,

and forelimb somatosensory cortices in blue, black and magenta, respectively) for which their associated ripple power traces are displayed in (ii). **(C)** (i) Illustration of how the ripple power amplitude was quantified. Ripple power amplitude was defined as the mean ripple power signal across full-width at half maximum (t_1 to t_2). (ii) Grand average (n = 14 animals) of mean hippocampal ripple power amplitudes across neocortical subnetworks shown in Fig. 2Ci, sorted in decreasing order. Each data point is the average of hippocampal ripple power amplitudes associated with all the regions in a given subnetwork and in a given animal. Bar graphs indicate mean ± SEM. (repeated measure ANOVA with Greenhouse-Geisser correction for sphericity: $F_{3,39} = 14.172$, $p = 1.8183\times10\text{-}5$; post-hoc multiple comparison with Tuckey's correction: medial vs visual p = 0.99476, medial vs auditory p = 0.073032 [p = 0.0152 without Greenhouse-Geisser correction], medial vs somatomotor p = 0.00054029, visual vs auditory p = 0.030248, visual vs somatomotor p = 0.0010466, auditory vs somatomotor p = 0.17794). This figure has two Ss.

Thus, during natural sleep and under urethane anesthesia (**Figure 2.3 – S1**), the medial and visual subnetworks are more likely to be coordinated with hippocampal SWRs. Moreover, we investigated the relationship between neocortical slow oscillation and hippocampal SWRs in animals for which neocortical electrophysiological signals were recorded (**Figure 2.3 – S2**). We found that hippocampal ripple power is suppressed (elevated) before (after) the onset of neocortical up-states. Similarly, hippocampal ripple power is elevated (suppressed) before (after) the onset of neocortical down-states. Therefore, the results obtained using optical imaging and neocortical electrophysiology were compatible.

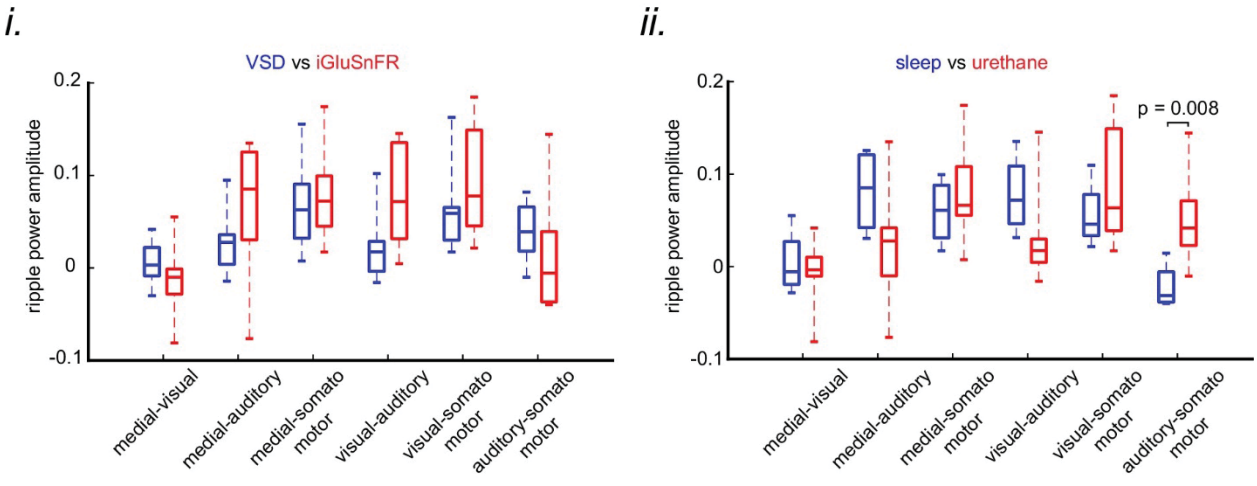

Figure 2.3 – S1. The correlation of ripple power with neocortical peak activity is similar under sleep/urethane anesthesia and VSD/iGluSnFR imaging conditions. The difference of ripple power

amplitudes (arithmetic subtraction) between all possible pairs of subnetworks is compared across VSD versus iGluSnFR (i) and sleep versus urethane anesthesia (ii) conditions. The only statistically significant result is from the difference auditory-somatosensory (auditory minus somatosensory) in sleep versus urethane comparison.

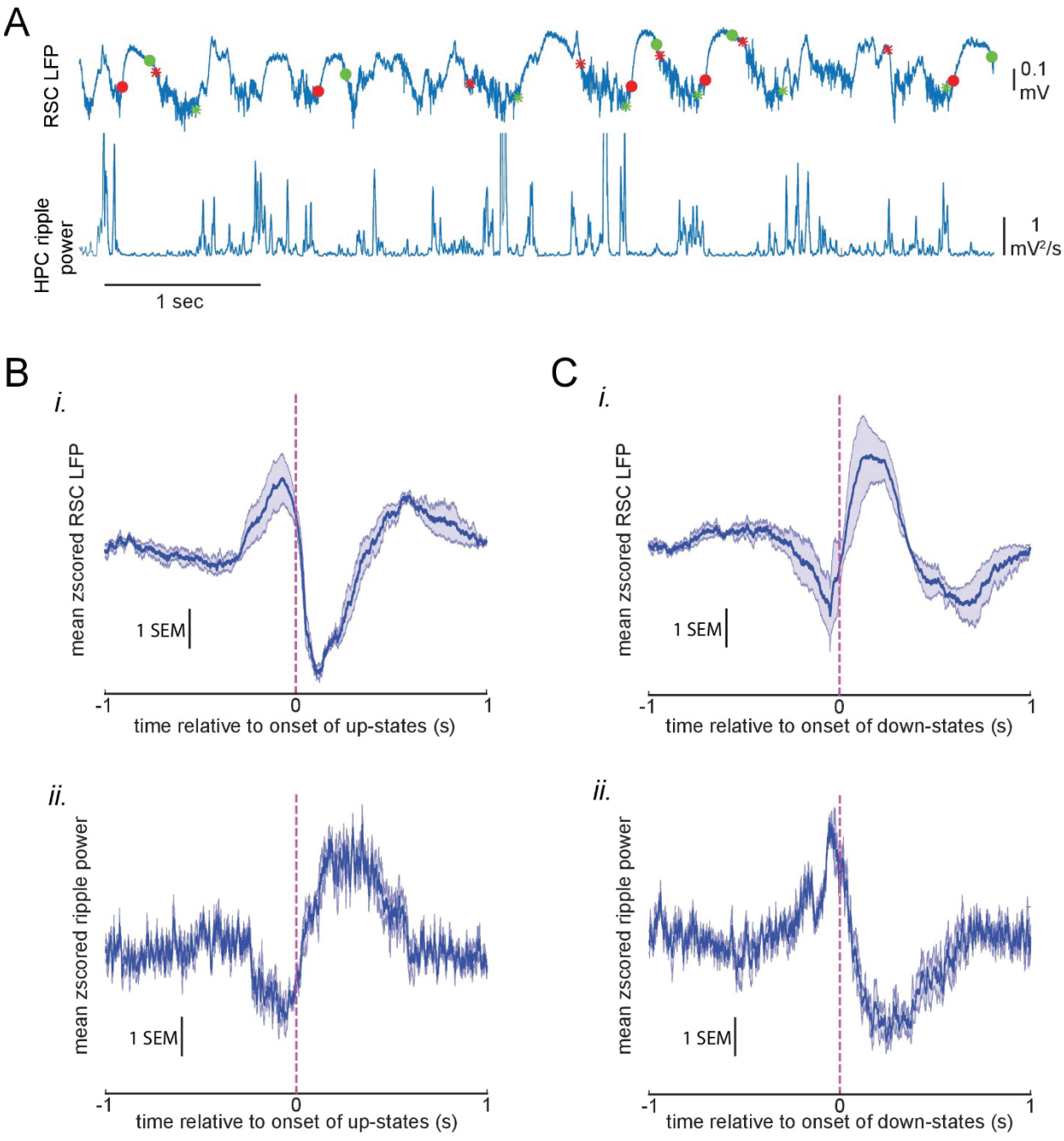

Figure 2.3 – S2. Modulation of hippocampal ripple power around neocortical up-/down-states. (**A**) Exemplar LFP signals recorded with a bipolar electrode from the retrosplenial cortex (RSC; top) and dorsal

CA1 of the hippocampus (filtered in ripple band, rectified, and smoothed; bottom) during slow oscillation. Red and green circles represent the onset and offset of detected RSC down-states, respectively. Similarly, red and green stars represent the onset and offset of detected RSC up-states, respectively. (**B**) Mean z-scored RSC LFP (i) and ripple power (ii) traces aligned to the onset of RSC up-states. The shaded area represents the SEM (n = 4 animals). Notice that the ripple power is suppressed and elevated before and after the onset of up-states, respectively. (**C**) Mean z-scored RSC LFP (i) and ripple power (ii) traces aligned to the onset of RSC down-states. The shaded area represents the SEM (n = 4 animals). Notice that the ripple power is elevated and suppressed before and after the onset of down-states, respectively.

2.3.4. Neocortex tends to activate sequentially from medial to more lateral regions around SWRs

After identifying which neocortical subnetworks are modulated around SWRs, we investigated the temporal order in which neocortical regions activated. The timestamp of the peak activity (t_p in **Figure 2.4Ai**) in the mean peri-SWR traces for each neocortical region was detected on an individual animal basis.

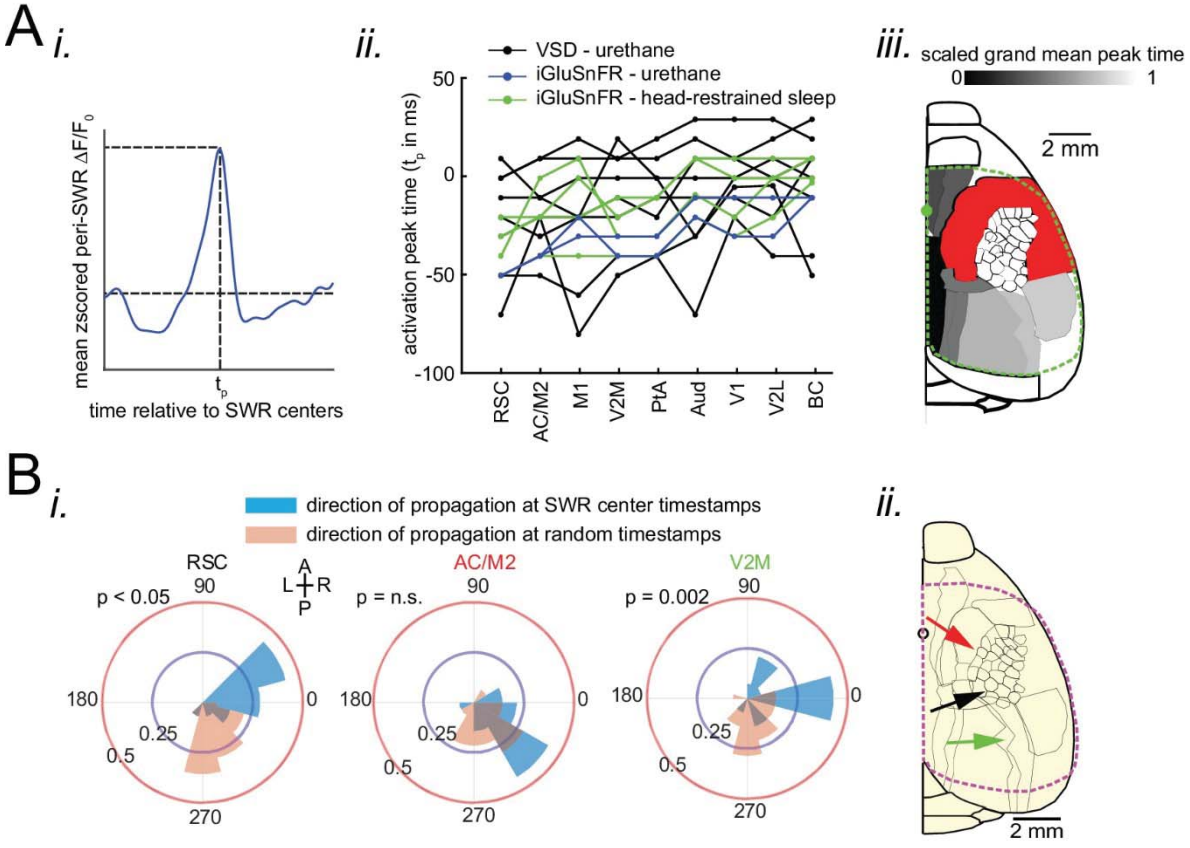

Figure 2.4. Neocortex tends to sequentially activate from medial to more lateral regions around SWRs. **(A)** (i) Demonstration of how peri-SWR neocortical activation peak time (t_p) was quantified. The mean peri-SWR neocortical activity trace was generated for each region (blue trace) and the timestamp of the peak was defined as t_p. (ii) Peri-SWR activation peak timestamp (t_p) relative to SWR centers (0s-time) across neocortical regions sorted in ascending order. Each line graph represents one animal. t_p values were not detected in some regions and in some animals (three data points in total), mainly because there was not a strong activation in those regions. Such missing data points were filled by average of available data points in the same region and in other animals (repeated measure ANOVA: F8,104 = 8.357195, $p < 0.0001$; post-hoc test for linear trend: slope = 0.003252024 second/region, $p < 0.0001$). (iii) Spatial map of peri-SWR activation peak time across all animals (n = 14) indicating a medial-to-lateral direction of activation. The red area was not included in this analysis because it was not activated strong enough to yield a reliable result. **(B)** (i) Circular distributions represent the direction of propagating waves of activity in three distinct neocortical regions at hippocampal SWR (blue distribution) and at random timestamps generated by shuffling inter-SWR time intervals (red distribution). 180-0 and 90-270 degrees represent the medio-lateral and antero-posterior axes, respectively. P-values come from Kuiper two-sample test. (ii) Schematic of propagation directions measured at SWR timestamps in three neocortical regions located in the medial neocortex. This figure has two figure supplements.

We then sorted peak activation times from earliest to latest relative to SWRs centers. A medial to lateral temporal gradient in peak times was observed across neocortical regions (**Figure 2.4Aii;** repeated measure ANOVA: $F_{8,104} = 8.357195$, $p < 0.0001$; post-hoc test for linear trend: slope = 0.003252024 second/region, $p < 0.0001$). The group average of peak times for each region across all animals also supported the medio-lateral direction of activations (**Figure 2.4Aiii; Figure 2.4 – S1; Figure 2.4 – S2**).

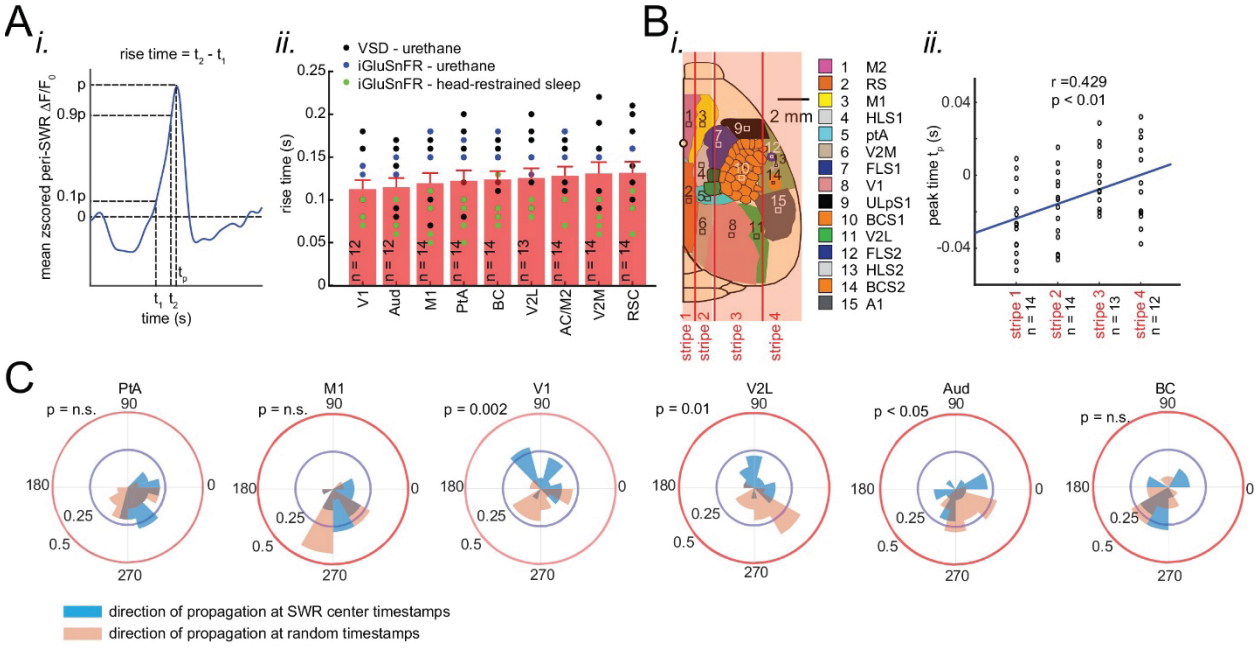

Figure 2.4 – S1. Neocortex tends to activate sequentially from medial to more lateral regions around SWRs. (**A**) (i) Demonstration of how peri-SWR neocortical activation rise time was measured. Rise time was calculated as the time which takes for the signal to reach 90% of the peak value starting from 10%. (ii) Summary of the mean peri-SWR activation rise time across neocortical regions from n=12-14 mice imaged during states of urethane anesthesia (blue and black dots) and head-restrained sleep (green dots). There is no significant difference in activation rise time across neocortical regions meaning that all imaged neocortical regions activate at the same rate. It suggests that activation peak time can reflect the activation time of a given region. The bar graphs are mean ± SEM. (**B**) Schematic representation of vertical stripes splitting the recorded neocortical regions from medial to lateral into four groups. (ii) There is a significant correlation ($r = 0.429$, $p < 0.01$, two-sided t-test) between stripe number and peak activation timestamp (t_p) indicating that the more lateral regions activate later than medial ones relative to hippocampal SWRs. Dots represent the average t_p across regions in each stripe and for each animal. (**C**) Circular distributions represent the direction of neocortical propagating waves of activation in a given region at hippocampal SWR timestamps (blue distribution) and at random timestamps generated by shuffling inter-SWR time intervals (red distribution). 180-0 degrees represent the medio-lateral and 90-270 degrees represent the antero-posterior axes (p-values are calculated based on Kuiper two-sample test).

To investigate whether significant directional order of activation can be observed on an individual SWR basis, rather than being driven by the mean across all SWRs, we iteratively applied optical flow analysis(Afrashteh et al., 2017) on mean peri-SWR neocortical activity around smaller subsets (n ~ 20) of randomly chosen SWRs and calculated the direction of propagation of activity

in each region (blue circular distribution in **Figure 2.4B and Figure 2.4 – S1C**). We observed that around SWRs, the waves of activity in medial neocortical regions showed the strongest medio-lateral directional component, and the strength of this directionality decreased in more lateral regions (**Figure 2.4B; Figure 2.4 – S1**). In order to verify that the directionalities observed in optical flow analysis were meaningful; we compared them to directionalities in the same region but during random timestamps generated by shuffling the inter-SWR time intervals (orange circular distribution in **Figure 2.4B; Figure 2.4 – S1C**) and found a statistical difference between the two circular distributions in several regions (**Figure 2.4B; Kuiper two-sample test; RSC $p < 0.05$; AC/M2 $p > 0.05$; V2M $p = 0.002$; Figure 4 – S 1C**).

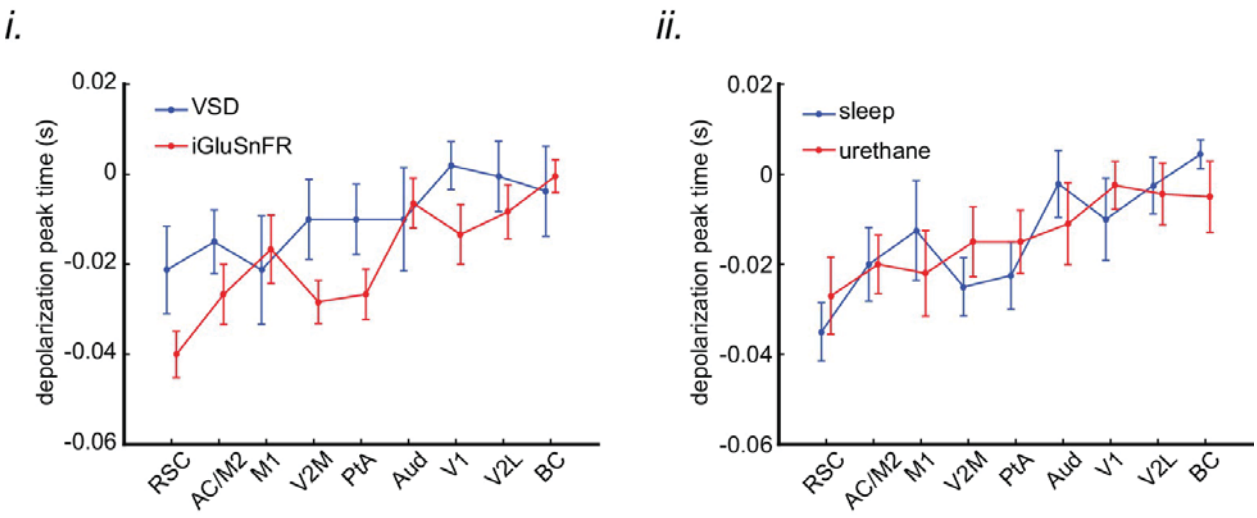

Figure 2.4 – S2. The order of sequential activation across neocortical regions around SWRs is similar under sleep/urethane anesthesia and VSD/iGluSnFR imaging conditions. The peak time of mean peri-SWR activation across neocortical regions is displayed for VSD versus iGluSnFR (i) and sleep versus urethane anesthesia (ii) conditions. The regions on the horizontal axes are sorted in an increasing order based on the average of all animals (n = 14) in each region. The linear trend in all the four conditions are statistically significant (repeated measure ANOVA follow-up test for linear trend; VSD: slope = 0.002665 s/region, iGluSnFR: slope = 0.004034 s/region, sleep: slope = 0.003968 s/region, and urethane: slope = 0.002966 s/region; All the p-values are less than 0.0001). Error bars represent standard errors.

2.3.5. Neocortical activation latency relative to SWRs spans a wide spectrum of negative to positive values

On average, neocortical voltage and glutamate activity tended to peak before SWRs in almost all of the imaged regions (**Figure 2.4Aii**). To investigate this temporal relationship further, we focused on RSC as an exemplar region, since it was the most modulated region around SWRs. Investigation on an individual SWR basis showed that the timings of RSC peak activity relative to SWRs forms a continuum spanning from negative (before) to positive (after) values (**Figure 2.5 – S1A**). To clarify what properties of SWRs co-vary with the temporal order of RSC activation relative to SWRs, we calculated an Asymmetry Index (AI) (**Figure 2.5A-B**) which is defined as the difference between mean activity in the intervals ± Δt after and before the SWRs center, divided by their sum, such that positive and negative values represent activity tending to follow or to precede the SWR, respectively. AI was used instead of peak time because, AI, which is calculated based on integral of a signal, is less noisy, and hence more reliable (**Figure 2.5 – S1B**).

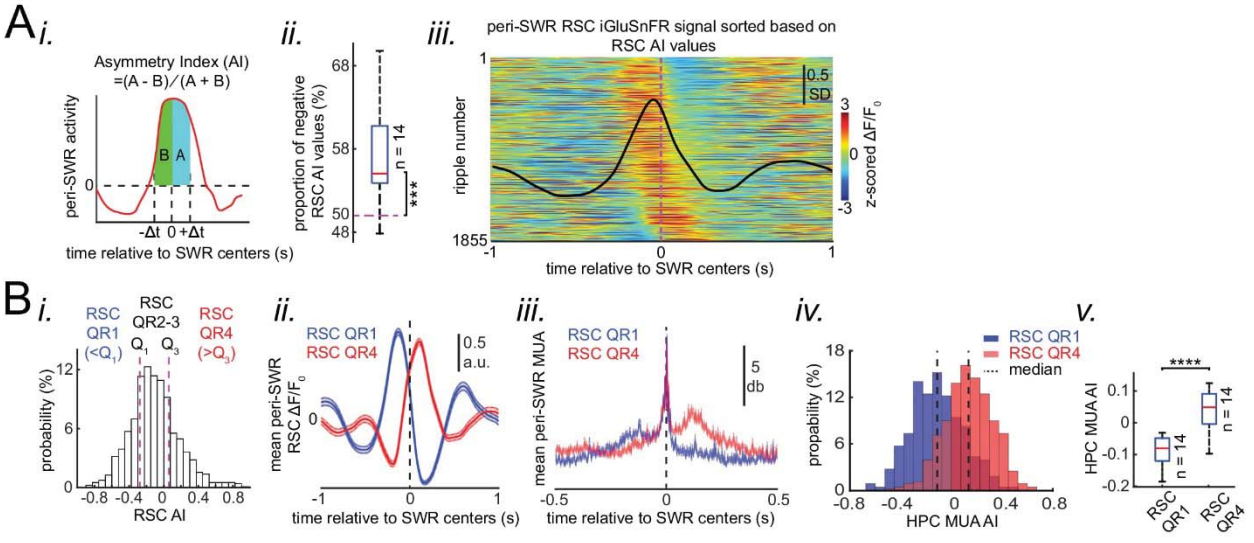

Figure 2.5. Neocortical activation latency relative to SWRs spans a wide spectrum of negative to positive values. **(A)** (i) Schematic of Asymmetry Index (AI) calculation. In this figure, AI was calculated for individual peri-SWR retrosplenial cortex (RSC) traces and called RSC AI. RSC AI values were used to

quantify the latency of neocortical activation relative to SWR timestamps. (ii) The proportion of negative RSC AI values across animals (n=14). Magenta dashed line indicates the chance level (50%). 55% (median, indicated by a red line) of peri-SWR RSC activity across animals have negative AI, meaning that on average, neocortical tendency to activate prior to hippocampal SWRs is greater than chance (n = 14; one-sided one-sample Wilcoxon signed-rank test; the median is greater than 0.5 with $p = 1.831\times10^{-4}$). (iii) Representative peri-SWR RSC activity sorted by AI calculated for each individual peri-SWR RSC trace. Color bar represents z-scored iGluSnFR signal. The black trace shows the mean peri-SWR RSC iGluSnFR signal. Note that the chance of neocortical activation preceding SWRs is higher than following them. **(B)** (i) Distribution of RSC AI values for a representative animal. Dashed lines indicate the first (Q_1) and third quartiles (Q_3). The SWRs for which the associated RSC AI values are less and greater than Q_1 and Q_3 are called RSC QR1 and QR4, respectively. RSC QR2-3 consists of all other SWRs. (ii) Example plots of mean peri-SWR RSC iGluSnFR signal associated with RSC QR1 (blue) and QR4 (red). The thickness of the shading around each plot indicates SEM. Note that the activity associated with RSC QR1 and QR4 peak before and after SWR centers, respectively. (iii) Time course of exemplar mean peri-SWR hippocampal MUA associated with SWRs in RSC QR1 (blue) and RSC QR4 (red). Notice that both hippocampal MUA activity and RSC iGluSnFR activity are negatively (negative AI) and positively (positive AI) skewed for RSC QR1 and QR4, respectively. (iv) Distributions of hippocampal MUA AI values for SWRs in RSC QR1 (blue) and QR4 (red) in a representative animal. The vertical line represents the median of each distribution. (v) Summary of median values calculated in (iv) across all animals (n = 14, one-sided paired Wilcoxon signed-rank test; RSC QR1 versus RSC QR4 $p = 6.103\times10^{-5}$). This figure has three figure supplements.

AIs were calculated for peri-SWR RSC traces, and are referred as RSC AI (**Figure 2.5A-B**). As expected, RSC AI values were strongly correlated with AI values similarly calculated for regions in medial and visual subnetworks (PtA = 0.78 ± 0.03; AC/M2 = 0.78 ± 0.02; V2M = 0.897 ± 0.01; V1 = 0.67 ± 0.02; V2L = 0.68 ± 0.02; Aud = 0.51 ± 0.03; M1 = 0.46 ± 0.04; BC = 0.53 ± 0.02; FLS1 = 0.38 ± 0.03; ULpS1 = 0.23 ± 0.04). We then partitioned the distribution of RSC AI values into lower and higher quartile ranges (QR) according to whether the RSC AI range fell below the first quartile (RSC QR1) or above the third quartile (RSC QR4) (**Figure 2.5B**). Interestingly, when neocortical activity tended to precede the SWRs there was a buildup of hippocampal MUA preceding the SWRs as well, whereas when the neocortex activation followed the SWRs, the hippocampal MUA likewise followed. In other words, the HPC AI values for SWRs in RSC QR1 were less than those for SWRs in RSC QR4, and the HPC AI values for SWRs in

RSC QR1 and RSC QR4 were more negative and positive, respectively (**Figure 2.5Bii-v;** n = 14 per group in Figure 2.5Bv; one-sided paired Wilcoxon signed-rank test; RSC QR1 versus RSC QR4 $p = 6.103\times10^{-5}$). This pattern suggests that the hippocampus and neocortex may engage in waves of mutual excitation in which a SWR may occur at any time before, during or after the peak of the hippocampal-neocortical activation.

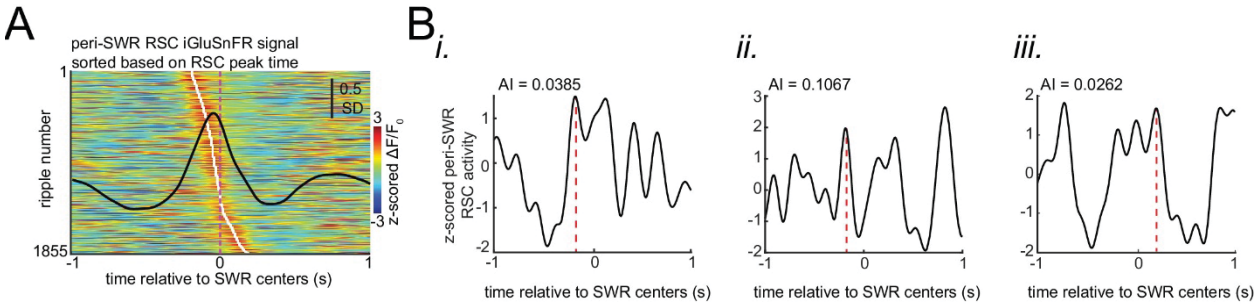

Figure 2.5 – S1. Asymmetry Index is a more robust measure of activation latency compared to peak activation timestamp**.** (**A**) Peri-SWR RSC activity for individual SWRs sorted by peak timestamps detected in (-200 ms, 200 ms) interval. Peak timestamps were calculated for each individual peri-SWR RSC trace. Color bar represents the z-scored iGluSnFR signal. The black trace shows the mean peri-SWR RSC iGluSnFR trace. (**B**) (i-iii) Asymmetry index (AI), calculated for three representative traces of peri-SWR RSC activity patterns, is shown to demonstrate that the peak time may not accurately reflect the timing of activation relative to SWRs. In these examples, the peak timestamp (magenta lines) for the first two and for the third examples occur before and after the SWR time (0 s), respectively, suggesting that the corresponding SWRs have occurred in the late and early phases of RSC activation, respectively. However, the RSC AI values for these three traces do not match with this conclusion. Instead, the RSC AI values suggest that their corresponding SWRs have occurred around the middle phase of RSC activation for the first (AI = 0.0385) and third (AI = 0.0262) time traces because their corresponding AI values are close to zero, and at the early phase of RSC activation for the second (AI = 0.1067) time trace because its corresponding AI value is positive and away from zero.

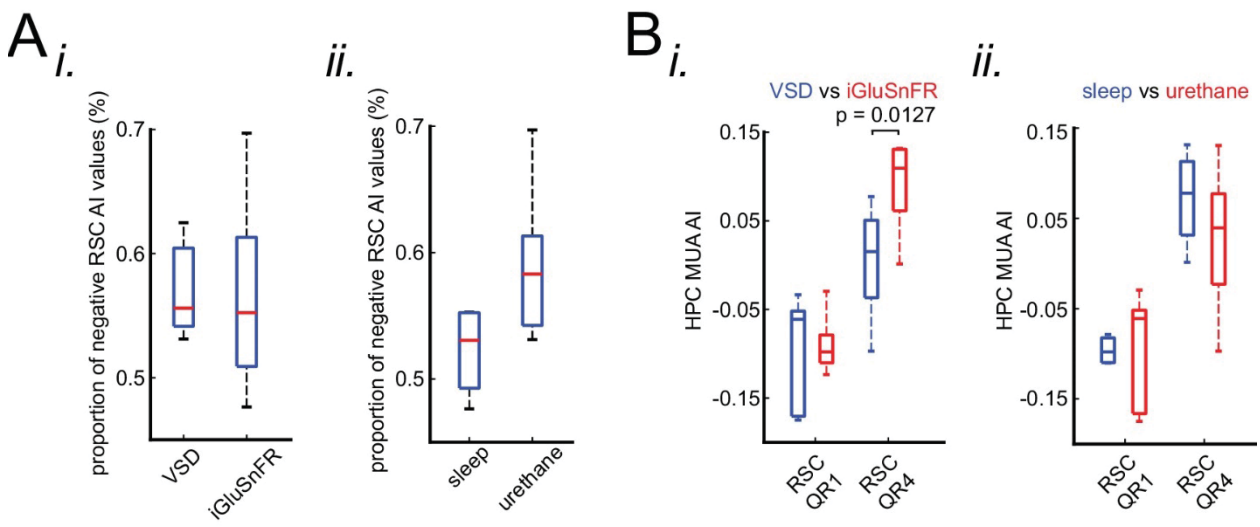

Figure 2.5 – S2. Neocortical activation latency relative to SWRs is similar under sleep/urethane anesthesia and VSD/iGluSnFR imaging conditions. **(A)** There is no statistically significant difference in the proportion of negative RSC AI values in VSD versus iGluSnFR (i) nor in sleep versus urethane (ii) conditions. **(B)** The comparison of the distribution of medians of HPC MUA AI values across RSC QR1 and RSC QR4 in VSD versus iGluSnFR (i) and in sleep versus urethane (ii) conditions. A statistically significant difference was observed in comparing the HPC MUA AI median values for RSC QR4 in VSD versus iGluSnFR.

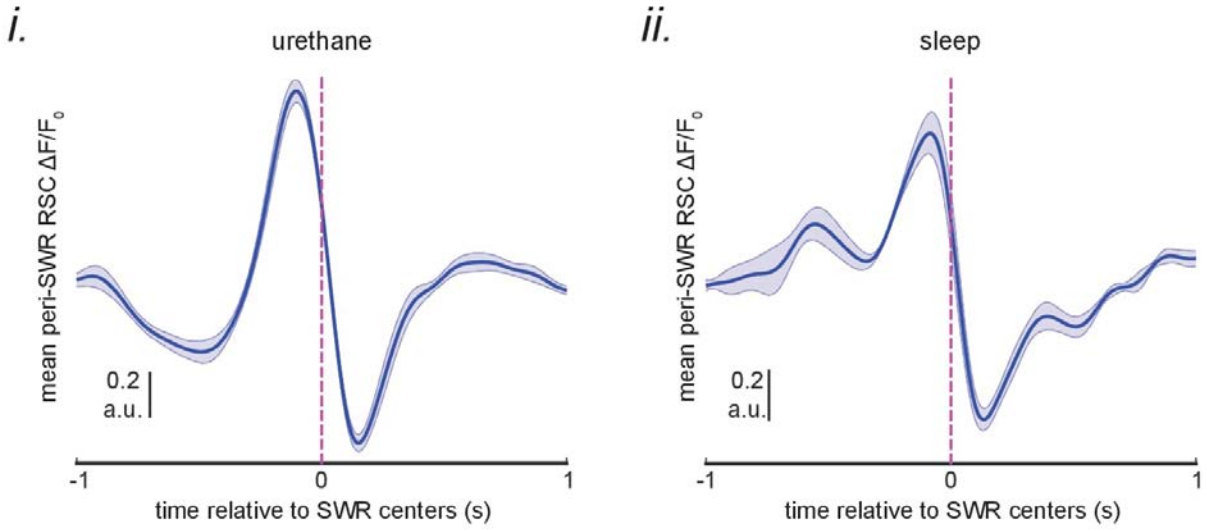

Figure 2.5 – S3. A delayed neocortical activation after SWRs in RSC QR1 was not observed. The mean of the peri-SWR RSC activity for SWRs in the RSC QR1 (blue curve shown in **Figure 2.5Bii**) were calculated for each animal and then the resultant signals were averaged across urethane-anesthetized (i) and sleeping (ii) animals separately.

2.3.6. Skewness of peri-SWR hippocampal MUA informs the neocortical activation latency relative to SWRs

We then investigated the inverse question, whether skewness of hippocampal MUA is a SWR-associated feature that correlates with whether neocortical activity precedes or follows SWRs. To do so, AI was calculated for peri-SWR hippocampal MUA traces, and the corresponding calculated AIs were referred to as HPC MUA AI (**Figure 2.6Ai**). Then, the proportion of SWRs whose RSC and HPC MUA AI values matched in sign (indicating either both preceded or both followed SWRs) were calculated. We found that, on average, only ~61% of SWRs have sign-matched RSC and HPC MUA AI values (**Figure 2.6Aii; significantly above the chance level of 50%; two-sided Wilcoxon signed rank test p = 1.220703125×10^{-4}**). Moreover, the correlation coefficient between HPC MUA and RSC AI values was low but significant (r = ~0.3; n = 11725; two-sided

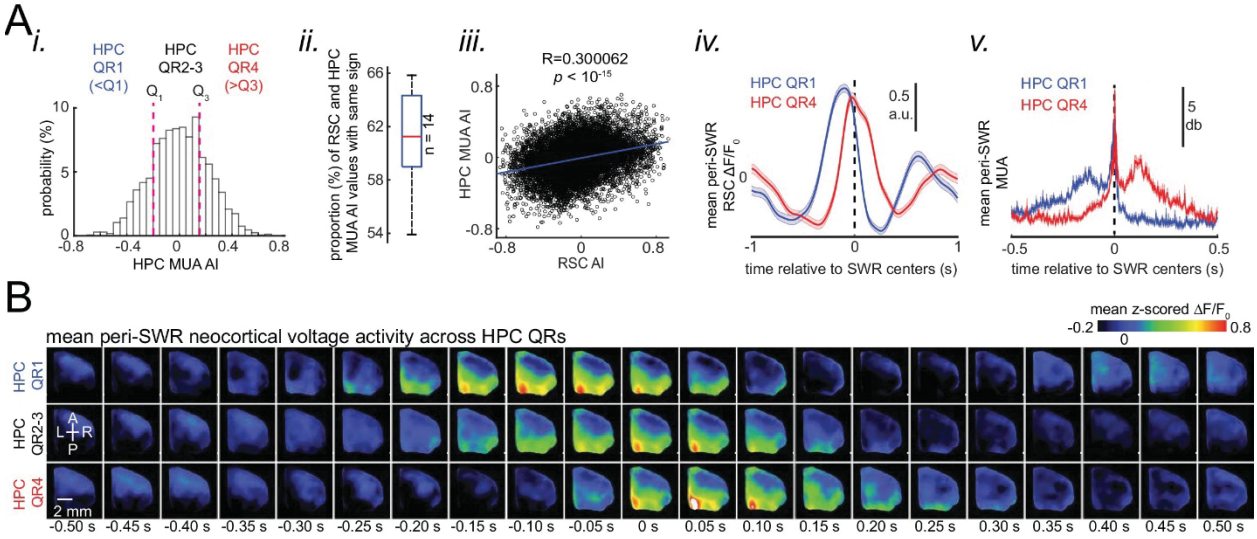

Figure 2.6. Skewness of peri-SWR hippocampal MUA informs neocortical activation latency relative to SWRs. **(A)** (i) Distribution of hippocampal MUA AI values for a representative animal. Dashed lines (Q_1 and Q_3) indicate the first and third quartiles. The SWRs for which the associated hippocampal MUA AI values are less than Q_1 and greater than Q_3 are called HPC QR1 and QR4, respectively. HPC QR2-3 consists of all other SWRs. (ii) Distribution of the proportion of SWRs in each animal for which the sign of both RSC and hippocampal MUA AI values match, as an indication of how well hippocampal MUA can inform

whether RSC activity precedes or follows SWRs. The horizontal red line indicates the median of all proportion values in n = 14 animals (significantly above the chance level of 50%; two-sided Wilcoxon signed rank test p = 1.220703125×10-4). (iii) Correlation between the RSC and hippocampal MUA AI values pooled across all animals (14 animals) is low but significant (n = 11725 SWRs across all animals; two-sided t-test $p < 10^{-15}$). (iv) Example plots of mean peri-SWR RSC glutamate activity associated with HPC QR1 (blue) and QR4 (red). (v) Time course of exemplar mean peri-SWR HPC MUA traces associated with SWRs in HPC QR1 (blue) and Q4 (red). Notice that both HPC MUA activity (v) and RSC glutamate activity (iv) are negatively skewed (negative AI) for HPC QR1, and the converse is true for HPC QR4. **(B)** Mean neocortical voltage activity centered on SWR centers associated with HPC QR1, QR2-3, and QR4 in a representative animal. Note the relative temporal shift in activity across three quartile ranges. This figure has two figure supplements.

t-test $p < 10^{-15}$; **Figure 2.6Aiii**). We then partitioned the distribution of HPC MUA AI values into lower and higher quartile ranges according to whether the HPC MUA AI range fell below the first quartile (HPC QR1) or above the third quartile (HPC QR4) (**Figure 2.6Ai**). We found that SWRs, preceded or followed by MUA (HPC QR1 vs QR4), were similarly preceded or followed by RSC activity, respectively (**Figure 2.6Aiv-v; Figure 2.6 – S1**). The effects observed for RSC activity can be generalized to other neocortical regions (**Figure 2.6B**). Thus, these results suggest that elevation of hippocampal MUA is correlated with neocortical activation independent of the timestamp at which SRWs occur.

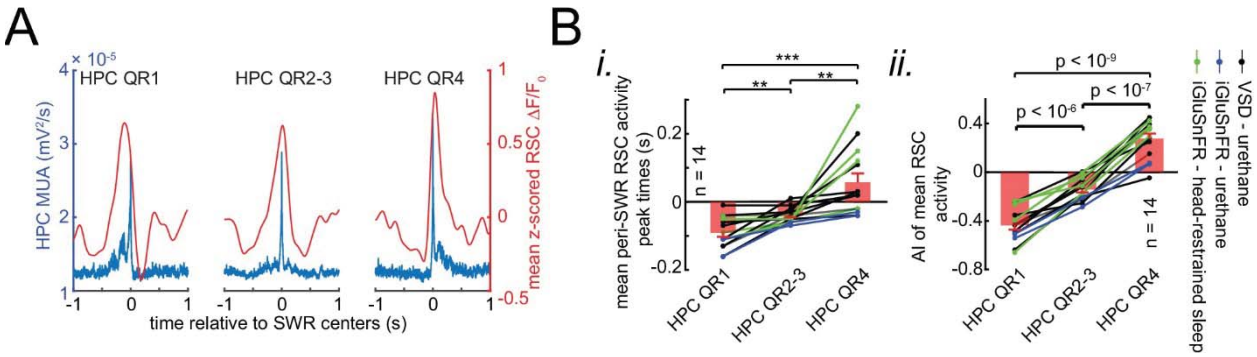

Figure 2.6 – S1. Whether retrosplenial cortex activation precedes or follows SWRs is correlated by skewness peri-SWR hippocampal MUA. (**A**) Representative mean peri-SWR RSC activity (red traces) and hippocampal MUA (blue traces) calculated for hippocampal SWRs in HPC QR1, QR2-3, and QR4 defined in Figure 2.6A i. Notice that skewness of RSC activity and hippocampal MUA matches in each plot. (**B**) (i-ii) Group data (n = 14) representing the peak timestamps (i) and AI values (ii) calculated from mean peri-

SWR RSC traces (red traces in panel A). Both graphs show that mean peri-SWR activation tends to precede and follow the SWRs in HPC QR1 and QR4, respectively. Bar graphs represent mean ± SEM.; **p<0.01, ***p<0.001, one-sided paired t-test.

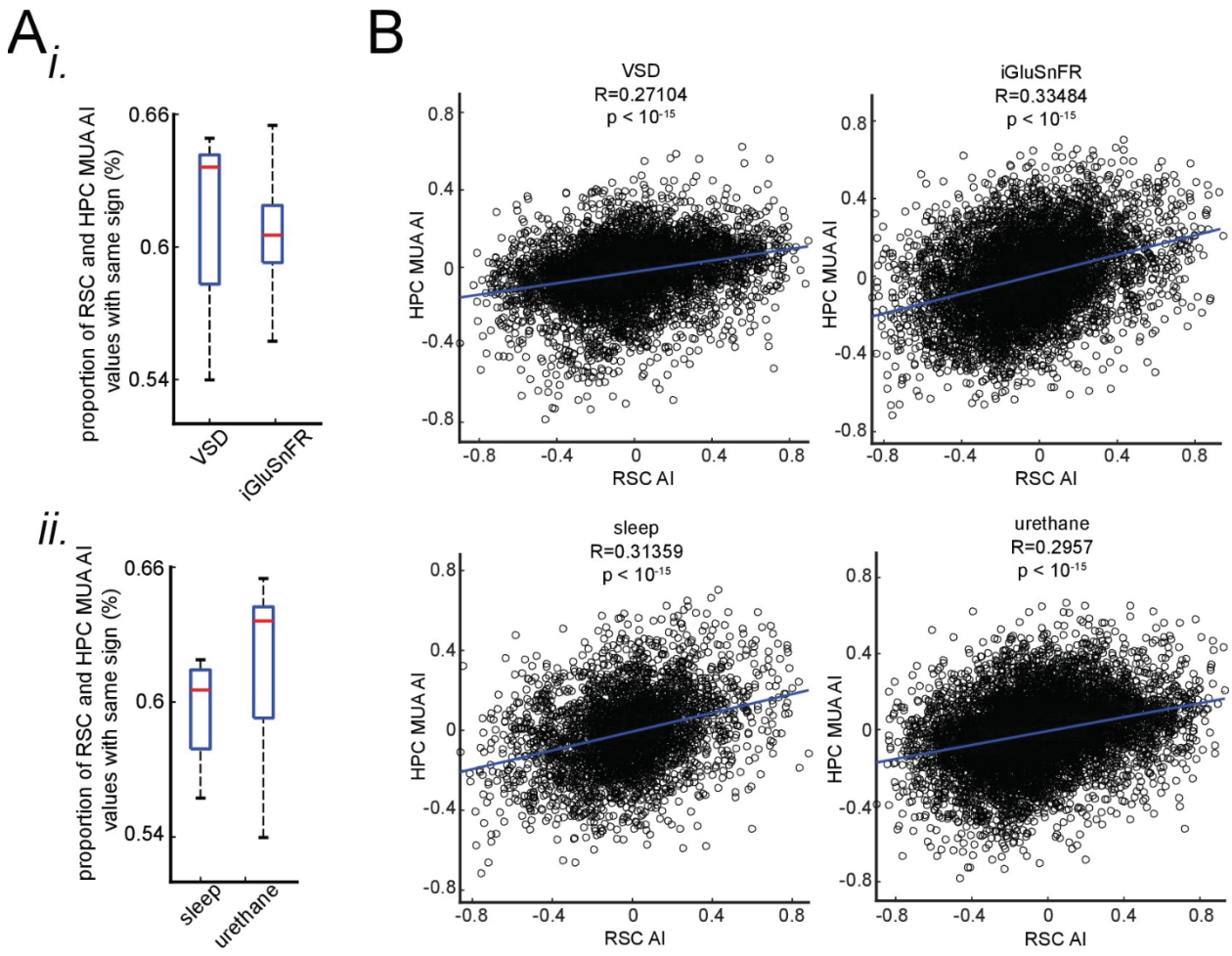

Figure 2.6 – S2. The correspondence between neocortical activation latency relative to SWRs and skewness of peri-SWR hippocampal MUA is similar under sleep/urethane anesthesia and VSD/iGluSnFR imaging conditions. **(A)** There is no statistically significant difference in the proportion of RSC and HPC MUA AI values with the same sign in VSD versus iGluSnFR (i) nor sleep versus urethane (ii) conditions. **(B)** The correlation coefficients between RSC and HPC MUA AI values are statistically significant across all four conditions and are close to each other.

2.3.7. Occurrence of single/isolated ripples versus ripple bundles correlates with whether RSC activation precedes or follows hippocampus

Although the skewness of peri-SWR MUA informs the variations in neocortical activation latency relative to SWRs, it does so to a weak extent (**Figure 2.5B and 2.6A**), suggesting that additional factors, other than skewness of peri-SWR HPC MUA, are required to predict whether neocortex precedes or follows hippocampus around SWRs.

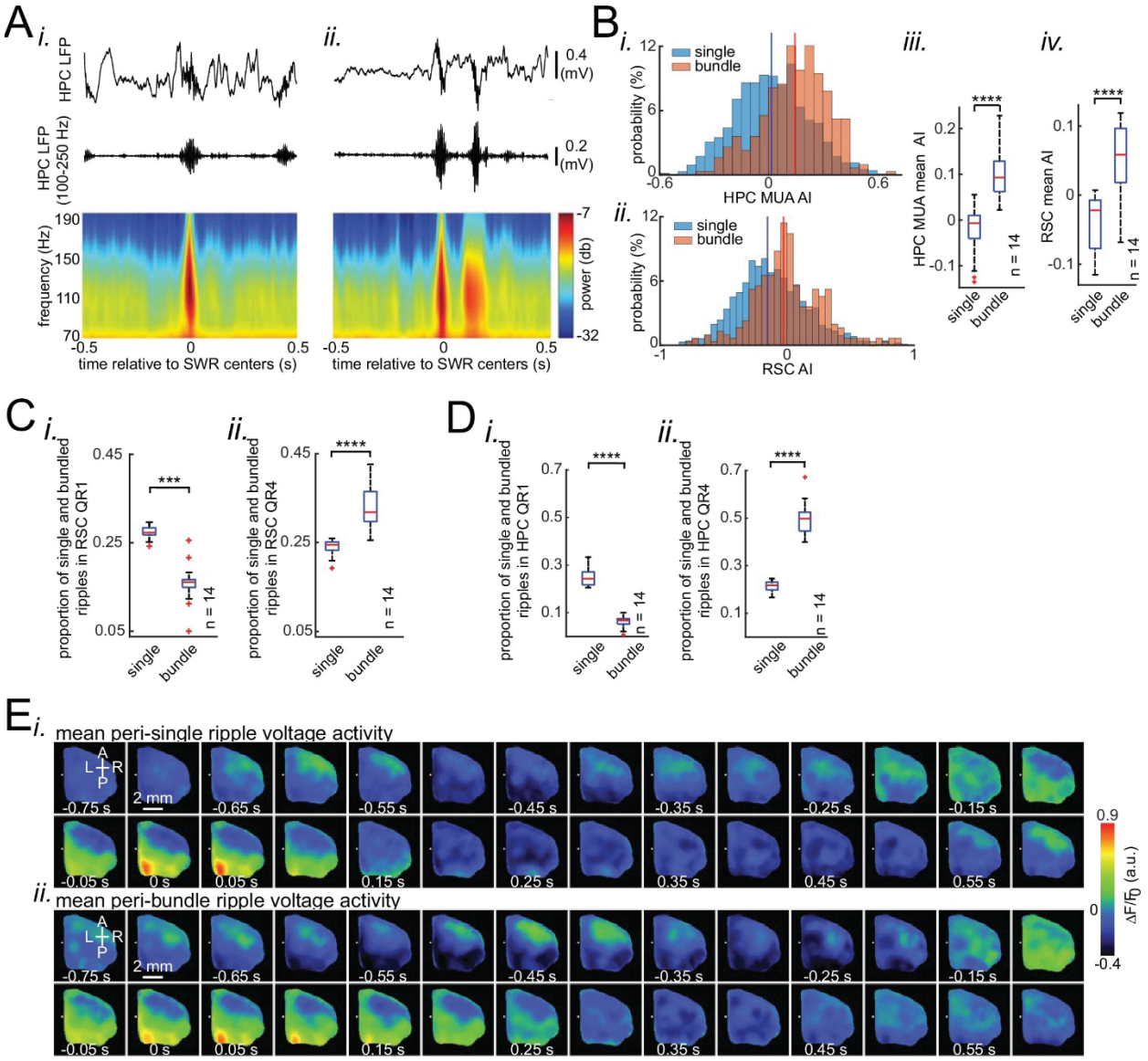

Figure 2.7. Occurrence of single/isolated ripples versus ripple bundles correlates with whether RSC activation precedes or follows hippocampus. **(A)** Example raw hippocampal LFP signal (top row), ripple-band filtered signal (middle row), and mean peri-SWR spectrogram (bottom row) displaying (i) single/isolated and (ii) bundled ripples. **(B)** Distribution of HPC MUA (i) and RSC (ii) AI values calculated for single/isolated (blue) and bundled (red) ripples in a representative animal. The blue and red vertical lines represent the means of blue and red distributions, respectively. As expected, the red distribution is shifted to the right with respect to the blue one. (iii-iv) Comparison of HPC MUA (iii) and RSC (iv) AI mean values for single/isolated and bundled ripples (n = 14; one-sided paired Wilcoxon signed-rank test; in iii $p = 6.103\times10^{-5}$; in iv $p = 6.103\times10^{-5}$). The red plus signs represent the data points outside the interval (centered on median value) which includes 99.3 percent of all data points. Red horizontal lines represent the medians. **(C-D)** Summary data from n = 14 mice representing the proportion of single/isolated versus bundled ripples fell in RSC (C) and HPC (D) QR1 (i) and QR4 (ii). Note that there is a higher chance for single/isolated ripples to lie in RSC or HPC QR1 and higher chance for bundled ripples to fall in RSC or HPC QR4 (one-sided paired Wilcoxon signed-rank test; in C $p = 1.221\times10^{-4}$; in D $p = 6.103\times10^{-5}$). **(E)** (i-ii) Representative montages of mean neocortical voltage activity centered on single/isolated ripples (i) and the first ripple in bundled ripples (ii). Notice that neocortex stays active longer and peaks later around bundled versus single/isolated ripples. Moreover, there is strong neocortical deactivation preceding bundled ripples. This figure has two figure supplements.

We found that the occasional occurrence of 'bundle' of two or more SWRs(Davidson et al., 2009b; Wu and Foster, 2014) was another factor correlating with peri-SWR neocortical activity latency (**Figure 2.7; Figure 2.7 – S1**). On average, neocortex stayed active for a longer time and peaked later around the bundled than single/isolated ripples (**Figure 2.7 – S1A-C**). This observation suggests that there is a higher chance for the neocortex to follow the bundled ripples compared to the single/isolated ones (**Figure 2.7B-E; Figure 2.7 – S1C**). Interestingly, the neocortical deactivation preceding SWRs was stronger in bundled than isolated ripples**,** pointing to the strength of neocortical down-states as a predictor of occurrence of bundled ripples (**Figure 2.7 – S1Dii**). Moreover, the neocortical activation was stronger around bundled than isolated ripples (**Figure 2.7 – S1Cii**)**.**

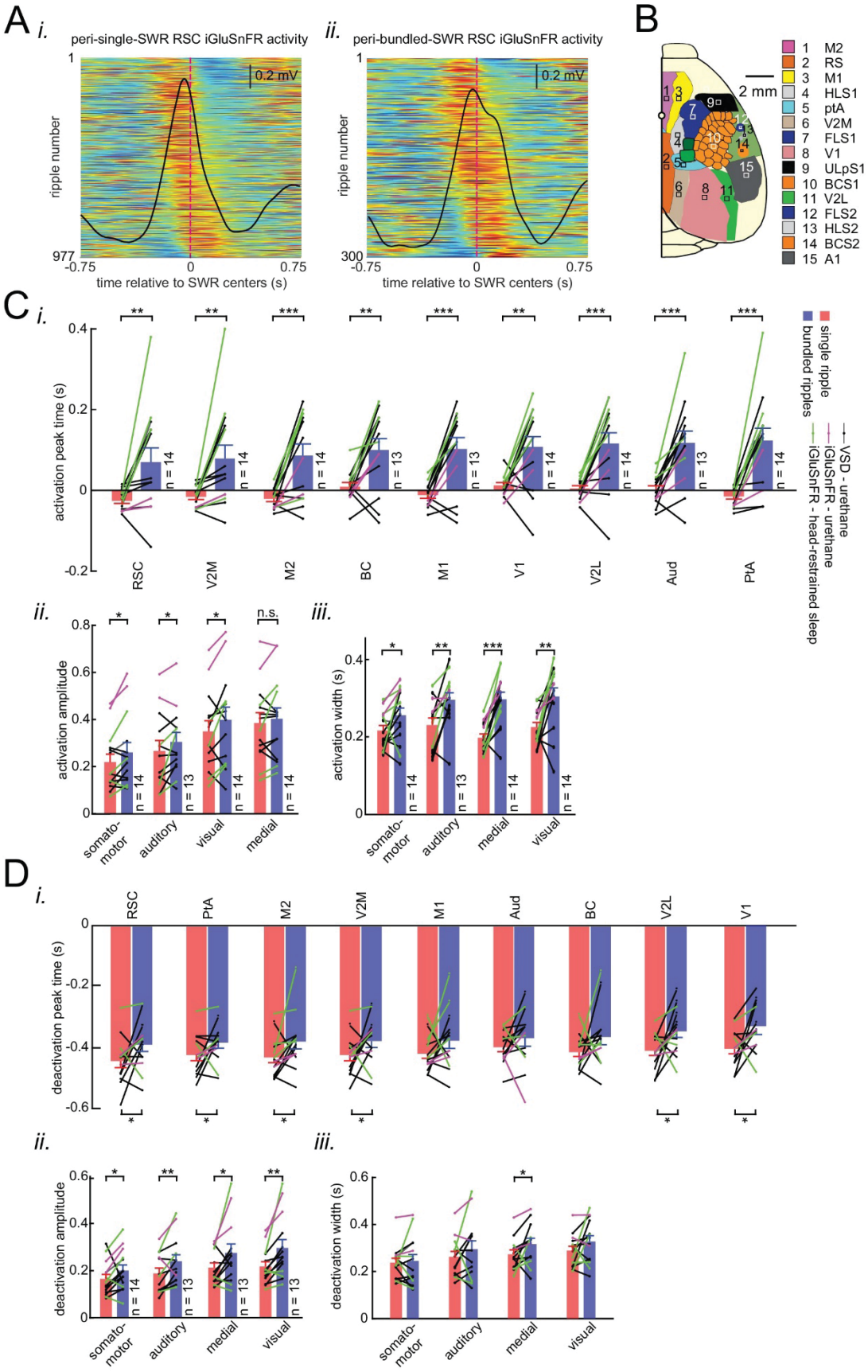
A
i.
peri-single-SWR RSC iGluSnFR activity
ripple number
0.2 mV
time relative to SWR centers (s)
ii.
peri-bundled-SWR RSC iGluSnFR activity
B
2 mm
1 M2
2 RS
3 M1
4 HLS1
5 ptA
6 V2M
7 FLS1
8 V1
9 ULpS1
10 BCS1
11 V2L
12 FLS2
13 HLS2
14 BCS2
15 A1
C
i.
activation peak time (s)
RSC
V2M
M2
BC
M1
V1
V2L
Aud
PtA
single ripple
bundled ripples
VSD - urethane
iGluSnFR - urethane
iGluSnFR - head-restrained sleep
ii.
activation amplitude
iii.
activation width (s)
somato-motor
auditory
visual
medial
n.s.
D
i.
deactivation peak time (s)
ii.
deactivation amplitude
iii.
deactivation width (s)

Figure 2.7 – S1. Distinct latency, strength, and duration of neocortical modulation around single/isolated versus bundled ripples. (**A**) (i-ii) Peri-SWR RSC activity for individual single/isolated (i) and bundled (ii) SWRs sorted by RSC asymmetry index. Asymmetry indices were calculated for each individual peri-SWR RSC trace. Color bar represents the z-scored iGluSnFR signal. The black trace shows the mean peri-SWR RSC iGluSnFR trace. The peri-SWR RSC traces in bundled ripples are wider and cover longer post-ripple time durations, demonstrating the reason why the distribution of RSC Asymmetry Index (AI) values for bundled ripples tends to have larger median values compared to single/isolated ripples. (**B**) Schematic of a cranial window for optical imaging of neocortical voltage or glutamate activity. The voltage or glutamate activity was recorded from the dorsal surface of the right neocortical hemisphere, containing the specified regions. The abbreviations denote the following cortices AC/M2: anterior cingulate/secondary Motor, RS: retrosplenial, M1: primary motor, HLS1: hindlimb primary somatosensory, PtA: posterior parietal, V2M: secondary medial visual, FLS1: forelimb primary somatosensory, TrS1: trunk primary somatosensory, ShNcS1: shoulder/neck primary somatosensory, V1: primary visual, ULpS1: lip primary somatosensory, BCS1: primary barrel, V2L: secondary lateral visual, S2: secondary somatosensory, A1: primary auditory. (**C-D**) Neocortical activation (C) and deactivation (D) peak timestamps (i), activation amplitudes (ii), and durations (iii) across neocortical regions around single/isolated versus bundled ripples. Such deactivations always precede SWRs. Notice that the neocortical activation and deactivation peak timestamp is significantly larger around bundled compared to isolated ripples in all (almost all for deactivation) neocortical regions. Moreover, the significant difference in activation and deactivation amplitudes around isolated versus bundled ripples is observed in all neocortical subnetworks (except the medial one for activation). The duration of neocortical activation is longer in all neocortical subnetworks around bundled compared to single/isolated ripples while that of deactivation is longer only in the medial subnetwork (*$p<0.05$, **$p<0.01$, ***$p<0.001$, n.s. $p > 0.05$, paired t-test; n=13-14 mice). All bar graphs represent mean ± SEM.

Although short inter-SWR intervals leading to ‘bundles’ of ripples can simply be a result of an underlying Poisson process, it is possible that bundled ripples constitute a random process different from that of single/isolated events. If the former is true, then the inter-SWR interval should be an exponential distribution(Shen and McNaughton, 1996). The inter-SWR time interval distribution of SWRs occurrence was well modeled by an exponential curve (linear curve in logarithmic scale) only for intervals longer than ~250 ms (single/isolated ripples). However, for shorter intervals (bundled ripples), there was an excess of positive residuals of the fitted exponential curve (**Figure 2 – S2E**). This suggests that the mechanisms of SWR generation when they occur in close temporal proximity to each other obeys a non-Poisson dynamic, constituting a different random process from that of single/isolated ripple events.

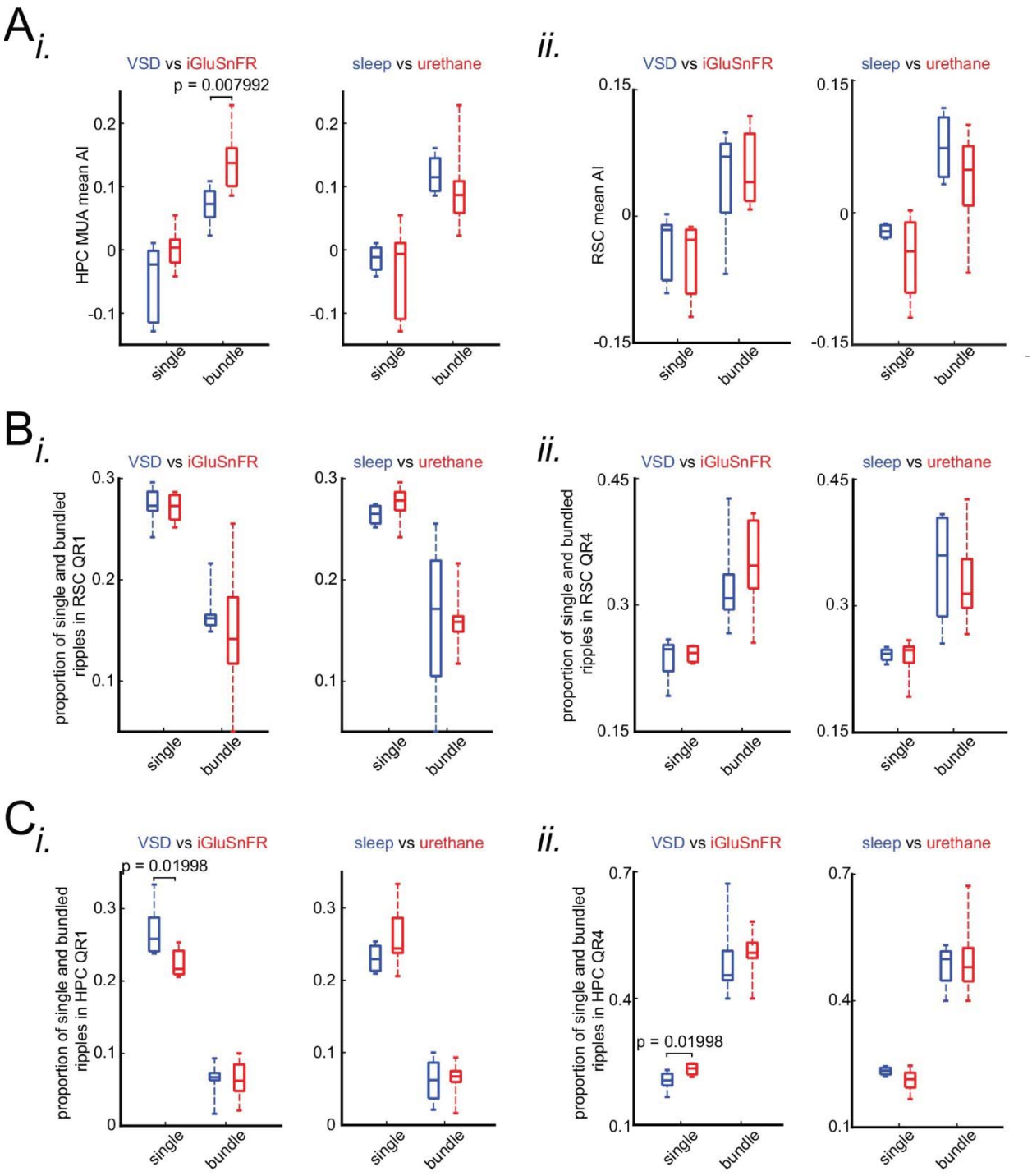

Figure 2.7 – S2. The correlation between occurrence of single/isolated versus bundled ripples and latency of peri-SWR RSC activation is similar under sleep/urethane anesthesia and VSD/iGluSnFR imaging conditions. **(A)** Comparison of HPC MUA (i) and RSC (ii) mean AI values in VSD versus iGluSnFR and in sleep versus urethane conditions across single and bundled ripples. The only statistically significant difference is from comparing HPC MUA mean AI values of bundled ripples in VSD versus iGluSnFR

conditions. **(B)** Comparison of proportion of single and bundled ripples in RSC QR1 (i) and RSC QR4 (ii) in VSD versus iGluSnFR and sleep versus urethane conditions. There is no statistically significant in all eight comparisons here. **(C)** The same as B except for HPC QR1 (i) and HPC QR4 (ii). There are two statistically significant differences out of eight comparisons here. P-values for these significant differences are shown in the diagrams.

2.4. Discussion

The interactions between neocortex and hippocampus play an integral role in memory consolidation during sleep. These interactions are particularly clear during SWRs, where replays of both hippocampal and neocortical memory-associated traces tend to co-occur(Jadhav et al., 2016; Ji and Wilson, 2007; Peyrache et al., 2009). Therefore, it is important to have a functional map of peri-SWR neocortical activity during sleep, which could inform our search for neocortical regions engaged in memory consolidation. In this study, we partly filled this gap by providing a mesoscale spatiotemporal map of peri-SWR dorsal neocortical activity.

2.4.1. Patterns of activity in neocortical regions are differentially modulated around hippocampal SWRs

A differential level of activation and deactivation around SWRs was observed across neocortical regions. This differential modulation was correlated with neocortical structural connectivity: regions with strong axonal interconnections were co-modulated to a similar extent around SWRs. Although significant peri-SWR modulation of discrete neocortical regions has been reported previously using electrophysiological methods, for example, in prefrontal(Battaglia et al., 2004; Mölle et al., 2006; Peyrache et al., 2011, 2009), posterior parietal(Wilber et al., 2017), entorhinal(Isomura et al., 2006), primary somatosensory(Sirota et al., 2003), visual(Ji and Wilson, 2007), and auditory corticex (Rothschild et al., 2017), previous studies were unable to simultaneously characterize the differential patterns of activity across such regions, due to a lack

of extensive spatial coverage of the neocortical mantle. Battaglia et al.(Battaglia et al., 2004) however, have mentioned a midline bias in the modulation of firing rate of different neocortical regions around SWRs, but they left the detailed analysis of such regional effect for future studies. Here, we expanded upon their finding by utilizing high spatiotemporal resolution wide-field optical imaging of voltage and glutamate activity combined with electrophysiology.

The only study to our knowledge that has compared the modulation of neocortical regions around SWRs (Logothetis et al., 2012) reported a significant up-regulation of Blood Oxygen Level-Dependent (BOLD) signal in almost the entire neocortex around SWRs in monkeys, whereas we observed a dichotomy among neocortical regions where somatosensory regions did not show a significant modulation compared to medial subnetwork regions. The previous study also reported a down-regulation of mean peri-SWR BOLD signal in primary visual cortex(Logothetis et al., 2012), which is in contrast to our results in which V1, along with other visual regions, showed strong activations. These discrepancies could be due to an intrinsic difference between BOLD and optical voltage-sensitive dye (VSD) and iGluSnFR imaging signals. As opposed to optical VSD and iGluSnFR signals, BOLD signal is an indirect, and substantially slower measure of neuronal electrical activity, which sometimes may not faithfully reflect the underlying neuronal activity(Iadecola and Nedergaard, 2007). On the other hand, mesoscale optical imaging detects activity predominantly in the superficial ~300 microns of neocortex, although this layer does contain dendrites from lower layers. Additionally, this discrepancy could be due to the difference in animal model (macaque vs mouse), although this seems relatively less likely given the increasingly documented connectivity similarities between these species.

The subnetworks that were accessible to us for imaging are subsets of larger brain-wide networks. In particular, a medial subnetwork, consisting of retrosplenial and posterior parietal cortices, is a subset of the default mode network which is involved in several cognitive processes including memory(Smith et al., 2018; Stafford et al., 2014). Therefore, our results suggest that default mode network is probably one of the most modulated networks of the mouse brain around SWRs. This idea has been supported in macaques(Kaplan et al., 2016).

The reported gradation in modulation extent of different neocortical regions begs the question of what is special about visual sensory areas, which were the second most modulated regions around SWRs, compared with somatosensory areas, which were the least modulated regions. The answer to this question could be related to the stronger structural connectivity between retrosplenial and visual areas compared with retrosplenial and somatosensory cortices(Sugar et al., 2011; Van Groen and Wyss, 2003). However, it does not completely settle the problem. Assuming that neocortical activation around SWRs has a mnemonic function, one may plausibly expect a stronger activation in neocortical regions that are more involved in daily life information processing. For example, vibrissal sensation is highly active during wakefulness and probably plays an important role in memory processes in the rodent brain. But, why is it the case that barrel cortex is not as active as visual cortices around SWRs? It is an interesting question that can be addressed in a separate study with using appropriate behavioral tasks. For instance, the peri-SWR differential activation of neocortical regions after performing odor-memory and visually-guided spatial memory tasks could be compared.

2.4.2. Ripple power is distinctively correlated with peak activity in different neocortical subnetworks

There was a differential association between peak activity in different neocortical regions/subnetworks and hippocampal ripple power. A similar pattern as the one observed earlier in peri-SWR averaging analysis also appeared here, where there was a significantly stronger association between hippocampal ripple power and peak activity in medial compared to somatomotor subnetworks. Molle et al(Mölle et al., 2006) reported a relevant finding, that the probability of ripple occurrence was locked to mPFC EEG positive peak (depth LFP negative peak; equivalent to activation in this paper). They observed the lowest followed by the highest SWR occurrence probabilities well before and very close to the EEG positive peak, respectively.

We also know from other works that there is a significant association between neocortical up-/down-states and SWR occurrence(Battaglia et al., 2004; Isomura et al., 2006; Mölle et al., 2006; Peyrache et al., 2011, 2009; Sirota et al., 2003), although many up-states are not associated with SWRs. Consistent with previous reports, we also found a strong modulation of hippocampal ripple power around the onset of neocortical up-/down-states. Moreover, we extended the previous findings by providing the spatial distribution of correspondence between neocortical up-states and hippocampal ripple power.

2.4.3. Neocortex tends to activate sequentially from medial to more lateral regions around SWRs

There was a medial to lateral temporal gradient of activation of neocortical regions around SWRs on a time scale of about 30 ms. To the best of our knowledge, such mediolateral sequential

activation of neocortical regions around SWRs has not been previously reported, probably because older studies used electrophysiological techniques with sparser spatial coverage. However, Logothetis et al.(Logothetis et al., 2012), in their pioneering study in monkeys, reported a sequential activation among neocortical regions on a time scale of a few seconds using fMRI, where temporal, frontal and prefrontal regions activated earlier than sensory areas around SWRs. In our imaging window, we did not have access to the prefrontal and temporal areas especially medial prefrontal cortex, medial and lateral entorhinal cortices whose activities modulation around SWRs has already been studied (Isomura et al., 2006). Nonetheless, we did observe that visual and auditory sensory cortices were the latest among neocortical regions to activate.

Two major opposite directions of propagation for neocortical waves of activity during slow-wave sleep (SWS) in mice have been reported, posterior-medial to anterior-lateral and anterior-lateral to posterior-medial directions (Greenberg et al., 2018; Mohajerani et al., 2013, 2010). Moreover, retrosplenial cortex has been shown to have the highest probability to be the initial zone of waves with the former direction(Greenberg et al., 2018). Therefore, our results suggest that SWRs tend to occur during slow waves with the posterior-medial to anterior-lateral direction of propagation. It is probable that the neocortical up-states occurring in the absence of SWRs tend to have the opposite direction of propagation as reported in human studies (Massimini et al., 2004), but we did not investigate this idea in the present work.

In addition, compatible with previous reports, our data shows that almost all neocortical regions tend to start activating more or less before the hippocampus generates a SWR (**Figure 2.4Aii**), which suggests a neocortex-to-hippocampus initial direction of information flow around

SWRs. It could be interpreted from the viewpoint of hippocampal memory indexing theory in this way: an initial flow of incompletely retrieved memories from neocortex to hippocampus could lead to reactivation of a corresponding memory index code, stored in hippocampus, which in turn may lead to reactivation of global neocortical memory traces. The potential biasing of hippocampal reactivation by neocortical one has been previously proposed (Helfrich et al., 2019; Klinzing et al., 2019; Ngo et al., 2019; Norman et al., 2019; Rothschild, 2019; Rothschild et al., 2017; Sirota et al., 2003; Wang and Ikemoto, 2016). Therefore, RSC, which is the first among dorsal neocortical regions to activate around SWRs, may mediate this initial information flow, probably through entorhinal cortex, and subsequently bridge the broadcast of hippocampal index code to the rest of the neocortical mantle. In fact, the pattern of structural connectivity of RSC with entorhinal cortex and hippocampus(Wyass and Van Groen, 1992) supports this idea, where numerous efferents from RSC to entorhinal cortex, the principal input zone to hippocampus, and ample afferents from subicular structure, the main output gate in hippocampus, to RSC have been reported(Amaral and Witter, 1989).

The neocortical-hippocampal-neocortical loop of information flow has been observed around hippocampal SWRs after an extensive training in spatial tasks (Rothschild, 2019; Rothschild et al., 2017). One way of detecting such a potential loop in our data was to check if the neocortical activations that precede SWRs (RSC QR1 in **Figure 5Bii**) also lead to delayed neocortical activations. We tested this idea and did not observe a delayed neocortical activation (**Figure 5 – S 3**). However, it does not mean the peri-SWR neocortical-hippocampal-neocortical loop of information flow does not exists. The lack of neocortical-hippocampal-neocortical loop in our data could be explained by the extent of animal experience prior to data collection. Rothschild

et al. (Rothschild et al., 2017) trained rats for at least 12 days in a spatial task, while the mice used in our experiment were naïve. Although unlikely, the lower temporal resolution of glutamate and voltage imaging, compared with that of single-unit activity presented in Rothschild et al. may also explain why we did not observe a neocortical-hippocampal-neocortical loop in our data.

2.4.4. Skewness of peri-SWR hippocampal MUA informs neocortical activation latency relative to SWRs

Two general patterns of hippocampal MUA around SWRs were observed, a gradual build-up leading to a sharp transient increase at the SWR time and a sharp transient increase at the SWR time followed by a gradual decrease to baseline (**Figure 2.5Bii-v**). Interestingly, these two leading and lagging patterns of hippocampal MUA corresponded to two leading and lagging patterns of activity in the neocortex, respectively.

Ji and Wilson(Ji and Wilson, 2007) reported periods of sustained MUA interleaved by periods of silence in both neocortex and hippocampus during SWS, which could be a reflection of slow oscillations. They called these periods of sustained activity “frames”. They found that neocortical and hippocampal frames tend to co-occur and neocortical frames, on average, tend to precede hippocampal ones by ~50 ms. They also reported that there is a higher ripple power right after the onset and right before the offset of the hippocampal frames compared to other times. Moreover, ripple power was higher at the end compared to the beginning of hippocampal frames. Taking into account the co-occurrence of neocortical and hippocampal frames, we can infer that ripple power is probably higher at the end compared to the beginning of neocortical frames as well, potentially denoting a higher probability of ripple occurrence at the end of neocortical up-states.

This inference is compatible with our results, reported in **Figure 2.3 – S2**, where we observed an elevation of hippocampal ripple power right before the onset of RSC down-states.

We speculate that the observed temporal diversity in hippocampal-neocortical interactions around SWRs could reflect the degree of consolidation of a given memory, where neocortex leads hippocampus for well-consolidated memories and lags for newly formed ones. Our prediction is that reactivation of recently formed memory traces tend to happen during SWRs around which neocortex follows hippocampus. Since the timing of neocortical peak activity can be inferred from hippocampal MUA skewness, it is not necessary to directly record neocortical activity to test this hypothesis. Datasets with only hippocampal recordings could be assessed for this purpose.

We should emphasize that the propagating nature of SWRs (Patel et al., 2013) does not influence the results reported in the current study. The majority of SWRs propagate less than 3 mm across the septal-intermediate or intermediate-temporal portion of the rat hippocampus with a minimum speed of 0.33 mm/ms_(Patel et al., 2013). Considering the lengths of mouse hippocampus septal-intermediate and intermediate-temporal portions (~3.25mm) (Milior et al., 2016), it would take less than 9 ms (equivalent to one cycle of ripples) for SWRs to reach to the electrode tip from their initiation zones. Therefore, changing the location of the electrode tip in the septal-intermediate portion of the hippocampus would have a minimal effect on the results reported in this study. However, our findings could have been different had we recorded from the intermediate-temporal portion of HPC since SWRs in dorsal and ventral portions of the hippocampus often do not co-occur (Patel et al., 2013).

2.4.5. Occurrence of single/isolated versus bundled ripples correlates with whether RSC activation precedes or follows hippocampus

Consistent with previous findings(Davidson et al., 2009b; Wu and Foster, 2014), we observed that multiple SWRs could sometimes occur in close proximity as a bundle of ripples. We found that, on average, the neocortical tendency to follow hippocampus is higher around bundled compared to isolated ripples. We also observed that all neocortical subnetworks except the medial one were activated more strongly around bundled compared to isolated ripples.

It has been reported that reactivation of prolonged sequences of place cells, encoding recently traversed long routes by rats, tends to occur during bundled ripples(Davidson et al., 2009b; Wu and Foster, 2014). An isolated ripple has a limited duration and therefore its neural content consists of a sequence of limited number of place cells with place fields covering routes with a limited length(Davidson et al., 2009b). Therefore, if coordinated interaction between hippocampus and neocortex is essential for memory consolidation, it is expected that neocortex stays active longer during bundled ripples, when the hippocampus is reactivating memories of larger content and/or longer duration. This is what was observed, suggesting bundled ripples tend to occur during longer neocortical up-states when there is a longer temporal window available for a potential hippocampal-neocortical communication. Interestingly, according to our data, the probability of occurrence of a bundled ripple in hippocampus is correlated with the pre-SWR (not peri-SWR) deactivation amplitude in neocortex. This dip could be a signaling mechanism for an upcoming longer communication between the two structures.

In conclusion, this work sheds light on the dynamics of hippocampal-neocortical interactions around SWRs which are thought to underlie system memory consolidation processes. Our results reveal neocortical hotspots mediating the broadcast of hippocampal representations to the rest of neocortex by identifying retrosplenial cortex as a potential bridge between these two structures. Past the RSC, information flow tends to be carried along a medial-lateral direction, demonstrating the order of recruitment of different neocortical modules, potentially associated with different features of given memory, around SWRs. Lastly, neocortical activation latency around SWRs is informed by hippocampal features including MUA latency as well as the number of ripple events. The observed spectrum of temporal latencies in activation of hippocampus and neocortex around SWRs possibly reflects the direction of communication during hippocampal and neocortical reactivations of recent versus remote memories. We predict that encoding of new hippocampal-dependent memories lead to a transient bias toward hippocampus leading neocortex around post-encoding sleep SWRs and that this bias would last until the load of consolidating new information gradually dissipates.

2.5. Materials and Methods

2.5.1. Animals

A total of twelve mice, female and male, were used for the imaging studies. For natural sleep experiments, four adult (>2 months) iGluSnFR transgenic mice (strain Emx-CaMKII-Ai85), expressing iGluSnFR in glutamatergic neocortical neurons (Marvin et al., 2013b; Xie et al., 2016b), were used. We generated Emx-CaMKII-Ai85 transgenic mice by crossing the homozygous B6.129S2-Emx1tm1(cre)Krj/J strain (Jax no. 005628) and the B6.Cg-Tg(CamK2a-tTA)1Mmay/DboJ strain (Jax no.007004) with the hemizygous B6;129S-Igs7 tm85(teto-

gltI/GDP*)Hze/J strain (Jax no.026260). This crossing is expected to produce expression of iGluSnFR within all excitatory neurons across all layers of the cortex, but not in GABAergic neurons (Huang and Zeng, 2013; Madisen et al., 2015). Brain sections of the positive transgenic mice confirmed robust expression in the neocortex and hippocampus (**Figure 2.1 – S1**). At the end of natural sleep experiments, two of the iGluSnFR mice were anesthetized with urethane and imaged. Eight C57BL/6J mice from Jackson Laboratory were also used for acute voltage-sensitive dye imaging under urethane anesthesia. An additional set of 6 C57BL/6J mice, including both males and females were used for the electrophysiological studies. Mice were housed in groups of two to five under a 12-h light-dark cycle. Mice were given ad libitum access to water and standard laboratory mouse diet at all times. Mice used in the sleep recording experiments were housed singly after head-plate/electrode implantation surgery. The animal protocols were approved by the University of Lethbridge Animal Care Committee and were in accordance with guidelines set forth by the Canadian Council for Animal Care.

2.5.2. Surgery

Urethane Surgeries

Animals were administered with urethane (1.25 mg/kg) and immediately anesthetized with isoflurane (1–2% mixed in O_2) in order to perform the surgery. We began to administer urethane before the isoflurane, so that by the time we reached the recording stage, urethane would be in effect. This order of administration improved surgery success and reduced fatality rate. We were gradually reducing isoflurane levels over the course of surgery, and isoflurane levels diminished completely by the time urethane recordings began. After animals were anesthetized with isoflurane, mice were placed on a metal plate that could be mounted onto the stage of the upright

macroscope, and the skull was fastened to a steel plate. Before craniotomy, the electrode was implanted in the pyramidal layer of dorsal hippocampus. A 7 × 6 mm unilateral craniotomy (bregma 2.5 to −4.5 mm, lateral 0 to 6 mm) was made, and the underlying dura was removed, as described previously. Body temperature was maintained at 37 °C using a heating pad with a feedback thermistor during the surgery and recording sessions. Animals were also given a tracheotomy to reduce breathing complications.

Head-fixed Natural Sleep Surgeries

For natural sleep experiments, we performed subcutaneous injections with 0.5 gr/Kg buprenorphine half an hour before the surgery started. Animals were then anesthetized with isoflurane (1–2% mixed in O_2). Following anesthesia, we performed the following: removed the head skin, implanted the hippocampal LFP electrode, implanted a head-plate, covered the skull with a thin and transparent layer of the metabond (Parkell, Inc.), and at the end covered the skull with a glass coverslip. An additional bipolar electrode was also implanted in the neck muscles for recording EMG activity. Animals were allowed to recover for two weeks before recordings started.

Surgeries for Unrestrained Natural Sleep Experiments

The animals were anesthetized with isoflurane (2.5% induction, 1-1.5% maintenance), and after removing the skin, multiple holes with particular coordinates were drilled on the skull for implanting hippocampal and neocortical electrodes. An additional bipolar electrode was also implanted in the neck muscles for recording EMG activity. For neocortical and hippocampal recordings of LFPs, bipolar (tip separation = 0.6 mm) and monopolar electrodes, made from Teflon-coated stainless-steel wire with bare diameter of 50.8 μm (A-M Systems), were implanted

in several neocortical areas as well as the pyramidal layer of CA1 in dorsal hippocampus according to the following coordinates in mm: primary motor cortex (M1): AP: 1.5, ML: -1.7, DV: 1.5, secondary motor cortex (M2): AP: 1.7, ML: 0.6, DV:1.1 mm, mouth primary somatosensory area (S1M): AP: 0.85, ML: 2.8, DV: 1.4, barrel primary somatosensory area (S1BC): AP: -0.1, ML: -3.0, DV: 1.4 mm, retrosplenial cortex (RSC): AP: -2.5, ML: 0.6, DV: 1.1 mm, and CA1 subfield of hippocampus (HPC): AP: -2.5, ML: 2.0, DV:1.1 mm. For EMG, a multi-stranded Teflon-coated stainless-steel wire with bare diameter of 127 μm (Cooner Wire) was implanted into the neck musculature using a 22 gauge needle. The reference and ground screws were placed on the skull over the cerebellum. The other end of all electrode wires were clamped between two receptacle connectors (Mill-Max Mfg. Corp.). Clamped connectors were fixated on the skull using metabond (Parkell, Inc.) and dental cement. Body temperature was maintained at 37 °C using a heating pad with a feedback thermistor during the surgery. Animals were allowed to recover for one week before recordings started.

2.5.3. Habituation for head-restraint natural sleep experiments

After 14 d of recovery, mice were habituated to the recording setup, by putting the animals one by one on the recording platform with one or two pieces of Cheerios cereal. They were allowed to explore the platform and acclimatize to the environment. They gradually started to eat the cheerios after a few days. Then the animals were head-restrained with daily prolongation of head-fixation duration. We started with five minutes on the first day and increased the head-restrained duration by five minutes per day for up to one hour. During head-fixation period, each animal was loosely surrounded by a plastic tube to limit motion and guide relaxation. A day before recording, the animals were moved from their home cage colony room to another room at noontime. We

prevented them from falling asleep for around nine hours while they were kept in their own home cage by touching them using a cotton-tip stick whenever they showed signs of falling asleep. In the final hours of sleep restriction, we sometimes gently handled the animals. Then, we transferred the mice to a bigger cage containing new objects, including a running wheel and many pieces of cheerios and a water container. We left the mice in the new cage in the same room overnight. The next day, the mice were transferred to the recording room early in the morning and the recording initiated at around 6:00 AM. After the recording, mice were allowed to recover and sleep at will, in their own home cage in the colony room, for at least three days before repeating this procedure for subsequent recording sessions.

The main reason for not conducting all the experiments under natural sleep was the low success rate of having animals sleeping under head fixation, especially with a slightly tilted head position. Tilting the head was done to include temporal cortices (e.g. the auditory cortex) within our imaging window. Therefore, we used a model of sleep, i.e. urethane anesthesia, to make our sample size larger.

2.5.4. Neocortical and hippocampal LFP recording in head-restrained imaging experiments

Teflon coated 50 μm stainless steel wires (A-M Systems) were used for the hippocampal and neocortical LFP and MUA recordings. For HPC recordings, we drilled a hole on the right hemisphere skull about 2.6 mm lateral to the midline and tangent to the posterior side of the occipital suture. Then, the tip of the monopolar electrode was gradually lowered through the hole at a 57 degree angle with respect to the vertical axis perpendicular to the surface on which the stereotaxic apparatus was sitting. During lowering, the electrode signal with respect to the reference electrode located on top of the cerebellum, was monitored both visually and audibly.

Lowering the electrode was stopped as soon as a dramatic increase in the MUA was heard and observed near the calculated coordinate (angle = 57 degrees, depth = ~1.75 mm) for the pyramidal layer of dorsal CA1. After identifying the optimum location for the electrode tip, we fixated the electrode on the skull using Krazy Glue and dental cement. For the neocortical LFP and MUA recordings, the tip of the electrodes were placed in the superficial layers of neocortical regions (usually motor cortex) at the edge of the cranial window. The electrode signals were amplified (x 1,000) and filtered (0.1–10000 Hz) using a Grass A.C. pre-amplifier Model P511 (Artisan Technology Group ®, IL) and digitized using a Digidata 1440 (Molecular Device Inc., CA) data acquisition system at 20 kHz sampling rate. For the chronic natural sleep experiments, we used the same wire but in the bipolar form to record hippocampal LFP. After data collection, 1 mA positive and negative currents were injected into the hippocampal electrode for about 200 ms to mark electrode location for histology. Animals were perfused with PBS (1x) and PFA (4%) and their brains were extracted, sectioned and mounted. Location of the hippocampal electrode was further confirmed postmortem using cresyl violet staining (**Figure 1 – S 1**).

2.5.5. Neocortical and hippocampal LFP recording in unrestrained sleep experiments

Animals were left undisturbed to recover for 7 days after surgery and then habituated for 5-7 days in the recording chamber. On recording days, animals were transferred to the recording chamber where their sleep activity was recorded starting from 8:30 AM for 4 hours using a motorized commutator (NeuroTek Innovative Technology Inc., On, Canada). LFPs and EMG activity were amplified, filtered (0.1-4000 Hz) and digitized at 16 kHz using a Digital Lynx SX Electrophysiology System (Neuralynx Inc., MT) and the data was recorded and stored on a local PC using Cheetah software (Neuralynx, Inc. MT).

2.5.6. Voltage sensitive dye imaging

The procedures we used are described previously (Greenberg et al., 2018; Mohajerani et al., 2013), and are briefly explained here. After completion of surgery, the exposed brain were incubated with solution containing voltage dye for 30-45 minutes. The solution was made by dissolving voltage-sensitive dye (VSD) RH-1691 (Optical Imaging, New York, NY) in 4-(2-hydroxyethyl)-1-piperazineethanesulfonic acid (HEPES)-buffered saline solution (0.5 mg ml^{-1}). To minimize the movement artifacts due to the respiration, we covered the stained brain with 1.5% agarose made in HEPES-buffered saline and sealed the cranial window with a glass coverslip. VSD imaging of spontaneous activity in the absence of sensory stimuli began ~30 min after removing the dye solution and washing the brain until the residual dye solution was completely removed. Using a charge-coupled device (CCD) camera (1M60 Pantera, Dalsa, Waterloo, ON) and an EPIX E4DB frame grabber with XCAP 3.7 imaging software (EPIX, Inc., Buffalo Grove, IL), we recorded 12-bit images every 10 ms (100 Hz). We used a red LED (Luxeon K2, 627-nm center) and excitation filters of 630 ± 15 nm to excite the VSD. The reflected fluorescent signal from excited dyes was filtered using a 673 to 703 nm bandpass optical filter (Semrock, New York, NY), and was passed through a microscope composed of front-to-front video lenses (8.6 × 8.6 mm field of view, 67 μm per pixel). To reduce the potential artifacts caused by the presence of large neocortical blood vessels, we focused the lens into the neocortex to a depth of ~1 mm. Total duration of the VSD excitation in a typical imaging experiment ranged from one to two hours. We also recorded the voltage optical signal from the neocortex in response to different periphery stimulation as described before (Mohajerani et al., 2013). Sensory stimulation was used to determine the coordinates for the primary sensory areas (HLS1, FLS1, BCS1, V1 and A1),

secondary somatosensory areas (HLS2, FLS2 and BCS2). From these primary sensory coordinates, the relative locations of additional associational areas were estimated using stereotaxic coordinates (ptA, RS, M2, V2M (medial secondary visual cortex), V2L (lateral secondary visual cortex), and M1 (primary motor cortex).

2.5.7. Glutamate imaging

iGluSnFR was excited with light from a blue-light-emitting diode (Luxeon K2, 473 nm, Quadica Developments Inc., Lethbridge, Alberta) delivered through a band-pass filter (Chroma Technology Corp, 467– 499 nm). Ambient light resulting from iGluSnFR excitation (473 nm) was ~1.5 mW over the 8 × 8 mm area used for imaging. iGluSnFR fluorescence emission was filtered using a 520–580 nm band-pass filter (Semrock, New York, NY). We collected 12-bit images at 100 Hz using CCD camera (1M60 Pantera, Dalsa, Waterloo, ON) and an EPIX E4DB frame grabber with XCAP 3.7 imaging software (EPIX, Inc., Buffalo Grove, IL). To reduce the potential artifacts caused by the presence of large neocortical blood vessels, we focused the lens into the neocortex to a depth of ~1 mm. Total duration of the indicator excitation in a typical imaging experiment ranged from two to three hours. At the last day of experiments, we anesthetized mice with 1.5 gr/kg urethane and imaged the neocortex. We also recorded the iGluSnFR signal in response to different periphery stimulation under urethane anesthesia as described before(Mohajerani et al., 2013). Sensory stimulation were used to functionally map the center of the hind-limb somatosensory, fore-limb somatosensory, auditory, visual, and barrel cortices.

2.5.8. Behavioral and pupil recording

To monitor animal behavior and measure pupil size, we used an IR USB camera (Point Grey Firefly MV USB, FLIR Systems, Inc.) with 20 Hertz frame rate. We also used an infrared LED to illuminate the animals' faces and parts of their body including their head, shoulders, and forelimbs.

2.5.9. Pupil diameter detection

We used an intensity-based thresholding custom made algorithm implemented in Bonsai (https://bonsai-rx.org//) to quantify pupil diameter. Briefly, the algorithm detects the pupil by segmenting it with the surrounding areas of the eye and models it as an ellipse. The main diagonal of the ellipse was considered as the pupil diameter.

2.5.10. Sleep scoring

Vigilance stages of each animal were classified as awake, NREM, and REM by thresholding EMG and hippocampal theta-to-delta ratio signals(Niethard et al., 2018; Yang et al., 2014; Yüzgeç et al., 2018). Awake periods were identified by visual inspection of animal behavior and EMG signal. NREM sleep was identified as periods with low EMG and theta-to-delta ratio. For head-restrained experiments, we also included a third criteria for detecting NREM sleep periods: lack of facial (around the chin) movement for at least 50 seconds. REM sleep periods were detected when EMG signals was the lowest, which is due to muscular atonia, and high theta-to-delta ratios. For head-fixed experiments, we also measured pupil size to verify our sleep scoring results (Yüzgeç et al., 2018).

2.5.10. SWRs detection

We followed the method used in Molle et al.(Mölle et al., 2006) for detecting ripples. Briefly, the raw hippocampal LFP was first down-sampled to 2 kHz. Then, it was filtered using a 400-order band-pass FIR filter designed in MATLAB (MathWorks). The filtered signal was rectified and smoothed using a rectangular window with a length of 8 ms, generating the ripple power signal. SWRs were identified when the ripple power signal passed the detection threshold defined by the mean plus a multiple (**Figure 2.2** and **Figure 2.2 – S3**: 2 for VSDI and 3 for iGluSnFR imaging; **Figure 2.2 – S4**: 3 for VSDI and 4 for iGluSnFR imaging) of standard deviation of the ripple power signals. A lower threshold (75% of the detection threshold) was used to identify the onset and offset of each SWR. Detected events were further screened by applying a duration threshold. Events with a duration shorter than the mean duration of all detected events were excluded. The ripple center was defined as the timestamp of the largest trough between the onset and offset times. Moreover, events with centers less than 50 ms apart were concatenated.

2.5.11. Splitting SWRs into HPC quartiles

We defined a quantity, called asymmetry index (AI), to measure the asymmetry or skewness of hippocampal MUA and neocortical voltage and iGluSnFR signals centered on SWR centers timestamps (0s). AI is defined as (A - B) / (A + B), where A and B are the mean values from -0.2-0 s and 0-0.2 s respectively. AI values range from -1 and 1, where an AI = -1 and AI = 1 denote complete skewness of the signal to left and right relative to the SWR centers, respectively. The distribution of MUA AI values was split into quartiles. The first and fourth quartiles were utilized for further analyses to examine whether SWRs either preceded or followed by MUA, respectively.

2.5.12. Bundled ripples detection

Bundled ripples were identified by applying an additional threshold on previously detected SWRs. For each previously detected SWR, the wavelet-based power (using analytic Morlet wavelet) in the ripple-band frequencies (150-250 Hz) was calculated for peri-SWR hippocampal LFP traces. Ripple events were identified as bundled ripples if the following criteria were met: (1) The power signal surpassed an adaptively determined power threshold for at least two successive times; (2) The minimum duration was met for each supra-threshold event; and (3) The temporal distance between two successive supra-threshold peaks was less than 200 ms(Davidson et al., 2009b; Wu and Foster, 2014). The remainder of detected SWRs were considered as single/isolated events. 62 ± 0.03% (mean + SEM; n = 14 mice) of all detected bundled ripples in our data consist of two ripples.

2.5.13. MUA calculation

MUA signal was calculated from hippocampal and neocortical LFP signals using a similar method reported before(Belitski et al., 2008). Briefly, the LFP signals were filtered above 300 Hz, rectified and smoothed with a rectangular window with the length of ~3 ms for the hippocampal and 100 ms for the neocortical signals. The resultant signals are called HPC and RSC MUA, respectively, in this work.

2.5.14. Detection of neocortical up-/down-states

A thresholding procedure (Battaglia et al., 2004) similar to what used for the SWRs detection was employed to detect the neocortical up-/down states. Briefly, two thresholds for amplitude and duration were applied on the neocortical MUA signal. The events (1) whose amplitudes were greater (smaller) and (2) whose durations were longer than the corresponding thresholds were considered as up-states (down-states). Different thresholds were used for detection of up- and down-states.

2.5.15. Detection of neocortical peak activation measured by optical signal

A very similar approach to what used for the detection of neocortical up-/down-states was employed to detect neocortical peak activations measured by optical signal. Briefly, the voltage or iGluSnFR $\Delta F/F_0$ captured from each neocortical region was thresholded for both amplitude and duration. The events with amplitudes larger and durations longer than the corresponding thresholds were detected as peak activations in that region. Different thresholds were used for different neocortical regions.

2.5.16. Preprocessing of Voltage and iGluSnFR imaging data

The optical voltage and glutamate signals were first denoised by applying singular-value decomposition and taking the components with the greatest associated singular values(Mitra and Pesaran, 1999). Then, for each pixel in the imaging window, a baseline (F_0) of the optical voltage and iGluSnFR signals (F) was calculated. Baseline calculation was accomplished using the *locdetrend* function in the Chronux toolbox (http://chronux.org/; Mitra & Bokil 2007) to fit a

piecewise linear curve to the pixel time series using the local regression method. The calculated baseline signal was then subtracted from the raw signal, and the difference signal was divided by the baseline values at each time point ($\Delta F/F_0$). Because most of the optical signal power is concentrated in lower frequencies(Mohajerani et al., 2013), a band pass (0.1–6 Hz) FIR filter was applied on the $\Delta F/F_0$ signal. In this paper, optical signals were expressed as a percentage change relative to the baseline optical signal responses ($\Delta F/F_0 \times 100\%$).

2.5.17. Optical flow analysis

To estimate the propagation direction of peri-SWR neocortical activity, we randomly selected around twenty peri-SWR stacks of imaging frames, and averaged them. The averaged stack was used to calculate propagation direction of neocortical waves at the time of SWRs. Propagation direction was calculated using the Horn-Schunck method implemented in Matlab-based Optical-Flow Analysis Toolbox developed by Afrashteh et al.(Afrashteh et al., 2017). This toolbox can be used to quantify the spatiotemporal dynamics of mesoscale brain activity such as propagation direction, location of sources and sinks as well as the trajectories and temporal velocities of flow of activity dynamics. To generate a circular distribution of propagation direction, we repeated the above process for 1000 iterations.

2.5.18. z-scoring peri-SWR neocortical activity

The inter-SWR intervals were randomly permuted to generate new timestamps. Then, for each random time point, the surrounding imaging frames, capturing one second before to one second after, were temporally aligned. The mean and standard deviation of the corresponding frames were calculated across all the randomly generated time points. In doing so, we generated a

mean and a standard deviation stack of frames. We used these two stacks to z-score all the individual peri-SWR stacks of neocortical activity.

2.5.19. Statistical tests

All statistical test for linear data were performed using MATLAB built-in functions. One-sided paired t-test and Wilcoxon signed-rank tests were used for linear data. For circular data, Kuiper two-sample test, implemented in CircStat toolbox(Berens, 2009), was used.

2.5.20. Data exclusion criterion

For some group data comparisons in supplementary figures, outlier data points, defined as points outside 95% of the distribution relative to the median value, were excluded in some groups. Whenever the number of animals is less than 14 ($n < 14$), which is the case only in supplementary figures, such exclusion has been performed.

Acknowledgment

This work was supported by Natural Sciences and Engineering Research Council of Canada (grant no 40352 & 1631465 to MHM and BLM respectively), Alberta Innovates (MHM and BLM), Alberta Prion Research Institute (grant no. 43568 to MHM), and Canadian Institute for Health Research (grant no 390930 & 156040 to MHM and BLM MHM respectively), National Science Foundation (MHM, BLM), and USA Defense Advanced Research Projects Agency (grant no HR0011-18-2-0021 to BLM). The authors also thank Di Shao and Behroo Mirza Agha for animal breeding, J. Sun for surgical assistance and Masami Tatsuno for their suggestions for data

analysis. The authors thank Hongkoi Zeng from the Allen Institute for Brain Science for providing the Emx-cre, Camk2a-tTa, and Ai85 mice as a gift.

3. Spatiotemporal patterns of neocortical activity around hippocampal sharp-wave ripples during wakefulness

3.1. Abstract

Coordinated activity in the hippocampal-neocortical network around hippocampal sharp-wave ripples (SWRs) is essential for mnemonic information processing in the brain. Even though SWRs occur in both sleep and wake states, the majority of studies have been focused on studying the dynamics of neocortical activity around sleep SWRs. Given that sleep and awake SWRs likely serve somewhat different functions, and that the neurochemical milieu of the cortex differs substantially across behavioral states, the corresponding neocortical activity patterns may differ in important ways. We addressed this possibility by conducting voltage and glutamate wide-field imaging of a large portion of the dorsal neocortex with concurrent hippocampal LFP recording in awake mice. In contrast to sleep, the peri-SWRs pattern of neocortical voltage activity during wakefulness showed a strong reduction, especially in the agranular retrosplenial cortex (aRSC). To investigate how this pattern is reflected in the neuronal spiking activity, two-photon calcium imaging of aRSC was also conducted. At least two subpopulations of excitatory neurons in aRSC were observed, whose peri-ripple modulation patterns were opposite of each other: one increased and the other decreased firing rate. These differences in peri-SWR spatiotemporal patterns of neocortical activity in sleep versus awake states might reflect different functions, for example, memory consolidation versus planning.

3.2. Introduction

Hippocampal-neocortical interactions around hippocampal SWRs play an important role in memory processes (Buzsáki, 2015, 1989; Yu-Lin Qin et al., 1997; Schwindel and McNaughton, 2011). The functional role of such interactions is believed to be brain state-dependent such that they are involved in memory consolidation during NREM sleep, while they are implicated in memory-guided behavior such as planning and memory retrieval in waking state (Ólafsdóttir et al., 2018; Roumis and Frank, 2015; Tang and Jadhav, 2019). This state-dependent functional dichotomy poses a question: how do spatiotemporal dynamics of hippocampal-neocortical network interactions differ in the two states?

There are pronounced differences in the neocortical activity patterns between NREM sleep and quiet wakefulness. The most prominent difference is the near absence of so-called slow-oscillations (SO) during wakefulness. SO, a quasi-synchronous <= 1 Hz fluctuation observed throughout the neocortex during NREM sleep, is partly correlated with hippocampal SWRs, and recent memory reactivation in the cortex is strongly locked to SWRs (Benchenane et al., 2010; Kaefer et al., 2020; Peyrache et al., 2009; Rothschild et al., 2016). However, given the absence of SO in wakefulness (Tang et al., 2017), it is not straightforward to extrapolate from sleep to wakefulness, although a few studies have shown that the proportion of neurons whose spiking activity is suppressed around hippocampal SWRs is significantly higher in wakefulness compared with sleep.

In the present study, we extended the previous results by imaging the activity of a large portion of the dorsal neocortical regions in awake mice, with concurrent local-field potential (LFP) recording from the pyramidal layer of the dorsal CA1. Wide-field glutamate and voltage recording were used to capture the excitatory synaptic input and the membrane potential fluctuations across

neocortical regions and to correlate them with the occurrence of hippocampal SWRs. A sharp contrast in the peri-SWRs neocortical activity between the awake and sleep states was observed. To further elaborate on this contrast, we used the two-photon calcium imaging to focus on the agranular retrosplenial cortex (aRSC) whose glutamate and voltage activity patterns were different from the rest of the imaged regions. Our results indicate that inhibition plays a stronger role in peri-ripple neocortical activity in awake than sleep states.

3.3. Results

To study peri-ripple activity across neocortical regions in the awake state, we utilized three imaging modalities to shed light on different dimensions of the problem at hand. First, to capture the internal dynamics of neocortical regions, wide-field voltage imaging with voltage indicator (butterfly1.2) expressed in the layer II/III excitatory neocortical neurons was used (Figure 3.1Aii). Second, to capture the excitatory input (from the perspective of the dendritic trees) to the neocortical regions, wide-field imaging with intensity-based glutamate-sensing fluorescent reporter (iGluSnFR) indicator expressed in the layer II/III excitatory neocortical neurons was used (Figure 1Ai). Last, to estimate the spiking output of neocortical neurons, two-photon calcium imaging of the aRSC in Thy1-GCamp mice was conducted (Figure 3.1Aiii). In all these three imaging modality experiments, concurrent local field potential (LFP) recording from the pyramidal layer of the CA1 subfield of the dorsal hippocampus was performed, and the hippocampal LFP was used to detect ripples (Figure 3.1B). To extract the overall neocortical behavior around ripples, the activity, captured by the three modalities, was aligned to the timestamp of the ripple centers (largest trough of ripples) and averaged (Figure 3.1C).

3.3.1. Voltage activity sharply dropped during awake ripples

The peri-ripple average of the voltage signals in the awake state revealed an activity pattern that was in sharp contrast with what had been reported in sleep (Figure 3.2 – S1A-B). The average neocortical voltage activity showed a fast reduction right after the ripple peaks (Figure 3.2A-B). There was significant regional variation in this reduction, with aRSC showing the strongest reduction amplitude (Figure 3.2C). This phenomenon was consistent in all the six animals used

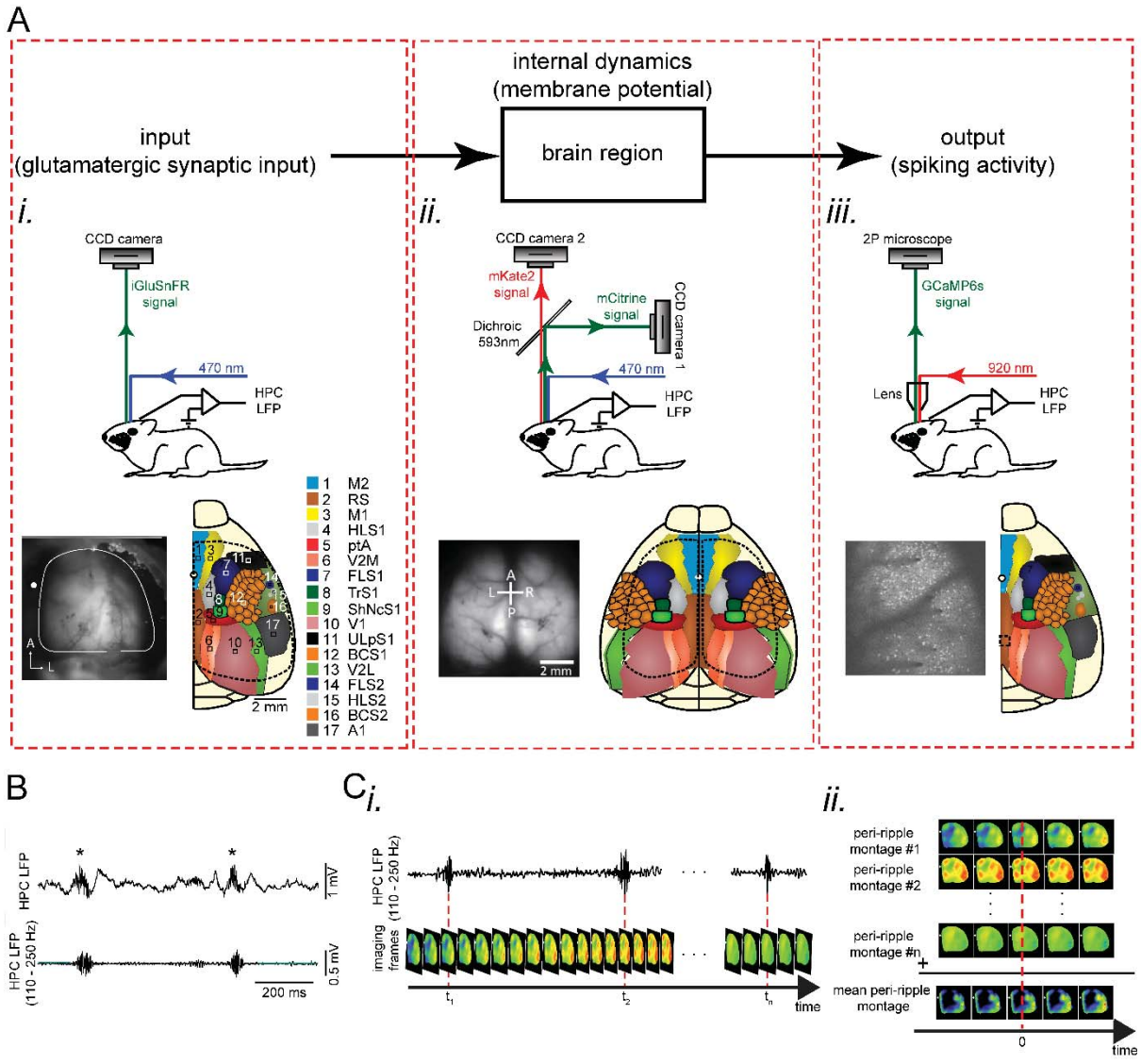

Figure 3.1. Experimental protocol for investigating peri-ripple neocortical activity during the awake state. (A) Top: each region could be modeled as an input-output block with internal dynamics. Bottom (i-iii): experimental setups, exemplar imaging windows, and schematic of regions included in the windows for unilateral wide-field glutamate imaging (i), bilateral wide-field voltage imaging (ii), and two-photon calcium imaging (iii) which were conducted for monitoring input, internal dynamics, and output, respectively. (B) Top: an exemplar local field potential (LFP) trace recorded from the pyramidal layer of CA1 subfield of the dorsal hippocampus. Asterisks denote detected ripples. Bottom: ripple-band (110-250 Hz) filtered version of the top trace. (C) Schematic of peri-ripple (ripple-triggered) averaging analysis. (i) Schematic of concurrently recorded LFP and imaging signals. Red dashed lines indicate the timestamp of the center of detected ripples. (ii) The imaging frames around the timestamp of the detected ripples are aligned with respect to the ripple centers and averaged.

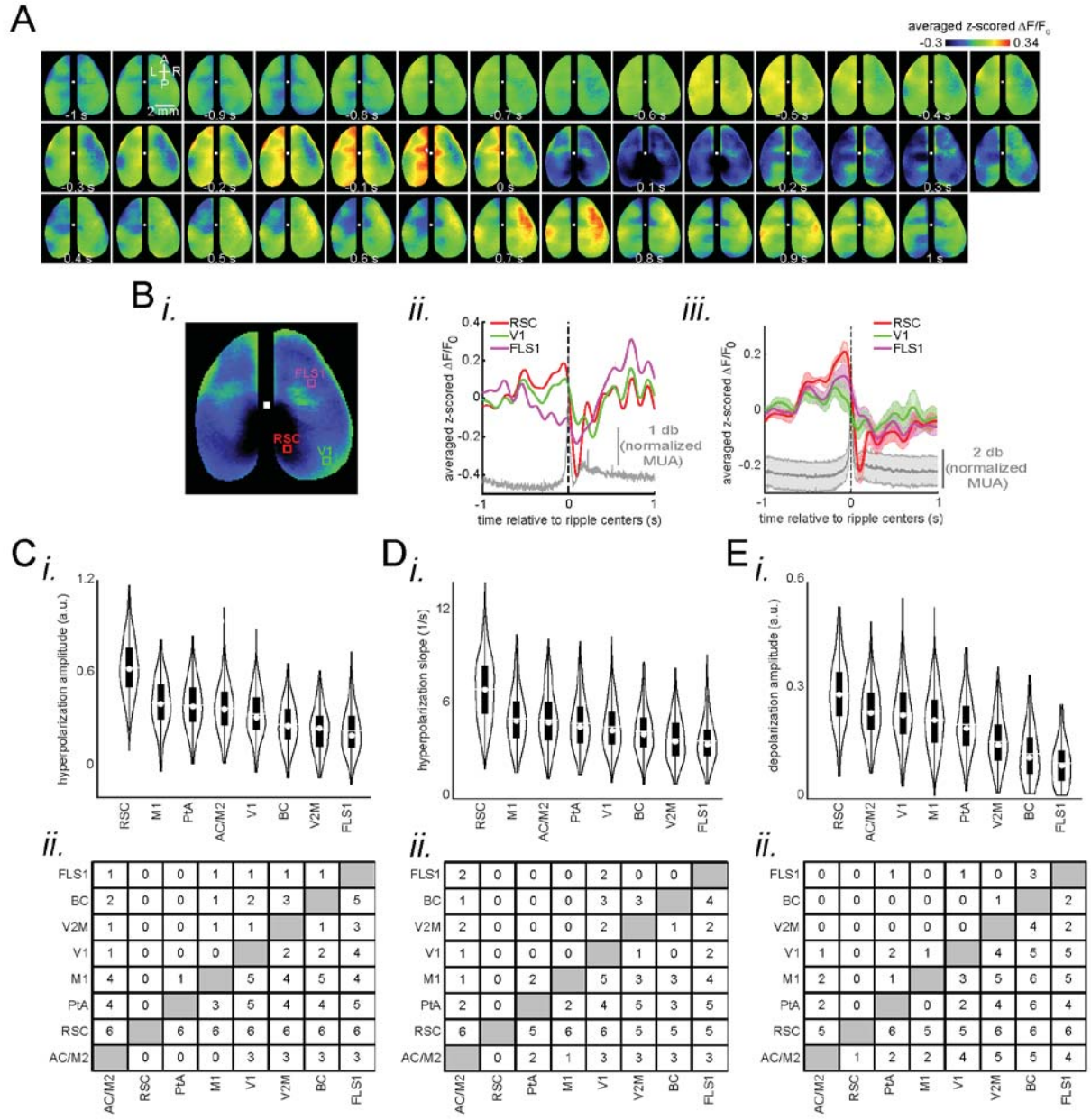

Figure 3.2. Voltage activity sharply dropped during awake ripples. (A) Montage of average voltage activity 1 second before and after ripple centers in a representative animal. Zero time represents the timestamp of the center of ripples. Note the reduction of the voltage signal, i.e. inhibition, across neocortical regions during ripples and the elevation of voltage activity before ripples. The inhibition is strongest in the retrosplenial cortex, the dark area in the posterior-medial part of the imaging window which is noticeable in the frame associated with the time 100 ms. (B) (i-ii) A representative frame chosen from inhibition period in A along with peri-ripple mean voltage time-series of three regions of interests chosen from the retrosplenial cortex (RSC), primary visual cortex (V1), and primary forelimb somatosensory cortex (FLS1). The data represented in time-series format is the same data shown in A. The gray trace is the mean MUA

activity. (iii) peri-ripple mean voltage time-series and MUA (gray) averaged across six mice. The shading represents standard error of the mean (SEM). RSC shows strongest and fastest inhibition compared with other regions. (C) (i) bootstrap distribution of inhibition amplitude (with respect to pre-ripple baseline) across imaged neocortical regions in a representative animal. The regions are sorted according to their distribution mean in descending order (repeated-measure ANOVA, $F = 440.597$, $df = 7$, p-value = 1.0596×10^{-211}, $n = 231$). (ii) The result of posthoc multiple comparisons following repeated-measure ANOVA, pooled across animals (6 animals). The numbers at each entry of the matrix represent the number of mice in which the bootstrap distribution associated with the corresponding row region has statistically significant larger mean than column region. Significance alpha level of 0.05 was used as the threshold for statistical significance. (D-E) The same as C but for inhibition slope (mean over full-width at half-maximum of derivative of the voltage signal; repeated-measure ANOVA, $F = 195.096$, $df = 7$, p-value = 1.1431×10^{-128}, $n = 231$) and pre-ripple elevation amplitude (mean over full-width at half-maximum; repeated-measure ANOVA, $F = 288.5488$, $df = 7$, p-value = 1.8389×10^{-142}, $n = 176$) of the voltage activity. Note that RSC, compared with all other imaged regions, shows largest inhibition amplitude, fastest rate of change of inhibition, and largest pre-ripple depolarization in at least 5 out of 6 animals.

for this set of experiments (Figure 3.2C; Figure 2 – S1C). The rate of reduction of the voltage activity was also fastest in the aRSC in the majority of animals (Figure 3.2D; Figure 3.2 – S1D). Since the rate of change (derivative) of voltage is proportional to the capacitive current, this result suggests that capacitive trans-membrane inhibitory currents are strongest in aRSC compared with other neocortical regions. Moreover, we observed a pre-ripple elevation of voltage activity which was also strongest in aRSC in at least half of the animals (Figure 3.2E; Figure 3.2 – S1E).

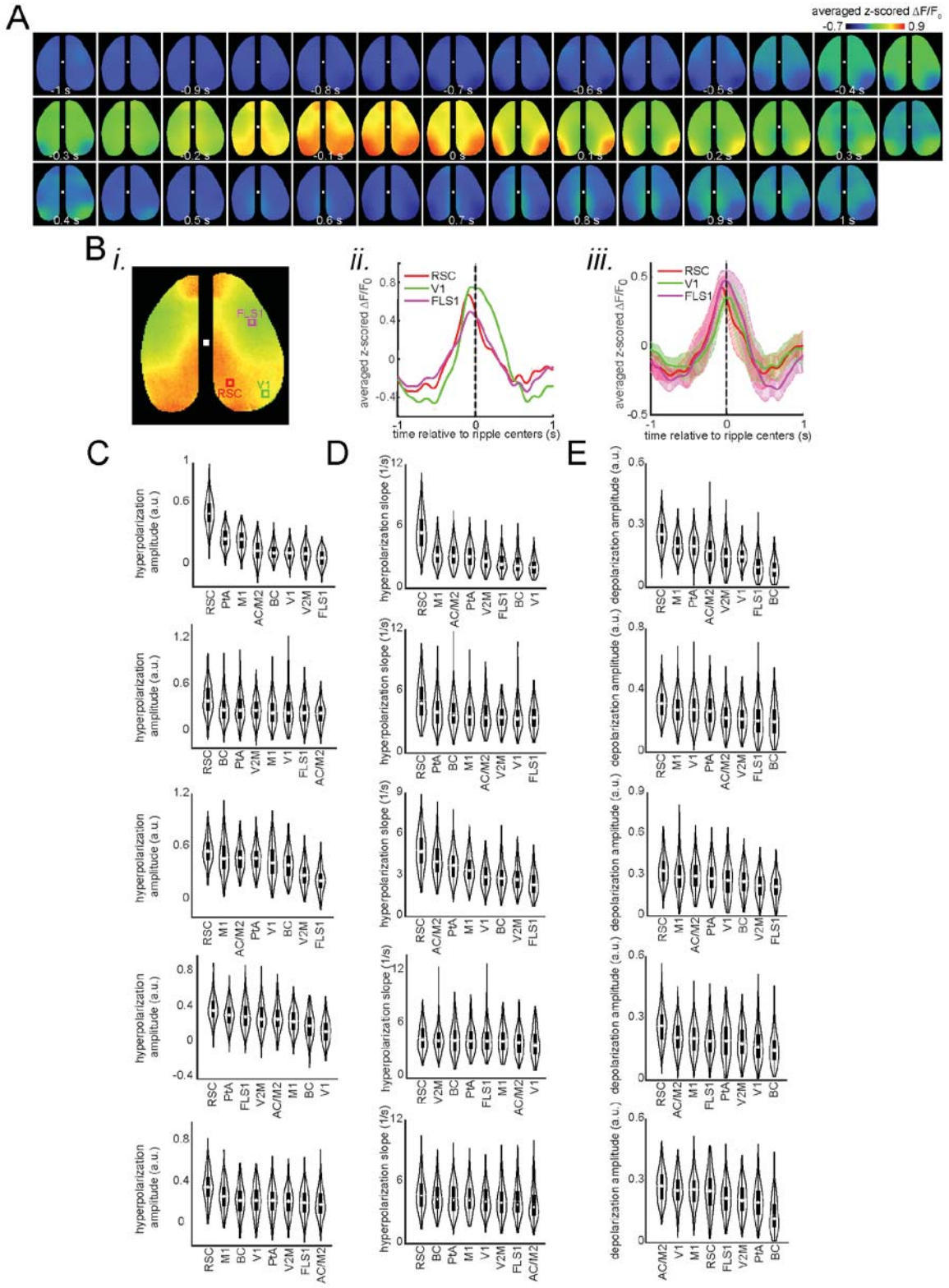
A
averaged z-scored ΔF/F0
-0.7
0.9
-1 s
-0.9 s
-0.8 s
-0.7 s
-0.6 s
-0.5 s
-0.4 s
-0.3 s
-0.2 s
-0.1 s
0 s
0.1 s
0.2 s
0.3 s
0.4 s
0.5 s
0.6 s
0.7 s
0.8 s
0.9 s
1 s
B i.
FLS1
RSC
V1
ii.
RSC
V1
FLS1
averaged z-scored ΔF/F0
time relative to ripple centers (s)
iii.
RSC
V1
FLS1
averaged z-scored ΔF/F0
time relative to ripple centers (s)
C
hyperpolarization amplitude (a.u.)
RSC PtA M1 AC/M2 BC V1 V2M FLS1
RSC BC PtA V2M M1 V1 FLS1 AC/M2
RSC M1 AC/M2 PtA V1 BC V2M FLS1
RSC PtA FLS1 V2M AC/M2 M1 BC V1
RSC M1 BC V1 PtA V2M FLS1 AC/M2
D
hyperpolarization slope (1/s)
RSC M1 AC/M2 PtA V2M FLS1 BC V1
RSC PtA BC M1 AC/M2 V2M V1 FLS1
RSC AC/M2 PtA M1 V1 BC V2M FLS1
RSC V2M BC PtA FLS1 M1 AC/M2 V1
RSC BC PtA M1 V1 V2M FLS1 AC/M2
E
depolarization amplitude (a.u.)
RSC M1 PtA AC/M2 V2M V1 FLS1 BC
RSC M1 V1 PtA AC/M2 V2M FLS1 BC
RSC M1 AC/M2 PtA V1 BC V2M FLS1
RSC AC/M2 M1 FLS1 PtA V2M V1 BC
AC/M2 V1 M1 RSC FLS1 V2M PtA BC

Figure 3.2 - S1. (A) Montage of average voltage activity 1 second before and after ripple centers under urethane anesthesia (as a model of sleep) in the same representative animal as in 2A. Zero time represents the timestamp of center of ripples. Note the elevation of voltage signal (depolarization) across neocortical regions during ripples which is in sharp contrast with the result in 2A. (B) (i-ii) A representative frame chosen from depolarization period in A along with peri-ripple mean voltage time-series of three region of interests chosen from retrosplenial cortex (RSC), primary visual cortex (V1), and primary forelimb somatosensory cortex (FLS1). The data represented in time-series format is the same data shown in A. (iii) peri-ripple mean voltage time-series under urethane anesthesia averaged across five mice. The shading represents standard error of the mean (SEM). (C) The same as Figure 2C-i (top) but for all other individual mice (repeated-measure ANOVA with df = 7 and n = 231; from top to bottom: F = 858.17, p = 0; F = 62.95, $p = 3.0723\times10^{-46}$; F = 202.86, $p = 1.578\times10^{-86}$; F = 163.62, $p = 1.797\times10^{-82}$; F = 115.303, $p = 2.703\times10^{-97}$). (D) The same as Figure 2D-i (top) but for all other individual mice (repeated-measure ANOVA with df = 7 and n = 231; from top to bottom: F = 291.61, $p = 1.32\times10^{-161}$; F = 63.9, $p = 4.56\times10^{-55}$; F = 240.13, $p = 1.36\times10^{-146}$; F = 7.35, $p = 4.06\times10^{-6}$; F = 20.24, $p = 1.43\times10^{-20}$). (E) The same as Figure 2E-i (top) but for all other individual mice (repeated-measure ANOVA with df = 7 and n = 231; from top to bottom: F = 316.86, $p = 1.79\times10^{-213}$; F = 92.71, $p = 4.53\times10^{-74}$; F = 62.03, $p = 4.88\times10^{-37}$; F = 58.77, $p = 2.3\times10^{-50}$; F = 134.77, $p = 2.37\times10^{-123}$).

3.3.2. Glutamatergic activity is reduced before and elevated after awake ripples in the neocortical superficial layers

Next, we performed peri-ripple averaging of glutamate (iGluSnFR) activity over the dorsal neocortex. In all the imaged neocortical regions, the glutamate signal was reduced before the ripple peak (Figure 3.3A-B). This reduction is probably associated with a brain state (i.e. quiet wakefulness) which is conducive for the emergence of the ripples. On the other hand, after the ripples occurred, the glutamate signal significantly increased (Figure 3.3A-B). There was a region-effect in the amplitude of the signal where the regions barrel cortex (BC), primary auditory cortex (Aud), and secondary medial visual cortex (V2M) showed the highest and aRSC the lowest increase in the majority of the animals (Figure 3.3C; Figure 3.3 – S1A). There was also a region-effect in the rate of change (i.e. slope or derivative) and elevation onset of the glutamate activity where aRSC showed the steepest slope and the latest onset of increment compared with other imaged regions, especially with BC, Aud, and V2M which showed the lowest slope (Figure 3.3D;

Figure 3.3 – S1B) and the earliest onset time in the majority of the animals (Figure 3.3E; Figure 3.3 – S1C). This result shows that even though aRSC glutamate signal starts activating late, it catches up by raising faster.

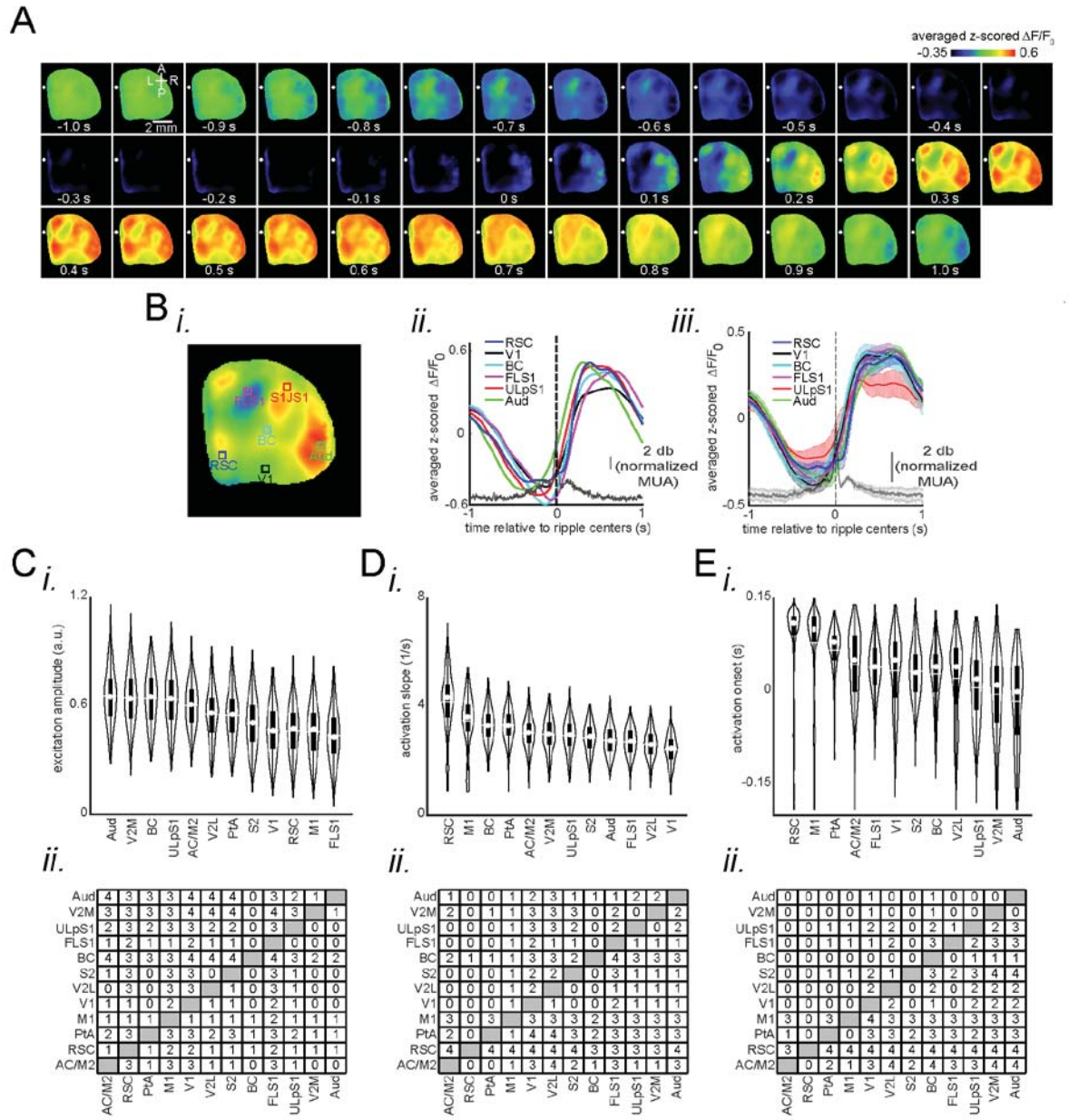

Figure 3.3. Glutamatergic excitation is reduced before and is elevated after awake ripples. (A) Montage of average iGluSnFR activity 1 second before and after ripple centers in a representative Ras iGluSnFR animal. Zero time represents the timestamp of the center of ripples. Note the elevation of the iGluSnFR signal, i.e. excitation, across neocortical regions after ripples. (B) (i-ii) A representative frame chosen from excitation period in A along with peri-ripple mean iGluSnFR time-series of six regions of interest chosen from retrosplenial cortex (RSC), primary visual cortex (V1), and primary forelimb somatosensory cortex

(FLS1), primary lip somatosensory cortex (ULpS1), primary barrel cortex (BC), and primary auditory cortex (Aud). The data represented in time-series format is the same data shown in A. The black/gray trace is the mean normalized MUA activity. (iii) peri-ripple mean iGluSnFR time-series and mean normalized MUA activity (black/gray) averaged across 4 mice. The shading represents the standard error of the mean (SEM). The glutamate signal from RSC shows the fastest and latest onset of elevation. (C) (i) bootstrap distribution of excitation amplitude (with respect to the pre-ripple baseline) across imaged neocortical regions in a representative animal. The regions are sorted according to their distribution mean in descending order (repeated-measure ANOVA, F = 337.9781, df = 11, p-value = 3.6841×10^{-262}, n = 270). (ii) The result of posthoc multiple comparisons following repeated measure ANOVA, pooled across animals (4 animals). The numbers at each entry of the matrix represent the number of mice in which the bootstrap distribution associated with the corresponding row region has a statistically significant larger mean than the column region. The significance alpha level of 0.05 was used as the threshold for statistical significance. (D-E) The same as C but for excitation slope (mean over full-width at half-maximum of derivative of the voltage signal repeated-measure ANOVA, F = 207.5245, df = 11, p-value = 3.427×10^{-130}, n = 270) and excitation onset (timestamp at which the derivative of iGluSnFR signal reaches its half-maximum for the first time repeated-measure ANOVA, F = 113.0048, df = 11, p-value = 7.705×10^{-149}, n = 270) of the glutamate activity. Note that RSC, compared with all other imaged regions, shows the fastest rate of change and the latest onset of excitation in at least 3 out of 4 animals.

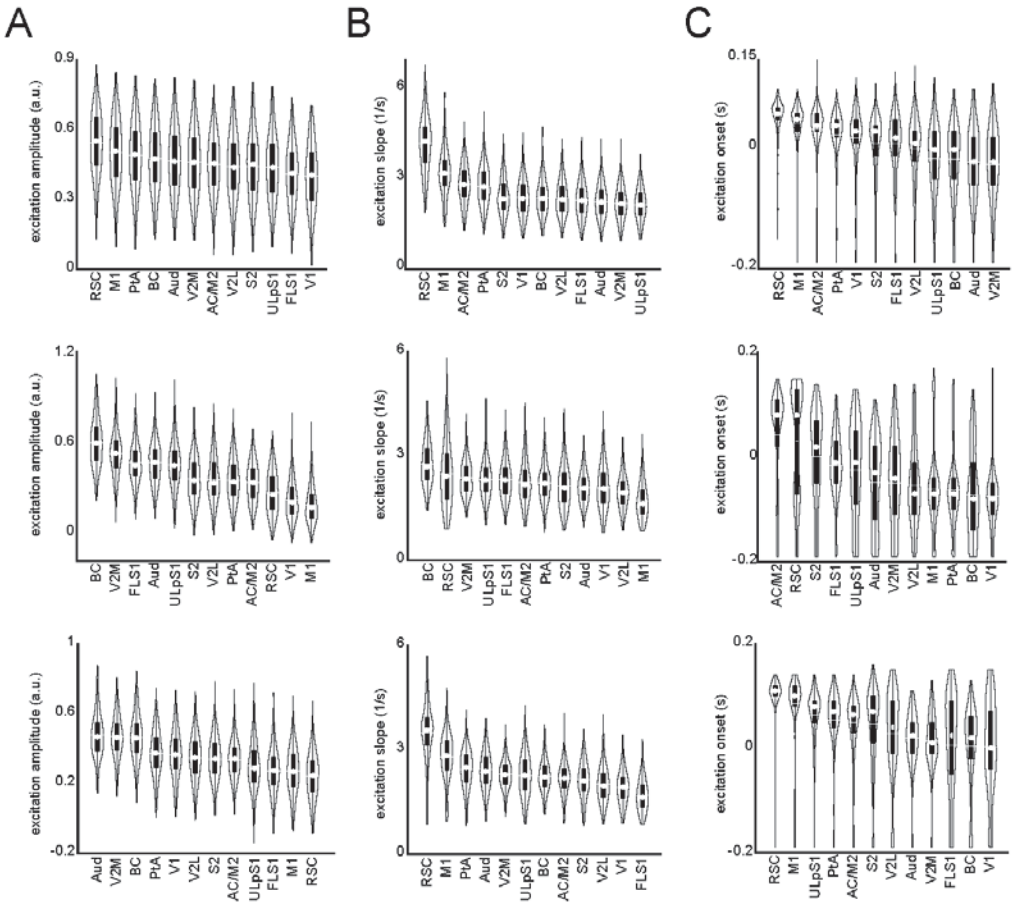

Figure 3.3 – S1. (A) The same as Figure 3C-i (top) but for all other individual mice (repeated-measure ANOVA with df = 11 and n = 270; from top to bottom: F = 304.206, p = 1.3×10^{-211}; F = 663.42, p = 0; F = 394.13, p = 4.42×10^{-256}). (B) The same as Figure 3D-i (top) but for all other individual mice (repeated-measure ANOVA with df = 11 and n = 270; from top to bottom: F = 889.69, p = 0; F = 81.93, p = 2.83×10^{-76}; F = 249.77, p = 1.35×10^{-180}). (C) The same as Figure 3E-i (top) but for all other individual mice (repeated-measure ANOVA with df = 11 and n = 270; from top to bottom: F = 142.93, p = 3.53×10^{-187}; F = 86.56, p = 2.53×10^{-119}; F = 57.1, p = 5.78×10^{-80}).

3.3.3. A subpopulation of aRSC neurons fires during ripples despite the presence of strong voltage reduction

Due to the suppression of membrane potential in superficial layers of aRSC neurons and a delayed glutamatergic elevation in the region (Figure 3.3E; Figure 3.3 – S1C: the onset time of RSC activation is larger than zero; Figure 3.4A), it is not clear whether aRSC neurons fire at all during awake ripples. To address this question, we performed two-photon calcium imaging of the neurons in layers II/III of aRSC. Then, peri-ripple averaging of single-cell calcium traces was performed, and the average traces of neurons over the interval -500 ms to +500 ms were clustered into two clusters using the k-means algorithm with correlation coefficient as the similarity measure. Two was the optimum number of clusters according to the silhouette and Calinski-Harabasz criteria. This analysis revealed that there are at least two equally-sized subpopulations of neurons in aRSC; one whose firing is elevated and one whose firing is suppressed during and right after the awake ripples (Figure 3.4B). Notably, in the ~1s-long interval before the ripple centers, the firing of elevated and suppressed sub-populations was suppressed and elevated, respectively. The pre-ripple modulation of the two sub-populations is consistent with the excitatory and inhibitory ramps observed in Chambers et al. (Chambers et al., 2021). These results show that, despite the presence of significant voltage reduction in aRSC, a substantial sub-population of

neurons manage to fire during awake ripples. However, the timing of their firing does not match that of glutamatergic elevation (firing precedes elevation).

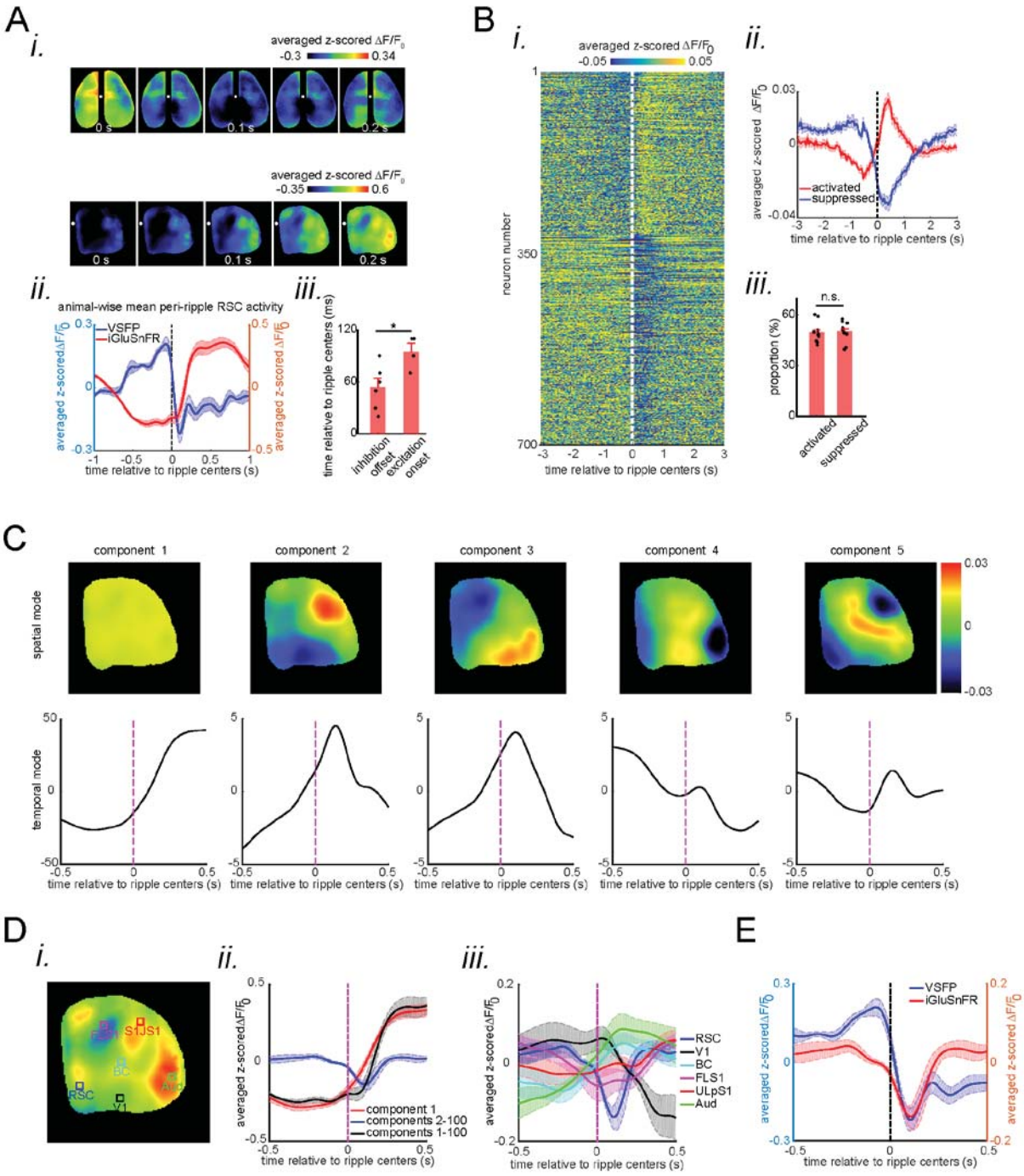

Figure 3.4. A subpopulation of RSC neurons fires during awake ripples despite the presence of strong voltage reduction. (A) (i) five frames taken from the montages shown in Figure 2A and 3A aligned with respect to the ripple center timestamps (zero time). Note the elevation of glutamate signal (excitation) as inhibition eases. Also, note that inhibition is strongest and excitation onset is latest in RSC compared with other regions. (ii) time-series representation of the RSC voltage (blue) and glutamate (red) signals shown in i. Note the onset of excitation is around the offset of inhibition. (iii) Statistical comparison of the inhibition offset time in VSFP mice (n=6) and excitation onset time in Ras iGluSnFR mice (n=4). There is a statistically significant difference between the two (two-sample t-test; $p = 0.02$). Comparing the results in A-ii and B-ii suggests that the majority of neurons in clusters 1 and 2 are modulated by the excitatory and inhibitory forces applied to RSC, respectively. (B) (i) Average calcium trace ($\Delta F/F_0$) for individual neurons 3 seconds before and after ripple centers in a representative animal. The neurons' calcium traces are grouped into two clusters and are sorted based on their cluster membership. During ripples, the neurons in clusters 1 and 2 show elevation and suppression of calcium signal, respectively. (ii) Peri-ripple calcium traces are averaged across neurons in each cluster in each animal and then averaged across 11 animals. The shading represents the standard error of the animal-wise mean. (iii) Statistical comparison of the proportion of neurons in clusters 1 (activated) and 2 (suppressed). There is no significant difference between the two proportions (paired t-test; $p > 0.05$). (C) Spatial and temporal modes associated with first 5 largest singular values (components) of the concatenated stack of peri-ripple iGluSnFR activity in the representative Ras animal presented in Figure 3A-B. Note that the spatial mode of the first component does not show a specific topography and the corresponding temporal mode is dominated by post-ripple elevation of iGluSnFR signal. Also, the amplitude of the first component temporal mode is an order of magnitude larger than that in other components. (D) (i) A representative frame chosen from A with 6 ROIs chosen from 6 different neocortical regions. (ii) Three animal-wise (n = 4) average of reconstructed mean peri-ripple glutamate signals captured from the RSC ROI in D-i. The signals were reconstructed using first (red), second-to-hundredth (blue), and first-to-hundredth (black) components in C. The black signal is the summation of the red and blue ones. Note that the red signal (first component) captured almost all of the elevation seen in the black signal while the blue signal (2-100th components) shows a post-ripple dip. (iii) Animal-wise average of reconstructed mean peri-ripple glutamate signals captured from all the ROIs in D-i color-coded according to the ROIs. The signals were reconstructed using second-to-hundredth components. Note that only RSC show a post-ripple dip. (E) Animal-wise average of mean peri-ripple signals captured from RSC in all VSFP (blue) and Ras iGluSnFR (red) animals. The signals in iGluSnFR animals were reconstructed from 2-100th components after singular value decomposition shown in C. Note that the timing of the dips in both signals match, suggesting they both represent the same phenomenon.

This led us to ask whether the observed glutamate activity consists of components whose activity timings match those of the observed reduction in the voltage and firing in the calcium imaging. To address this question, we performed singular-value decomposition on the concatenated stack of individual peri-ripple glutamate activity stacks. This method decomposed the stack into components with specific spatial (Figure 3.4C upper row) and temporal modes. Then,

for each component, the corresponding temporal mode was chunked around individual ripples, aligned, and averaged (Figure 3.4C lower row). Notably, the first component showed a global post-ripple elevation of glutamate activity whose amplitude was an order of magnitude larger than that in other components. Other components, on the other hand, showed a mixture of elevation and reduction across neocortical regions. These patterns were similar across all the animals. We combined all the components with mixed patterns of modulation (components 2 to 100) and reconstructed the mean peri-ripple glutamate activity across neocortical regions (Figure 3.4D). We observed that the mean peri-ripple glutamate activity in aRSC was decomposed into two specific patterns of post-ripple modulation, positive (Figure 4Dii; red signal; reconstructed from component 1) and negative (blue signal; reconstructed from components 2 to 100). Interestingly, other regions did not show the negative pattern of modulation (Figure 3.4Diii). In addition, the timing of the post-ripple negatively-modulated glutamate signal in aRSC matched that of voltage activity in aRSC (Figure 3.4E), which suggests that one of the factors involved in the reduction of voltage in aRSC is the reduction of excitatory glutamatergic input to the region. Also, the onset time of the positively modulated glutamate signal in aRSC (Figure 3.4Dii) was earlier than that of the original signal, which matched better with the timing of aRSC neurons firing presented in Figure 3.4B.

3.3.4. The timing of peri-ripple glutamatergic activity is layer-dependent

Given different hypothesized functions for superficial and deep layers in association cortices (Burke et al., 2005; McNaughton, 2010), we asked whether the patterns of peri-ripple glutamate activity are layer-dependent. To address this question, we conducted wide-field optical imaging with concurrent CA1 LFP recording in EMX iGluSnFR mice with glutamate indicators

expressed in excitatory neurons across all the neocortical layers (as opposed to Ras mice with only superficial layer expression). Qualitatively, the mean peri-ripple glutamate activity in EMX mice (Figure 3.5A-B) did not differ from that in Ras mice (Figure 3.3A-B). However, the activity in

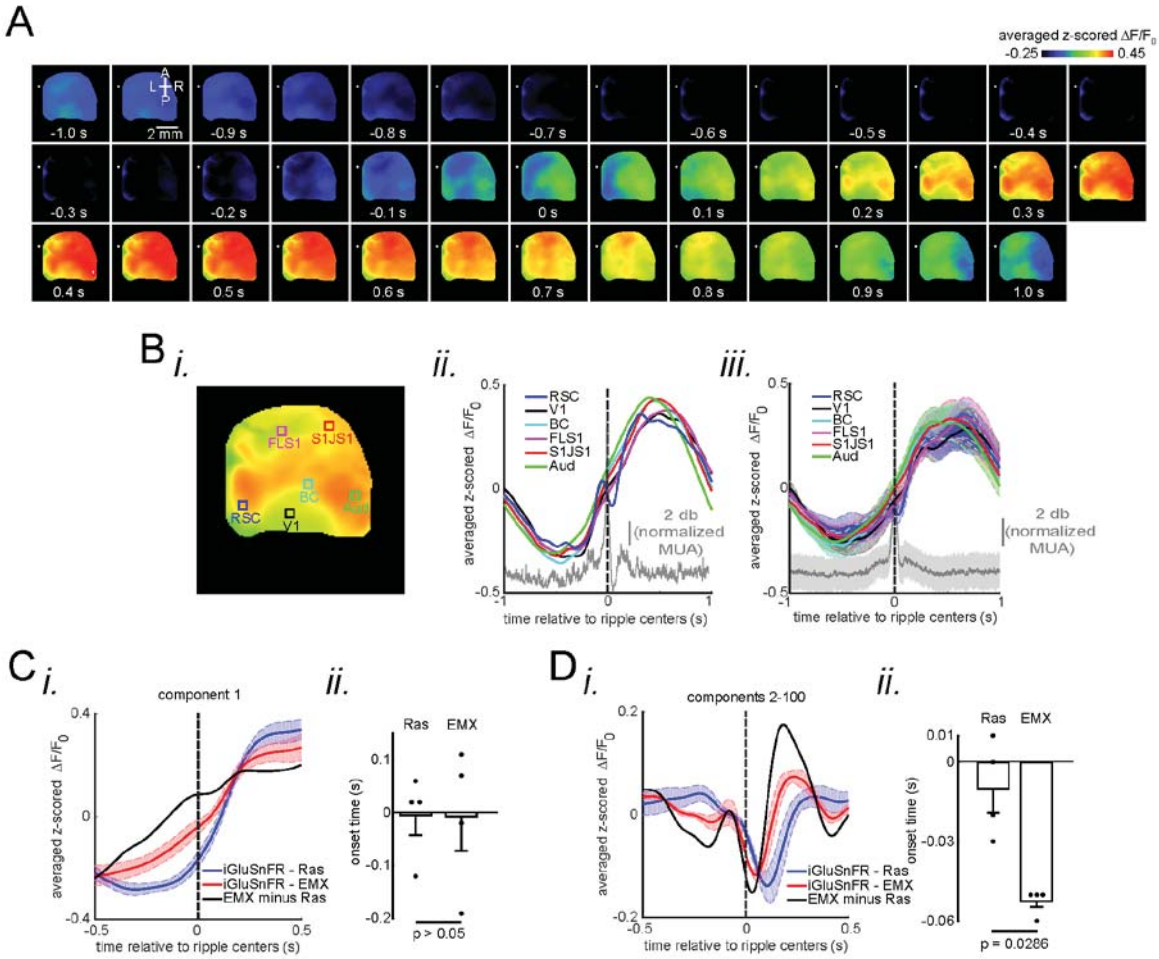

Figure 3.5. Peri-ripple glutamatergic input in superficial neocortical layers is delayed compared with that in deep layers. (A) Montage of average iGluSnFR activity 1 second before and after ripple centers in a representative EMX iGluSnFR animal. Zero time represents the timestamp of center of ripples. Note the elevation of glutamate signal, i.e. excitation, across neocortical regions around ripple times. (B) (i-ii) A representative frame chosen from excitation period in A along with peri-ripple mean iGluSnFR time-series of six regions of interest chosen from retrosplenial cortex (RSC), primary visual cortex (V1), and primary forelimb somatosensory cortex (FLS1), primary lip somatosensory cortex (ULpS1), primary barrel cortex (BC), and primary auditory cortex (Aud). The data represented in time-series format is the same data shown in A. The black/gray trace is the mean normalized MUA activity. (iii) peri-ripple mean iGluSnFR time-series and mean nortmalized MUA activity (black/gray) averaged across 4 mice. The shading represents standard error of the mean (SEM). The glutamate signals in EMX animals are shifted to left (precede) compared with those in Ras animals represented in Figure 3A-B. (C) (i) Animal-wise (n = 4) average of

reconstructed (using 1st component) mean peri-ripple glutamate activity in Ras (blue) and EMX (red) animals. The black trace is the estimated glutamate activity of the depp layers of aRSC. (ii) The statistical comparison of onset time in Ras and EMX signals in i (two-way ranksum test). (D) (i) Animal-wise average of reconstructed (using 2-100th components) mean peri-ripple glutamate activity in Ras (blue) and EMX (red) animals. (ii) The statistical comparison of onset time in Ras and EMX signals in i (two-sided ranksum test). The black trace is the estimated glutamate activity of the depp layers of aRSC.

EMX mice seemed to be shifted to an earlier time (compare Figure 3.3Biii and 5Biii). To probe the potential differences in glutamate activity in Ras and EMX mice, we compared the result of the singular value decomposition analysis. The spatial and temporal modes associated with different components were similar in these two strains (compare Figure 3.4C and Figure 3.5 – S1A). Moreover, the reconstructed signals from the 1st and 2-100th components showed the same pattern of positive and negative modulations, respectively (Figure 3.5 – S1B). We did not find a statistically significant difference in the slope of neither positively- nor negatively modulated signals between Ras and EMX groups. Additionally, although the animal-wise average of positively-modulated aRSC signal showed earlier onset time (Figure 3.5Ci), the statistical comparison between the two groups did not reach the significance threshold of 0.05 (Figure 3.5Cii). However, the onset time of negatively-modulated signal in aRSC was significantly earlier in EMX than that in Ras group (Figure 3.5Dii). We also estimated the glutamate activity of the deep layers of aRSC by subtracting a scaled version of the Ras from the EMX signal (the black trace in Figure 3.5C-Di; $\text{black trace} = \frac{\text{red trace} - 0.5 * \text{blue trace}}{0.5}$). The scaling was performed to accommodate for the potential amount of variance the superficial and deep layers explain in the EMX signal (Newton et al., 2021). The estimated positively- and negatively modulated glutamate signals from the deep layers of aRSC showed a shift to an earlier time (to the left). Furthermore, the estimated negatively-modulated signal (black trace in Figure 3.5Di) showed a noticeable

rebound with a peak around 200 ms after the SWR centers. All in all, these results suggest that deep neocortical layers in aRSC express glutamatergic modulation earlier than superficial layers do.

3.4. Discussion

In this study, we investigated the peri-ripple activity of the neocortex from different angles during the awake state. We utilized voltage, glutamate, and calcium imaging to untangle the activity dynamics in the input, internal, and output levels of neocortical regions, especially in agranular retrosplenial cortex (aRSC). “Input” in this context is considered from the perspective of the dendritic trees occupying the majority of the volume of the superficial layers of the neocortical layers (Chemla and Chavane, 2010a, 2010b). Thus, even self-excitation (i.e. the excitation of the dendrites of a region by the axonal projections originating from the same region) is seen as input in this framework.

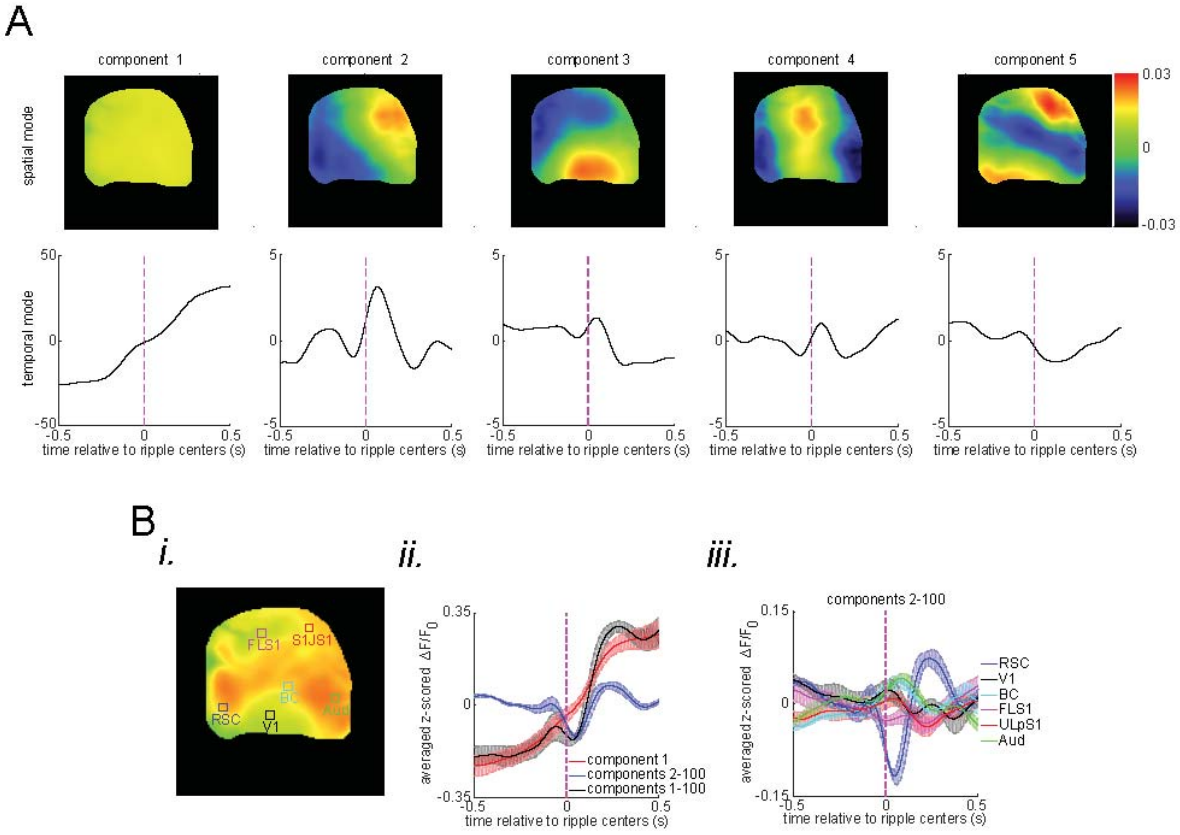

Figure 3.5 – S1. (A) Spatial and temporal modes associated with first 5 largest singular values (components) of the concatenated stack of peri-ripple iGluSnFR activity in the representative EMX animal presented in Figure 5A-B. Note that the spatial mode of the first component does not show a specific topography and the corresponding temporal mode is dominated with post-ripple elevation of iGluSnFR signal. Also, the amplitude of the first component temporal mode is an order of magnitude larger than that in other components. (B) (i) A representative frame chosen from A with 6 ROIs chosen from 6 different neocortical regions. (ii) Three animal-wise average of reconstructed mean peri-ripple glutamate signals captured from the RSC ROI in B-i. The signals were reconstructed using first (red), second-to-hundredth (blue), and first-to-hundredth (black) components in A. The black signal is the summation of the red and blue ones. Note that the red signal (first component) captured almost all of the elevation seen in the black signal while the blue signal (2-100th components) shows a post-ripple dip. (iii) Animal-wise average of reconstructed mean peri-ripple glutamate signals captured from all the ROIs in B-i color-coded according to the ROIs. The signals were reconstructed using second-to-hundredth components. Note that only RSC show a post-ripple dip. The shading represents SEM.

The data revealed a reduction in peri-awake-SWR voltage activity with the strongest and fastest reduction in aRSC. The reduction of voltage activity could be due to at least two factors: 1) reduction of the glutamatergic input 2) gabaergic inhibition. We did not record gabaergic activity to be able to speak about inhibition with certainty. However, the former factor could be investigated using our data. Although the mean peri-awake-SWR glutamate activity did not show a reduction and instead showed a delayed elevation, we probed it further by applying the singular value decomposition (SVD) to see if the glutamate signal was a mixture (multiplex) of negatively- and positively-modulated components. The motivation for investigating the idea of multiplexed glutamate transmission was further fueled by the fact that a significant subpopulation of neurons in aRSC fired despite the significant reduction in voltage as well as seemingly delayed (relative to the SWR centers) glutamate activity in the region.

Singular value decomposition (SVD) was able to decompose the potentially-multiplexed glutamate signal in sRSC and to recover the two patterns of modulations. Notably, the timing of these two patterns matched those of voltage reduction and neural firing (measured by calcium activity) in aRSC. It is worthy of note that SVD is agnostic to excitation and inhibition, and it simply captures the maximum amount of variance in the data. Thus, the two patterns of modulations, which resulted from the application of SVD, may not reflect brain mechanisms. However, the coincidence of the timing of these two patterns with those of voltage reduction and neural firing in aRSC suggests that the SVD output, to some extent, reflects truly different neuronal processes.

Even though the peri-awake-SWR glutamate signal was found to be a mixture of rising and falling components, the amplitude (explained variance) of the rising component was larger than that of the falling component. It suggests that the reduction of the glutamate activity in aRSC is

not the only factor contributing to the reduction of the voltage signal in the region. Therefore, it is plausible that inhibitory input to the superficial layers of aRSC plays a significant role in the reduction of the voltage signal. Moreover, since the majority of the volume of the neocortical superficial layers is filled with dendritic trees (Chemla and Chavane, 2010a, 2010b), dendritic inhibition is probably the major inhibitory process reflected in the reduction of peri-awake-SWR voltage activity.

Another interesting result that came out of the application of SVD on the peri-awake-SWR glutamate activity was the observation that the negatively-modulated component was present only in aRSC and not in other recorded regions while the positively-modulated component was present in all the recorded regions. This observation supports the hypothesis of the presence of peri-awake-SWR inhibition in the neocortex. It is because even though the recorded neocortical regions, except aRSC, did not have a negatively-modulated glutamate activity component, they still showed a reduction in their voltage activity.

Peri-ripple modulation of multiple brain regions, such as ventral tegmental area (Gomperts et al., 2015), subiculum (Chrobak and Buzsáki, 1994; Nitzan et al., 2020b), medial prefrontal (Jadhav et al., 2016; Peyrache et al., 2009; Siapas and Wilson, 1998), anterior cingulate (Wang and Ikemoto, 2016), and entorhinal cortices (Isomura et al., 2006), have been observed. Moreover, our data show that multiple neocortical regions, such as the auditory and barrel cortices, express glutamate elevation before aRSC does. Since the majority of these regions project to aRSC, it is plausible that a peri-awake-SWR excitatory input to aRSC comes indirectly from the hippocampus, or even independently from the hippocampus, through these intermediate neocortical regions. In addition, because some aRSC neurons appear to start firing before the timing of SWR centers, it is also plausible that self-excitation may occur in aRSC. In addition, as

awake SWRs are involved in planning, and planning could lead to the initiation of movement, another potential source of excitation in aRSC could stem from the subcortical structures involved in motion generation.

According to the current literature, there are at least two potential sources for the peri-ripple inhibitory inputs to aRSC. One option is the long-range inhibitory projections emanating from CA1. Although a majority of tracing studies have been focused on the presence of such projections in the granular RSC (gRSC) (Jinno et al., 2007; Miyashita and Rockland, 2007; Yamawaki et al., 2019), it is plausible that they also exist in the agranular RSC (aRSC). The second option is feed-forward inhibition originated from CA1. This mechanism has been reported in gRSC where peri-ripple hippocampal excitatory input activates, via subiculum, the inhibitory interneurons in gRSC which leads to suppression of firing of pyramidal many neurons (Nitzan et al., 2020a; Opalka et al., 2020). Similarly, a recent work found that inhibitory interneurons in superficial layers of aRSC increase their firing during awake ripples which, in turn, could suppress the activity of excitatory neurons (Chambers et al., 2021).

Even though the elevation of neuronal firing is dominant around sleep SWRs, suppression of neuronal firing seems to be an abundant pattern of neuronal modulation around awake ripples. For instance, suppression of neuronal firing around awake hippocampal ripples has been reported in the medial prefrontal cortex (Jadhav et al., 2016) and gRSC (Nitzan et al., 2020b). Both of these regions are heavily involved in mnemonic processing, especially through replaying/reactivating the neural traces associated with previous experiences. Given that the fidelity of awake replays is higher than that of sleep ones (Karlsson & Frank 2009; Tang et al. 2017), it could be reasonably speculated that the peri-ripple inhibition plays a role in this higher fidelity. It probably does so via increasing the signal-to-noise ratio by suppressing the interference of the non-mnemonic neuronal

populations while the mnemonic representations are being replayed during ripples (Jadhav et al., 2016).

Given the coincidence of peri-ripple inhibition and the negatively-modulated component of the glutamatergic activity in superficial layers of aRSC, it could be deduced that the same coincidence would exist in the deep layers as well. This possibility is supported by the observation that reduction of glutamate signal occurred earlier in deep than superficial layers. In that case, the deep layers would receive a peri-ripple inhibitory force before the superficial layers do. Since the back-projection from the hippocampus mainly target the superficial neocortical layers (McNaughton, 2010), the difference in latency of peri-ripple modulation of deep versus superficial neocortical layers could be interpreted from the perspective of the memory indexing theory in the following way: At the time of awake ripples, the hippocampus communicates, via a subspace of neural space, the mnemonic signal as a form of an index code to the superficial layers of RSC. At this time, the deep layers, containing the attributes of past episodic memories, do not receive a mnemonic excitatory drive to avoid interference with the retrieval of index code in the superficial layers (McNaughton, 2010). When the index code is retrieved, it is sent to the deep layers for the memory contents to be retrieved, and now the superficial layers are deprived of the mnemonic excitatory drive to avoid any interference with the content retrieval in deep layers. This hypothesized coordinated and sequential retrieval process in superficial and deep layers (McNaughton, 2010) might be another factor involved in higher fidelity of awake than sleep replays. It is because peri-ripple neocortical inhibition is rare during sleep which could mean that the coordination of retrieval of index and attribute codes is not as strong during sleep as awake states.

3.5. Methods

3.5.1. Animals

6 adult (> 2 months old) male mice with the voltage-sensitive fluorescent protein (VSFP) Butterfly 1.2, expressed in excitatory neurons in neocortical layers II and III, were used for investigating membrane potential dynamics of neocortical regions around awake hippocampal ripples. These mice were generated by crossing the lines Ai78 (Jax023528) (Madisen et al., 2015), Camk2a-tTA (Jax007004), and Rasgrf2-2A-dCre (Jax022864).

4 adult (> 2 months old) female mice with fluorescent glutamate indicator, expressed in excitatory neurons in neocortical layers II and III, were used for investigating dynamics of excitatory synaptic input to the neocortical regions around awake hippocampal ripples. These mice were generated by crossing the lines Ai85 (Jax026260), Camk2a-tTA (Jax007004), and Rasgrf2-2A-dCre (Jax022864).

4 adult (> 2 months old) male mice with fluorescent glutamate indicator, expressed in excitatory neurons in all neocortical layers, were used for investigating dynamics of excitatory synaptic input to the neocortical regions around awake hippocampal ripples. These mice were generated by crossing the lines Ai85 (Jax026260), Camk2a-tTA (Jax007004), and Emx1-Cre (Jax005628).

11 Thy1-GCaMP6s female mice with a fluorescent calcium indicator, expressed in excitatory neurons across all neocortical layers, were used for investigating spiking dynamics of neurons in layers II/III of agranular retrosplenial cortex around awake hippocampal ripples.

Mice were housed in groups of two to five under a 12 hr light-dark cycle. Mice were given ad libitum access to water and standard laboratory mouse diet at all times. After head-

plate/electrode implantation surgery, the mice were single-housed. The animal protocols were approved by the University of Lethbridge Animal Care Committee and were in accordance with guidelines set forth by the Canadian Council for Animal Care.

3.5.2. Surgeries for wide-field voltage and glutamate imaging experiments

On the days of surgery on mice, used in wide-field imaging experiments, subcutaneous injection of buprenorphine (0.5 gr/Kg) was delivered half an hour before the surgery started. Animals were then anesthetized with isoflurane (1–2% mixed in O_2). After reaching the desired depth of anesthesia, the following steps were performed: (1) the skull skin was removed. (2) Hippocampal LFP electrode was implanted. (3) A head-plate was implanted. (4) The muscles covering the lateral portion of the skull (on top of secondary somatosensory and auditory cortices) were removed. This step was performed only for the glutamate imaging experiments where a unilateral imaging window was used. This step allowed us to image the activity of secondary somatosensory and auditory cortices. (5) The skull was covered with a thin and transparent layer of the metabond (Parkell, Inc). (6) The skull was covered with a glass coverslip. An additional bipolar electrode was implanted in the neck muscles for recording EMG activity. Animals were allowed to recover for two weeks before recordings started.

3.5.3. Surgeries for two-photon calcium imaging experiments

On the days of surgery on mice, used in two-photon calcium imaging experiments, subcutaneous injection of buprenorphine (0.5 gr/Kg) was delivered half an hour before the surgery started. Animals were then anesthetized with isoflurane (1–2% mixed in O_2). After reaching the

desired depth of anesthesia, the following steps were performed: (1) the skull skin was removed. (2) A small craniotomy was performed to remove a portion of the skull covering the agranular retrosplenial cortex. (3) The exposed part of the brain was covered with a glass coverslip. (4) Hippocampal LFP electrode was implanted. (5) A head-plate was implanted. (6) An additional bipolar electrode was implanted in the neck muscles for recording EMG activity. Animals were allowed to recover for two weeks before recordings started.

3.5.4. Hippocampal LFP recording

Teflon-coated 50 μm stainless steel wires (A-M Systems) were used to make bipolar hippocampal LFP electrodes. The two tips of the electrode were separate around 0.5 mm so that the tips could record from two different depths. To implant the electrode for wide-field imaging experiments, a hole was drilled on the right hemisphere skull about 2.6 mm lateral to the midline and tangent to the posterior side of the occipital suture. Then, the electrode was gradually lowered through the hole at an angle of 57 degrees with respect to the vertical axis (the axis perpendicular to the surface on which the stereotaxic apparatus was sitting). The electrode signal was being continuously monitored both visually and audibly. Lowering the electrode was stopped as soon as a dramatic increase in the spiking activity was heard and observed for the second time near the calculated coordinate (angle = 57 degrees, depth = ~1.75 mm) for the pyramidal layer of the dorsal CA1. In this way, we ensured that the upper and lower tips of the electrode were placed in and beneath the pyramidal layer of the dorsal CA1, respectively. The electrode was fixated on the skull using Krazy Glue and dental cement. For the two-photon imaging experiments, a similar electrode implantation procedure was used. The only difference was that the electrode was lowered perpendicular to the surface of the brain until it reached the pyramidal layer of the dorsal CA1. In

all the experiments, the hippocampal electrodes were implanted in the right hemispheres ipsilateral to the imaging window. The electrode signals were amplified using a Grass A.C. pre-amplifier Model P511 (Artisan Technology Group, IL) and digitized using a Digidata 1440 (Molecular Device Inc, CA) or National Instruments data acquisition system.

3.5.5. Glutamate imaging

Blue-light-emitting diodes (Luxeon K2, 473 nm, Quadica Developments Inc, Lethbridge, Alberta) augmented with band-pass filters (Chroma Technology Corp, 467–499 nm) were used to excite iGluSnFR indicators. The fluorescence emission from iGluSnFR was filtered with a 520–580 nm band-pass filter (Semrock, New York, NY) and collected as 12-bit images at 100 Hz using a CCD camera (1M60 Pantera, Dalsa, Waterloo, ON) and an EPIX E4DB frame grabber controlled with XCAP 3.7 imaging software (EPIX, Inc, Buffalo Grove, IL). To reduce the effect of large neocortical blood vessels in imaging quality, the lens was focused on the neocortex to a depth of ~1 mm. We also recorded the iGluSnFR signal in response to different periphery stimulation under urethane anesthesia (Mohajerani et al., 2013; Karimi Abadchi et al. 2020) to functionally map the center of the hind-limb somatosensory, fore-limb somatosensory, auditory, visual, and barrel cortices.

3.5.6. Voltage imaging

Blue-light-emitting diodes (Luxeon K2, 473 nm, Quadica Developments Inc, Lethbridge, Alberta) augmented with band-pass filters (Chroma Technology Corp, 467–499 nm) were used to excite the Butterfly indicator. The fluorescence emission from Butterfly FRET fluorophore pair,

mCitrine and mKate2, were filtered with a 520–580 nm and ????? band-pass filters (Semrock, New York, NY), respectively. The two filtered signals were collected as 12-bit images at 100 Hz using two CCD cameras (1M60 Pantera, Dalsa, Waterloo, ON) and two EPIX E4DB frame grabber controlled with a single XCAP 3.7 imaging software (EPIX, Inc, Buffalo Grove, IL). To reduce the effect of large neocortical blood vessels in imaging quality, the lens was focused into the neocortex to a depth of ~1 mm. We also recorded the Butterfly FRET signals in response to different periphery stimulation under urethane anesthesia (Mohajerani et al., 2013; Karimi Abadchi et al. 2020) to functionally map the center of the hind-limb somatosensory, fore-limb somatosensory, auditory, visual, and barrel cortices.

3.5.7. Two-photon calcium imaging

Two-photon calcium imaging was conducted via a Bergamo II multi-photon microscope (THORLABS). Ti:Saphire pulsed laser (Coherent) with wavelength of 920 nm and power of ~80 mW (measured at the tissue) was used to excite the calcium indicators. Scaning of the field of view was done by Galvo-Resonant X-Y mirrors. A 16x water-immersion objective lens (Nikon) with numerical aperture of 0.8 was used for imaging. The emitted light from calcium indicators was collected via a GaAsP photomultiplier tube (Hamamatsu). The field of view size was 835 × 835 µm and frames were captured at spatial resolution of 800 × 800 pixels and temporal resolution of 19.6 Hz. The depths of imaging was aimed between 110 and 190 µm (layers II/III).

3.5.8. Preprocessing of Butterfly (VSFP) imaging data

We followed the ratiometric procedure, described in Carandini et al. 2015, with a modification to preprocess the VSFP data and obtain an estimate of the membrane potential at each pixel. The modification was that we used time-varying quantities for $\overline{A}, \overline{D}, \overline{A_e}$, and $\overline{D_e}$ by calculating trends of these signals using the local regression method. We made this adjustment because we were working with spontaneous neocortical activity recorded over a long period of time while, in the Carandini et al. 2015, peri-stimulus activity over a short interval of time (a couple of seconds) was analyzed.

3.5.9. Preprocessing of iGluSnFR imaging data

First, low-rank reconstruction of the stack of frames, obtained via iGluSnFR imaging, was performed by applying singular-value decomposition and taking the components with the greatest associated singular values (Mitra and Pesaran, 1999). Next, for each pixel in the imaging window, a time-varying baseline (F_0) for the iGluSnFR signal (F) was calculated. Baseline calculation was performed by applying the *locdetrend* function in the Choronux toolbox (http://chronux.org/; Mitra and Bokil, 2007) to fit a piecewise linear curve to the pixels' time series using the local regression method. The calculated baseline signal (F_0) was then subtracted from the raw signal (F), and the difference signal was divided by the baseline values at each time point ($\Delta F/F_0$). At the end, a band pass (0.1–6 Hz) FIR filter was applied on the $\Delta F/F_0$ signal for each pixel.

3.5.10. Preprocessing of two-photon calcium imaging data

The preprocessing of two-photon calcium imaging data was conducted via Suite2p pipeline implemented in Python 3 (Pachitariu et al. 2017). The signals from the detected candidate neuronal ROIs as well as the geometric shape the ROIs were visually inspected to screen for non-somatic compartments. The neuropil component of the calcium traces, estimated by Suite2p, was multiplied by 0.7 and subtracted from the traces (Pachitariu et al. 2017).

3.5.11. SWRs detection

The raw hippocampal LFP was down-sampled to 1 kHz, filtered between 110 to 250 Hz (ripple-band) using real-valued Morlet wavelet implemented in MATLAB (MathWorks). The ripple power signal was generated by rectifying and smoothing the ripple-band filtered signal. Smoothing was performed using a rectangular window with a length of 8 ms. SWRs were identified when the ripple power signal passed the detection threshold defined by the mean plus a multiple of its standard deviation. The numerical value of the standard deviation multiplier was adjusted manually for each animal. A lower threshold (75% of the detection threshold) was used to estimate the onset and offset of each SWR. Detected events were further screened by applying a duration threshold. The timestamp of the largest trough between the onset and offset times of each detected event is referred to as the event center. At the end, events with centers less than 50 ms apart were concatenated.

3.5.12. Exclusion of ripples based on EMG activity

To ensure that the peri-ripple neocortical activity was least affected by movement-related brain activity, the ripples with noticeable EMG activity within ±500 ms were excluded from all the analyses used in this study.

3.5.13. Z-scoring peri-ripple neocortical activity

The z-scoring of peri-ripple traces/frames was performed against a null distribution. The null distribution was obtained from traces centered round random timestamps which did not necessarily correspond to those of ripple centers, and the random timestamps were generated by randomly permuting the intervals between the successive ripple centers. All the individual peri-ripple traces/frames were z-scored against the null distribution before being analyzed further.

3.5.14. Calculating amplitude, slope, and onset of inhibition and/or excitation

For voltage peri-ripple mean traces, to report all the quantities as a positive number, the traces were inverted by multiplying a negative one to them. Inhibition amplitude was calculated as the difference between maximum value of the trace in the interval [0,200ms] and the baseline value. The baseline value was calculated as the mean of the trace in the interval [-200ms,0]. To calculate the onset and offset of the inhibition, the maximum value of the derivative (rate of change) of the voltage traces in the interval [-200ms,200ms] was calculated. Onset and offset of inhibition were defined as the timestamps at which the derivative signal reaches half of its maximum value before and after the maximum value timestamp, respectively. The slope of inhibition was defined as the average slope of the voltage traces between their onset and offset

times. Finally, the pre-ripple amplitude of the voltage traces were calculated by averaging the non-inverted trace values between the timestamps of the half-maximum value.

For glutamate peri-ripple mean traces, all the calculations are the same as those applied to the voltage imaging data except the signal inversion at the very first step was not performed.

3.5.15. Clustering the RSC calcium traces

The z-scored (against the null distribution) peri-ripple calcium traces in the interval [-500ms, 500ms] were further z-scored with respect to their mean and standard deviation and then fed into the k-means algorithm implemented as a built-in function in MATLAB (MathWorks). Correlation was used as the distance measure; however, since the signals were z-scored before, the true distance measure was correlation coefficient.

3.5.16. Calculating the number of bootstrap draws and sampling size

The number of bootstrap draws for voltage (i.e. 193) and for glutamate (i.e. 270) imaging data was calculated to achieve the statistical power of 0.8 at significance level of 0.05 and effect size of 0.25 for a repeated-measure ANOVA design with 8 and 12 groups (i.e. regions), respectively. The power analysis was performed using the G*Power software (Faul, F. et al. 2007).

50 was chosen as the sampling size at each bootstrap draw. This number was chosen since the correlation coefficient between the average of the bootstrap draws and the average of the whole peri-ripple ripples plateaued around this number in all the animals.

3.6.17. Statistical tests

All statistical tests in this study were performed using MATLAB built-in functions. Repeated-measure ANOVA with Greenhouse-Geisser correction for sphericity was performed for testing the hypothesis that there was a region-effect in any of the features (i.e. amplitude, slope, onset/offset time) of the peri-ripple traces. This analysis was followed by performing multiple comparisons with Tukey-Kramer correction. For all the two-group comparisons, two-sample two-sided t-test was used.

4. Conclusion

According to the two-stage model of memory formation (Buzsaki 1989), the neuronal representations of past experiences reactivate in the hippocampus, mainly during sharp-wave ripples (SWRs), that could broadcast stored information to the down-stream neocortical regions. The broadcast of hippocampal indices, according to the hippocampal memory indexing theory (T J Teyler and DiScenna, 1986; Teyler and Rudy, 2007), would lead to reactivation of corresponding neocortical representations. Moreover, the neocortical activity could play a role in the selection of which index code would be reactivated in the hippocampus (T J Teyler and DiScenna, 1986). Thus, around SWRs, a coordinated dynamic interaction between the two structures has been predicted (McClelland et al., 1995; Sutherland and McNaughton, 2000; Teyler and Rudy, 2007).

Examination of this prediction was the main driver for the current thesis work. In this study, the dynamics of the hippocampal-neocortical interactions around SWRs in both sleep and awake states were examined. We took advantage of high spatial resolution and coverage of wide-field optical imaging as well as high temporal resolution of activity-sensitive optical sensors to observe activity dynamics of a large portion of the dorsal neocortex while the hippocampal local field potential (LFP) and multi-unit activity (MUA), obtained from the dorsal CA1, were being recorded. This preparation allowed us to extend previous findings by providing a mesoscale peri-SWR spatiotemporal map of neocortical activity and by investigating the correspondence of the features of the map and of the hippocampal activity.

Chapter 2 was dedicated to probing the dynamics of peri-SWR hippocampal-neocortical interactions in sleep and urethane anesthesia (as a model of sleep) in naïve mice. Two optical sensors, voltage-sensitive dye RS1921, and iGluSnFR, measuring membrane potential and synaptic glutamate transmission, respectively, were used. Since the data from both indicators

yielded similar results across both sleep and anesthetized states, the results obtained from a single pooled dataset were reported. SWR-triggered averaging analysis, revealed a topographically organized pattern of neocortical activity where recorded members of default mode network, i.e. dorsal retrosplenial (RSCd) and posterior parietal (PtA) cortices, were modulated the most while somatosensory areas the least. Moreover, a separate electrophysiology dataset confirmed the topographical organization of the neocortical activity modulations. Next, it was confirmed that the stronger modulation of RSCd and PtA was mainly due to their better coordination with SWRs than to their potentially larger activity amplitude. Furthermore, these regions were the first whose activity underwent modulation leading to a medial-to-lateral temporal gradient of activation. Importantly, the peri-individual-SWR activity of RSCd spanned a continuum of temporal relationship with SWRs such that the bulk of activity could sometimes precede and sometimes follow the peak of SWRs. However, in general, RSCd activity tended to precede the SWRs. This observation led us to investigate the features of hippocampal activity that were correlated with the timing of RSCs activity around SWRs. We found that skewness of CA1 multi-unit activity over an extended interval (i.e. -200ms to 200ms) matched that of RSCd activity. In addition, the occurrence of bundles of SWRs was another factor correlated with the timing of RSCd activation. Our finding suggests that the peri-SWR hippocampal-neocortical interactions are not unidirectional and are not concentrated only between the onset and offset of SWRs. Instead, these interactions are dynamic in a way that both the hippocampus and neocortex engage in mutual waves of activity during which SWRs could occur at any time, and information could be continually exchanged between the two structures.

Chapter 3 was a natural extension of the findings reported in chapter 2. In chapter 3, we investigated the same question but during quiet wakefulness. At first, two groups of transgenic

mice, expressing butterfly voltage and iGluSnFR glutamate sensors in the excitatory neurons of the superficial neocortical layers, were used. Surprisingly, the results coming out of the SWR-triggered averaging of the two sensor signals did not match each other as opposed to the results of the sleep experiments. Although glutamate activity, on average, showed a decrease followed by an increase before and after SRWs, respectively, the voltage signal showed a transient increase followed by a sharp decrease before and after SWRs, respectively. The strongest and sharpest reduction of voltage signal was localized in RSCd. These two paradoxically opposite patterns of glutamate and voltage activity led us to ask whether the RSCd glutamate activity was a mixture of positively- and negatively-modulated components in a way that the negatively-modulated component matched the reduction of the voltage signal. It turned out to be the case. Interestingly, among all the imaged regions, only RSCd showed a negatively-modulated component of the glutamate activity which matched well with its pattern of voltage modulation. To further elucidate the patterns of activity modulation, we used two-photon calcium imaging to monitor the activity of single excitatory cells in superficial layers of RSCd. We found two equally-sized subpopulations of neurons with opposite patterns of modulation, elevated and suppressed patterns, respectively. It appeared that the patterns of peri-SWR voltage and the negatively-modulated component of the glutamate activity matched that of the calcium-suppressed subpopulation while the pattern of positively-modulated component of the glutamate signal matched that of the calcium-elevated subpopulation. However, it remained unsettled as to why the peri-SWR voltage and glutamate activity patterns might have been mapped on those of calcium-suppressed and calcium-elevated subpopulations, respectively. We also compared the patterns of glutamate activity in two groups of transgenic mice, expressing iGluSnFR in excitatory neurons of only the superficial and of all the neocortical layers. Interestingly, we found that both positively- and negatively-modulated

components of the glutamate signal in RSCd were shifted to the left (closer to the SWR peaks) in the all-layer compared with the superficial-layer group. Although we did not perform repeated-measure experiments to have glutamate activity from all versus superficial layers in the same animal and to be able to subtract them, we nevertheless estimated the deep layers peri-ripple glutamate activity by subtracting the activity in the two independent groups of transgenic mice (deep = all - superficial). Our estimation suggested that deep layers may undergo glutamate modulation before the superficial layers do and therefore show a different pattern of modulation. However, confirming this idea requires further investigation, especially by using a transgenic mouse with iGluSnFR expression in only deep neocortical neurons.

5. Future directions

We have used naïve mice with no specific memory in this thesis, and thus, a natural follow-up study could be about investigating the dynamics of peri-SWR hippocampal-neocortical interactions as a function of the age of a recently-formed memory. To achieve control over the age of the memory, a one-shot learning paradigm must be used. It is because gradual learning paradigms, such as almost all paradigms used in the reactivation studies up until now, could trigger multiple rounds of memory encoding/retrieval followed by consolidation which could expedite the consolidation process (Sutherland et al., 2010; Sutherland and Lehmann, 2011) and blur the potential borderline between recent and remote memory. Here, the recency of memory is measured with respect to the time of initial formation but not to the last time it was re-experienced.

Contextual and cued fear conditioning are among the hippocampus-dependent one-shot learning paradigms that generate memories lasting for months in rodents. Moreover, the fear memories could be inducibly retrieved and readily inferred from the rodents' conditioned response, called freezing behaviour. Between the contextual and cued fear conditioning paradigms, the cued version appears to better suit the head-fix preparations required for conducting wide-field optical imaging. It is because, under the head-fixation, the retrieval of the formed memory could be easily induced by presenting the discrete cue, while inducing the memory retrieval by providing enough contextual elements of the original experience would be challenging.

The drawback of using the fear conditioning paradigm in combination with head-fixed preparation, on the other hand, is that the conditioning session has to be conducted in the freely-behaving condition (as opposed to the head-fixed condition for imaging) so that the conditioning and imaging contexts become as different as possible. It is because the head-fixation alone could acquire most of the associative power and become predictive of the unconditioned stimulus if the

conditioning occurs under the head-fixation. Moreover, electrically shocking mice induces abrupt and fast movements whose expression might cause harm to the animals under the head fixation. Although there has been some research work in which the conditioning, as well as retrieval of the fear memory, have taken place under head-fixation (Gillet et al., 2018), a mild amount of electrical current had to be used to reduce the behavioral expression of the shock experience. Then the caveat is that the induced memory using a mild shock might not last enough to be reliably retrieved. To avoid this potential caveat and because we are mainly interested in studying the retrieval and consolidation phase of memory processing, we are willing to accept the abovementioned drawback in return for being able to induce a long-lasting and readily retrievable memory that allows us to study its retrieval and consolidation as a function of its age.

Neuronal patterns of activity, associated with performance on a well-learned task, reactivate during SWRs during both sleep and awake states. However, such reactivation decays relatively quickly with a time constant of ~30 minutes (Kudrimoti et al., 1999). On the other hand, reactivation of novel experiences could last much longer ~10 hours (Giri et al., 2019). Moreover, neuronal traces associated with recently-formed memories explain a smaller fraction of the whole variance of the neuronal correlation structure compared with remotely-formed memories (Kudrimoti et al., 1999). These observations suggest that retrieval of a recently- versus a remotely-formed memory could have a differential effect on both the hippocampal and hippocampal-neocortical reactivation dynamics. We hypothesize that, at the early age of memory when it is not yet fully incorporated into the existing neocortical representations, hippocampal neuronal activity during SWRs is expected to predict upcoming neocortical activity more often than at the later age of the memory when it is presumably integrated with the neocortical representations. Therefore, we will start our investigation by addressing two specific questions: 1) Do retrieval-induced

patterns of neocortical activity evolve as a function of memory age, as multiple studies have suggested (Bontempi et al., 1999; Frankland and Bontempi, 2005; Wheeler et al., 2013), and if so, what are the characteristics of such evolution? 2) Do dynamics of post-retrieval peri-SWR hippocampal-neocortical interactions change as the memory ages, and if so, in what manner?

References

Afrashteh N, Inayat S, Mohsenvand M, Mohajerani MH. 2017. Optical-flow analysis toolbox for characterization of spatiotemporal dynamics in mesoscale optical imaging of brain activity. *Neuroimage* **153**:58–74. doi:10.1016/J.NEUROIMAGE.2017.03.034

Alexander AS, Rangel LM, Tingley D, Nitz DA. 2018. Neurophysiological signatures of temporal coordination between retrosplenial cortex and the hippocampal formation. *Behav Neurosci* **132**:453–468. doi:10.1037/bne0000254

Amaral DG, Witter MP. 1989. The three-dimensional organization of the hippocampal formation: A review of anatomical data. *Neuroscience* **31**:571–591. doi:10.1016/0306-4522(89)90424-7

Arieli a, Shoham D, Hildesheim R, Grinvald a. 1995. Coherent spatiotemporal patterns of ongoing activity revealed by real-time optical imaging coupled with single-unit recording in the cat visual cortex. *J Neurophysiol* **73**:2072–2093.

Barthó P, Slézia A, Mátyás F, Faradzs-Zade L, Ulbert I, Harris KD, Acsády L. 2014. Ongoing network state controls the length of sleep spindles via inhibitory activity. *Neuron* **82**:1367–1379. doi:10.1016/j.neuron.2014.04.046

Battaglia FP, Sutherland GR, McNaughton BL. 2004. Hippocampal sharp wave bursts coincide with neocortical "up-state" transitions. *Learn Mem* **11**:697–704. doi:10.1101/lm.73504

Belitski A, Gretton A, Magri C, Murayama Y, Montemurro MA, Logothetis NK, Panzeri S. 2008. Low-frequency local field potentials and spikes in primary visual cortex convey independent visual information. *J Neurosci* **28**:5696–709. doi:10.1523/JNEUROSCI.0009-08.2008

Benchenane K, Peyrache A, Khamassi M, Tierney PL, Gioanni Y, Battaglia FP, Wiener SI. 2010. Coherent Theta Oscillations and Reorganization of Spike Timing in the Hippocampal- Prefrontal Network upon Learning. *Neuron* **66**:921–936. doi:10.1016/j.neuron.2010.05.013

Berens P. 2009. CircStat : A MATLAB Toolbox for Circular Statistics . *J Stat Softw* **31**. doi:10.18637/jss.v031.i10

Bermudez-Contreras E, Chekhov S, Sun J, Tarnowsky J, McNaughton BL, Mohajerani MH. 2018. High-performance, inexpensive setup for simultaneous multisite recording of electrophysiological signals and mesoscale voltage imaging in the mouse cortex. *Neurophotonics* **5**:1. doi:10.1117/1.NPh.5.2.025005

Berners-Lee A, Wu X, Foster DJ. 2021. Prefrontal Cortical Neurons Are Selective for Non-Local Hippocampal Representations during Replay and Behavior. *J Neurosci* **41**:5894–5908. doi:10.1523/JNEUROSCI.1158-20.2021

Bontempi B, Laurent-Demir C, Destrade C, Jaffard R. 1999. Time-dependent reorganization of brain circuitry underlying long-term memory storage. *Nature* **400**:671–675. doi:10.1038/23270

Burke SN, Chawla MK, Penner MR, Crowell BE, Worley PF, Barnes CA, McNaughton BL. 2005. Differential Encoding of Behavior and Spatial Context in Deep and Superficial Layers of the Neocortex. *Neuron* **45**:667–674. doi:10.1016/J.NEURON.2005.01.042

Buzsaki G. 1998. Memory consolidation during sleep: a neurophysiological perspective. *J Sleep Res* **7**:17–23. doi:10.1046/J.1365-2869.7.S1.3.X

Buzsáki G. 2015. Hippocampal sharp wave-ripple: A cognitive biomarker for episodic memory and planning. *Hippocampus*. doi:10.1002/hipo.22488

Buzsáki G. 1996. The Hippocampo-Neocortical Dialogue. *Cereb Cortex* **6**:81–92. doi:10.1093/CERCOR/6.2.81

Buzsáki G. 1989. Two-stage model of memory trace formation: A role for "noisy" brain states. *Neuroscience* **31**:551–570. doi:10.1016/0306-4522(89)90423-5

Chambers AR, Berge CN, Vervaeke K. 2021. Cell-type-specific silence in thalamocortical circuits precedes hippocampal sharp-wave ripples. *bioRxiv* 2021.05.05.442741. doi:10.1101/2021.05.05.442741

Chemla S, Chavane F. 2010a. Voltage-sensitive dye imaging: Technique review and models. *J Physiol Paris* **104**:40–50. doi:10.1016/j.jphysparis.2009.11.009

Chemla S, Chavane F. 2010b. A biophysical cortical column model to study the multi-component origin of the VSDI signal. *Neuroimage* **53**:420–438. doi:10.1016/J.NEUROIMAGE.2010.06.026

Chrobak JJ, Buzsáki G. 1996. High-frequency oscillations in the output networks of the hippocampal-entorhinal axis of the freely behaving rat. *J Neurosci* **16**:3056–66. doi:10.1523/JNEUROSCI.16-09-03056.1996

Chrobak JJ, Buzsáki G. 1994. Selective activation of deep layer (V-VI) retrohippocampal cortical neurons during hippocampal sharp waves in the behaving rat. *J Neurosci* **14**:6160–6170. doi:10.1523/jneurosci.14-10-06160.1994

Clement E a., Richard A, Thwaites M, Ailon J, Peters S, Dickson CT. 2008. Cyclic and sleep-like spontaneous alternations of brain state under urethane anaesthesia. *PLoS One* **3**. doi:10.1371/journal.pone.0002004

Csicsvari J, Hirase H, Mamiya A, Buzsáki G. 2000. Ensemble patterns of hippocampal CA3-CA1 neurons during sharp wave-associated population events. *Neuron* **28**:585–94.

Davidson TJ, Kloosterman F, Wilson MA. 2009a. Hippocampal replay of extended experience. *Neuron* **63**:497–507. doi:10.1016/j.neuron.2009.07.027

Davidson TJ, Kloosterman F, Wilson MA. 2009b. Hippocampal replay of extended experience. *Neuron* **63**:497–507. doi:10.1016/j.neuron.2009.07.027

Diba K, Buzsáki G. 2007. Forward and reverse hippocampal place-cell sequences during ripples. *Nat Neurosci 2007 1010* **10**:1241–1242. doi:10.1038/nn1961

Dupret D, O'Neill J, Pleydell-Bouverie B, Csicsvari J. 2010. The reorganization and reactivation of hippocampal maps predict spatial memory performance. *Nat Neurosci* **13**:995–1002.

doi:10.1038/nn.2599

Ego-Stengel V, Wilson MA. 2010. Disruption of ripple-associated hippocampal activity during rest impairs spatial learning in the rat. *Hippocampus* **20**:1–10. doi:10.1002/hipo.20707

Eschenko O, Ramadan W, Mölle M, Born J, Sara SJ. 2008. Sustained increase in hippocampal sharp-wave ripple activity during slow-wave sleep after learning. *Learn Mem* **15**:222–8. doi:10.1101/lm.726008

Euston DR, Tatsuno M, McNaughton BL. 2007. Fast-forward playback of recent memory sequences in prefrontal cortex during sleep. *Science* **318**:1147–50. doi:10.1126/science.1148979

Ferezou I, Haiss F, Gentet LJ, Aronoff R, Weber B, Petersen CCH. 2007. Spatiotemporal Dynamics of Cortical Sensorimotor Integration in Behaving Mice. *Neuron* **56**:907–923. doi:10.1016/j.neuron.2007.10.007

Fernández-Ruiz A, Oliva A, de Oliveira EF, Rocha-Almeida F, Tingley D, Buzsáki G. 2019. Long-duration hippocampal sharp wave ripples improve memory. *Science (80-)* **364**:1082–1086. doi:10.1126/SCIENCE.AAX0758/SUPPL_FILE/AAX0758_FERNANDEZ-RUIZ_SM.PDF

Foster DJ, Wilson MA. 2006. Reverse replay of behavioural sequences in hippocampal place cells during the awake state. *Nat 2006 4407084* **440**:680–683. doi:10.1038/nature04587

Frankland PW, Bontempi B. 2005. The organization of recent and remote memories. *Nat Rev Neurosci* **6**:119–30. doi:10.1038/nrn1607

Gais S, Albouy G, Boly M, Dang-Vu TT, Darsaud A, Desseilles M, Rauchs G, Schabus M, Sterpenich V, Vandewalle G, Maquet P, Peigneux P. 2007. Sleep transforms the cerebral trace of declarative memories. *Proc Natl Acad Sci U S A* **104**:18778–83. doi:10.1073/pnas.0705454104

Gillespie AK, Maya DAA, Denovellis EL, Liu DF, Kastner DB, Coulter ME, Roumis DK, Eden UT, Frank LM. 2021. Hippocampal replay reflects specific past experiences rather than a plan for subsequent choice. *Neuron* **0**. doi:10.1016/J.NEURON.2021.07.029

Gillet SN, Kato HK, Justen MA, Lai M, Isaacson JS. 2018. Fear learning regulates cortical sensory representations by suppressing habituation. *Front Neural Circuits* **11**:112. doi:10.3389/FNCIR.2017.00112/BIBTEX

Girardeau G, Benchenane K, Wiener SI, Buzsáki G, Zugaro MB. 2009. Selective suppression of hippocampal ripples impairs spatial memory. *Nat Neurosci* **12**:1222–3. doi:10.1038/nn.2384

Girardeau G, Cei A, Zugaro M. 2014. Learning-induced plasticity regulates hippocampal sharp wave-ripple drive. *J Neurosci* **34**:5176–83. doi:10.1523/JNEUROSCI.4288-13.2014

Giri B, Miyawaki H, Mizuseki K, Cheng S, Diba K. 2019. Hippocampal reactivation extends for several hours following novel experience. *J Neurosci* **39**:866–875. doi:10.1523/JNEUROSCI.1950-18.2018

Gomperts SN, Kloosterman F, Wilson MA. 2015. VTA neurons coordinate with the

hippocampal reactivation of spatial experience. *Elife* **4**. doi:10.7554/eLife.05360

Goode TD, Tanaka KZ, Sahay A, McHugh TJ. 2020. An Integrated Index: Engrams, Place Cells, and Hippocampal Memory. *Neuron* **107**:805–820. doi:10.1016/J.NEURON.2020.07.011

Greenberg A, Abadchi JK, Dickson CT, Mohajerani MH. 2018. New waves: Rhythmic electrical field stimulation systematically alters spontaneous slow dynamics across mouse neocortex. *Neuroimage* **174**:328–339. doi:10.1016/j.neuroimage.2018.03.019

Gridchyn I, Schoenenberger P, Neill JO, Csicsvari J, Gridchyn I, Schoenenberger P, Neill JO, Csicsvari J. 2020. Assembly-Specific Disruption of Hippocampal Replay Leads to Selective Memory Deficit Article Assembly-Specific Disruption of Hippocampal Replay Leads to Selective Memory Deficit. *Neuron* **0**:1–10. doi:10.1016/j.neuron.2020.01.021

Helfrich RF, Lendner JD, Mander BA, Guillen H, Paff M, Mnatsakanyan L, Vadera S, Walker MP, Lin JJ, Knight RT. 2019. Bidirectional prefrontal-hippocampal dynamics organize information transfer during sleep in humans. *Nat Commun* **10**. doi:10.1038/s41467-019-11444-x

HF Ó, F C, C B. 2017. Task Demands Predict a Dynamic Switch in the Content of Awake Hippocampal Replay. *Neuron* **96**:925-935.e6. doi:10.1016/J.NEURON.2017.09.035

Hoffman KL, McNaughton BL. 2002. Coordinated reactivation of distributed memory traces in primate neocortex. *Science* **297**:2070–3. doi:10.1126/science.1073538

Huang ZJ, Zeng H. 2013. Genetic approaches to neural circuits in the mouse. *Annu Rev Neurosci* **36**:183–215. doi:10.1146/annurev-neuro-062012-170307

Iadecola C, Nedergaard M. 2007. Glial regulation of the cerebral microvasculature. *Nat Neurosci* **10**:1369–1376. doi:10.1038/nn2003

Isomura Y, Sirota A, Özen S, Montgomery S, Mizuseki K, Henze D a., Buzsáki G. 2006. Integration and Segregation of Activity in Entorhinal-Hippocampal Subregions by Neocortical Slow Oscillations. *Neuron* **52**:871–882. doi:10.1016/j.neuron.2006.10.023

Jadhav SP, Kemere C, German PW, Frank LM. 2012. Awake hippocampal sharp-wave ripples support spatial memory. *Science* **336**:1454–8. doi:10.1126/science.1217230

Jadhav SP, Rothschild G, Roumis DK, Frank LM. 2016. Coordinated Excitation and Inhibition of Prefrontal Ensembles during Awake Hippocampal Sharp-Wave Ripple Events. *Neuron* **90**:113–127. doi:10.1016/j.neuron.2016.02.010

Ji D, Wilson MA. 2007. Coordinated memory replay in the visual cortex and hippocampus during sleep. *Nat Neurosci* **10**:100–7. doi:10.1038/nn1825

Jiang X, Shamie I, K Doyle W, Friedman D, Dugan P, Devinsky O, Eskandar E, Cash SS, Thesen T, Halgren E. 2017. Replay of large-scale spatio-temporal patterns from waking during subsequent NREM sleep in human cortex. *Sci Rep* **7**:17380. doi:10.1038/s41598-017-17469-w

Jinno S, Klausberger T, Marton LF, Dalezios Y, Roberts JDB, Fuentealba P, Bushong EA, Henze D, Buzsaki G, Somogyi P. 2007. Neuronal Diversity in GABAergic Long-Range

Projections from the Hippocampus. *J Neurosci* **27**:8790–8804. doi:10.1523/JNEUROSCI.1847-07.2007

Johnson L a, Euston DR, Tatsuno M, McNaughton BL. 2010. Stored-trace reactivation in rat prefrontal cortex is correlated with down-to-up state fluctuation density. *J Neurosci* **30**:2650–2661. doi:10.1523/JNEUROSCI.1617-09.2010

Joo HR, Frank LM. 2018. The hippocampal sharp wave–ripple in memory retrieval for immediate use and consolidation. *Nat Rev Neurosci*. doi:10.1038/s41583-018-0077-1

Kaefer K, Nardin M, Blahna K, Csicsvari J. 2020. Replay of Behavioral Sequences in the Medial Prefrontal Cortex during Rule Switching. *Neuron* **106**:154-165.e6. doi:10.1016/J.NEURON.2020.01.015

Kaplan R, Adhikari MH, Hindriks R, Mantini D, Murayama Y, Logothetis NK, Deco G. 2016. Hippocampal Sharp-Wave Ripples Influence Selective Activation of the Default Mode Network. *Curr Biol* **26**:686–691. doi:10.1016/j.cub.2016.01.017

Khodagholy D, Gelinas JN, Buzsáki G. 2017. Learning-enhanced coupling between ripple oscillations in association cortices and hippocampus. *Science* **358**:369–372. doi:10.1126/science.aan6203

Klinzing JG, Niethard N, Born J. 2019. Mechanisms of systems memory consolidation during sleep. *Nat Neurosci*. doi:10.1038/s41593-019-0467-3

Kudrimoti HS, Barnes CA, McNaughton BL. 1999. Reactivation of hippocampal cell assemblies: effects of behavioral state, experience, and EEG dynamics. *J Neurosci* **19**:4090–101. doi:10.1523/JNEUROSCI.19-10-04090.1999

Kyweriga M, Sun J, Wang S, Kline R, Mohajerani MH. 2017. A Large Lateral Craniotomy Procedure for Mesoscale Wide-field Optical Imaging of Brain Activity. *J Vis Exp*. doi:10.3791/52642

Lavenex P, Amaral DG. 2000. Hippocampal-neocortical interaction: A hierarchy of associativity. *Hippocampus* **10**:420–430. doi:10.1002/1098-1063(2000)10:4<420::AID-HIPO8>3.0.CO;2-5

Lee AK, Wilson MA. 2002. Memory of sequential experience in the hippocampus during slow wave sleep. *Neuron* **36**:1183–94. doi:10.1016/S0896-6273(02)01096-6

Logothetis NK, Eschenko O, Murayama Y, Augath M, Steudel T, Evrard HC, Besserve M, Oeltermann a. 2012. Hippocampal-cortical interaction during periods of subcortical silence. *Nature* **491**:547–53. doi:10.1038/nature11618

Madisen L, Garner AR, Shimaoka D, Chuong AS, Klapoetke NC, Li L, van der Bourg A, Niino Y, Egolf L, Monetti C, Gu H, Mills M, Cheng A, Tasic B, Nguyen TN, Sunkin SM, Benucci A, Nagy A, Miyawaki A, Helmchen F, Empson RM, Knöpfel T, Boyden ES, Reid RC, Carandini M, Zeng H. 2015. Transgenic Mice for Intersectional Targeting of Neural Sensors and Effectors with High Specificity and Performance. *Neuron* **85**:942–958. doi:10.1016/j.neuron.2015.02.022

Maingret N, Girardeau G, Todorova R, Goutierre M, Zugaro M. 2016. Hippocampo-cortical

coupling mediates memory consolidation during sleep. *Nat Neurosci*. doi:10.1038/nn.4304

Marr D. 1971. Simple Memory: A Theory for Archicortex. *Philos Trans R Soc B Biol Sci* **262**:23–81. doi:10.1098/rstb.1971.0078

Marvin JS, Borghuis BG, Tian L, Cichon J, Harnett MT, Akerboom J, Gordus A, Renninger SL, Chen T-W, Bargmann CI, Orger MB, Schreiter ER, Demb JB, Gan W-B, Hires SA, Looger LL. 2013a. An optimized fluorescent probe for visualizing glutamate neurotransmission. *Nat Methods* **10**:162–170. doi:10.1038/nmeth.2333

Marvin JS, Borghuis BG, Tian L, Cichon J, Harnett MT, Akerboom J, Gordus A, Renninger SL, Chen T-W, Bargmann CI, Orger MB, Schreiter ER, Demb JB, Gan W-B, Hires SA, Looger LL. 2013b. An optimized fluorescent probe for visualizing glutamate neurotransmission. *Nat Methods* **10**:162–170. doi:10.1038/nmeth.2333

Massimini M, Huber R, Ferrarelli F, Hill S, Tononi G. 2004. The sleep slow oscillation as a traveling wave. *J Neurosci* **24**:6862–6870. doi:10.1523/JNEUROSCI.1318-04.2004

McClelland JL, McNaughton BL, O'Reilly RC. 1995. Why there are complementary learning systems in the hippocampus and neocortex: Insights from the successes and failures of connectionist models of learning and memory. *Psychol Rev* **102**:419–457. doi:10.1037/0033-295X.102.3.419

McNaughton BL. 2010. Cortical hierarchies, sleep, and the extraction of knowledge from memory. *Artif Intell* **174**:205–214. doi:10.1016/J.ARTINT.2009.11.013

McNaughton BL, Morris RGM. 1987. Hippocampal synaptic enhancement and information storage within a distributed memory system. *Trends Neurosci* **10**:408–415. doi:10.1016/0166-2236(87)90011-7

Milior G, Castro MA Di, Sciarria LP, Garofalo S, Branchi I, Ragozzino D, Limatola C, Maggi L. 2016. Electrophysiological Properties of CA1 Pyramidal Neurons along the Longitudinal Axis of the Mouse Hippocampus. *Sci Rep* **6**. doi:10.1038/srep38242

Mitra P, Bokil H. 2007. Observed Brain Dynamics. Oxford University Press. doi:10.1093/acprof:oso/9780195178081.001.0001

Mitra PP, Pesaran B. 1999. Analysis of Dynamic Brain Imaging Data. *Biophys J* **76**:691–708. doi:10.1016/S0006-3495(99)77236-X

Miyashita T, Rockland KS. 2007. GABAergic projections from the hippocampus to the retrosplenial cortex in the rat. *Eur J Neurosci* **26**:1193–1204. doi:10.1111/j.1460-9568.2007.05745.x

Mohajerani MH, Chan AW, Mohsenvand M, LeDue J, Liu R, McVea DA, Boyd JD, Wang YT, Reimers M, Murphy TH. 2013. Spontaneous cortical activity alternates between motifs defined by regional axonal projections. *Nat Neurosci* **16**:1426–1435. doi:10.1038/nn.3499

Mohajerani MH, McVea D a, Fingas M, Murphy TH. 2010. Mirrored bilateral slow-wave cortical activity within local circuits revealed by fast bihemispheric voltage-sensitive dye imaging in anesthetized and awake mice. *J Neurosci* **30**:3745–3751. doi:10.1523/JNEUROSCI.6437-09.2010

Mölle M, Yeshenko O, Marshall L, Sara SJ, Born J. 2006. Hippocampal sharp wave-ripples linked to slow oscillations in rat slow-wave sleep. *J Neurophysiol* **96**:62–70. doi:10.1152/jn.00014.2006

Nádasdy Z, Hirase H, Czurkó A, Csicsvari J, Buzsáki G. 1999. Replay and time compression of recurring spike sequences in the hippocampus. *J Neurosci* **19**:9497–507. doi:10.1523/JNEUROSCI.19-21-09497.1999

Newton TH, Reimann MW, Abdellah M, Chevtchenko G, Muller EB, Markram H. 2021. In silico voltage-sensitive dye imaging reveals the emergent dynamics of cortical populations. *Nat Commun 2021 121* **12**:1–13. doi:10.1038/s41467-021-23901-7

Ngo HV V., Seibold M, Boche DC, Mölle M, Born J. 2019. Insights on auditory closed-loop stimulation targeting sleep spindles in slow oscillation up-states. *J Neurosci Methods* **316**:117–124. doi:10.1016/j.jneumeth.2018.09.006

Niethard N, Ngo H-V V, Ehrlich I, Born J. 2018. Cortical circuit activity underlying sleep slow oscillations and spindles. *Proc Natl Acad Sci U S A* **115**:E9220–E9229. doi:10.1073/pnas.1805517115

Nitzan N, McKenzie S, Beed P, English DF, Oldani S, Tukker JJ, Buzsáki G, Schmitz D. 2020a. Propagation of hippocampal ripples to the neocortex by way of a subiculum-retrosplenial pathway. *Nat Commun 2020 111* **11**:1–17. doi:10.1038/s41467-020-15787-8

Nitzan N, McKenzie S, Beed PS, English DF, Oldani S, Tukker JJ, Buzsaki G, Schmitz D. 2020b. Propagation of Hippocampal Ripples to the Neocortex by Way of a Subiculum-Retrosplenial Pathway. *bioRxiv* 2020.02.27.966770. doi:10.1101/2020.02.27.966770

Norimoto H, Makino K, Gao M, Shikano Y, Okamoto K, Ishikawa T, Sasaki T, Hioki H, Fujisawa S, Ikegaya Y. 2018. Hippocampal ripples down-regulate synapses. *Science (80-)* **359**:1524–1527. doi:10.1126/SCIENCE.AAO0702/SUPPL_FILE/PAP.PDF

Norman Y, Yeagle EM, Khuvis S, Harel M, Mehta AD, Malach R. 2019. Hippocampal sharp-wave ripples linked to visual episodic recollection in humans. *Science (80-)* **365**. doi:10.1126/science.aax1030

Ólafsdóttir HF, Bush D, Barry C. 2018. The Role of Hippocampal Replay in Memory and Planning. *Curr Biol* **28**:R37–R50. doi:10.1016/J.CUB.2017.10.073

Opalka AN, Huang W, Liu J, Liang H, Wang D V. 2020. Hippocampal Ripple Coordinates Retrosplenial Inhibitory Neurons during Slow-Wave Sleep. *Cell Rep* **30**:432-441.e3. doi:10.1016/j.celrep.2019.12.038

Pagliardini S, Funk GD, Dickson CT. 2013a. Breathing and brain state: Urethane anesthesia as a model for natural sleep. *Respir Physiol Neurobiol* **188**:324–332. doi:10.1016/j.resp.2013.05.035

Pagliardini S, Gosgnach S, Dickson CT. 2013b. Spontaneous Sleep-Like Brain State Alternations and Breathing Characteristics in Urethane Anesthetized Mice. *PLoS One* **8**:1–10. doi:10.1371/journal.pone.0070411

Patel J, Schomburg EW, Berényi A, Fujisawa S, Buzsáki G. 2013. Local generation and

propagation of ripples along the septotemporal axis of the hippocampus. *J Neurosci* **33**:17029–41. doi:10.1523/JNEUROSCI.2036-13.2013

Pavlides C, Winson J. 1989. Influences of hippocampal place cell firing in the awake state on the activity of these cells during subsequent sleep episodes. *J Neurosci* **9**:2907–18.

Peyrache A, Battaglia FP, Destexhe A. 2011. Inhibition recruitment in prefrontal cortex during sleep spindles and gating of hippocampal inputs. *Proc Natl Acad Sci U S A* **108**:17207–12. doi:10.1073/pnas.1103612108

Peyrache A, Khamassi M, Benchenane K, Wiener SI, Battaglia FP. 2009. Replay of rule-learning related neural patterns in the prefrontal cortex during sleep. *Nat Neurosci* **12**:919–26. doi:10.1038/nn.2337

Pfeiffer BE, Foster DJ. 2013. Hippocampal place-cell sequences depict future paths to remembered goals. *Nature* **497**:74–79. doi:10.1038/nature12112

Qin Yu-Lin, Mcnaughton BL, Skaggs WE, Barnes CA. 1997. Memory reprocessing in corticocortical and hippocampocortical neuronal ensembles. *Philos Trans R Soc London Ser B Biol Sci* **352**:1525–1533. doi:10.1098/rstb.1997.0139

Qin Y.-L., Mcnaughton BL, Skaggs WE, Barnes CA. 1997. Memory reprocessing in corticocortical and hippocampocortical neuronal ensembles. *Philos Trans R Soc B Biol Sci* **352**:1525–1533. doi:10.1098/rstb.1997.0139

Ramadan W, Eschenko O, Sara SJ. 2009. Hippocampal Sharp Wave/Ripples during Sleep for Consolidation of Associative Memory. *PLoS One* **4**:e6697. doi:10.1371/JOURNAL.PONE.0006697

Ramirez-Villegas JF, Logothetis NK, Besserve M. 2015. Diversity of sharp-wave-ripple LFP signatures reveals differentiated brain-wide dynamical events. *Proc Natl Acad Sci U S A*. doi:10.1073/pnas.1518257112

Rothschild G. 2019. The transformation of multi-sensory experiences into memories during sleep. *Neurobiol Learn Mem* **160**:58–66. doi:10.1016/j.nlm.2018.03.019

Rothschild G, Eban E, Frank LM. 2017. A cortical-hippocampal-cortical loop of information processing during memory consolidation. *Nat Neurosci* **20**:251–259. doi:10.1038/nn.4457

Rothschild G, Eban E, Frank LM. 2016. A cortical–hippocampal–cortical loop of information processing during memory consolidation. *Nat Neurosci*. doi:10.1038/nn.4457

Roumis DK, Frank LM. 2015. Hippocampal sharp-wave ripples in waking and sleeping states. *Curr Opin Neurobiol* **35**:6–12. doi:10.1016/j.conb.2015.05.001

Roux L, Hu B, Eichler R, Stark E, Buzsáki G. 2017. Sharp wave ripples during learning stabilize the hippocampal spatial map. *Nat Neurosci 2017 206* **20**:845–853. doi:10.1038/nn.4543

Schwindel CD, McNaughton BL. 2011. Hippocampal-cortical interactions and the dynamics of memory trace reactivation. *Prog Brain Res* **193**:163–77. doi:10.1016/B978-0-444-53839-0.00011-9

Scoville WB, Milner B. 1957. LOSS OF RECENT MEMORY AFTER BILATERAL

HIPPOCAMPAL LESIONS. *J Neurol Neurosurg Psychiatry* **20**:11. doi:10.1136/JNNP.20.1.11

Shen B, McNaughton BL. 1996. Modeling the spontaneous reactivation of experience-specific hippocampal cell assembles during sleep. *Hippocampus* **6**:685–692. doi:10.1002/(SICI)1098-1063(1996)6:6<685::AID-HIPO11>3.0.CO;2-X

Shin JD, Tang W, Jadhav SP. 2019. Dynamics of Awake Hippocampal-Prefrontal Replay for Spatial Learning and Memory-Guided Decision Making. *Neuron*. doi:10.1016/j.neuron.2019.09.012

Shoham D, Glaser DE, Arieli a, Kenet T, Wijnbergen C, Toledo Y, Hildesheim R, Grinvald a. 1999. Imaging cortical dynamics at high spatial and temporal resolution with novel blue voltage-sensitive dyes. *Neuron* **24**:791–802. doi:S0896-6273(00)81027-2 [pii]

Siapas AG, Wilson M a. 1998. Coordinated interactions between hippocampal ripples and cortical spindles during slow-wave sleep. *Neuron* **21**:1123–1128. doi:10.1016/S0896-6273(00)80629-7

Sirota A, Csicsvari J, Buhl D, Buzsáki G. 2003. Communication between neocortex and hippocampus during sleep in rodents. *Proc Natl Acad Sci U S A* **100**:2065–2069. doi:10.1073/pnas.0437938100

Skaggs WE, McNaughton BL. 1996. Replay of neuronal firing sequences in rat hippocampus during sleep following spatial experience. *Science* **271**:1870–3. doi:10.1126/SCIENCE.271.5257.1870

Smith V, Mitchell DJ, Duncan J. 2018. Role of the Default Mode Network in Cognitive Transitions. *Cereb Cortex* **28**:3685–3696. doi:10.1093/cercor/bhy167

Stafford JM, Jarrett BR, Miranda-Dominguez O, Mills BD, Cain N, Mihalas S, Lahvis GP, Lattal KM, Mitchell SH, David S V., Fryer JD, Nigg JT, Fair D a. 2014. Large-scale topology and the default mode network in the mouse connectome. *Proc Natl Acad Sci* **111**. doi:10.1073/pnas.1404346111

Sugar J, Witter MP, van Strien NM, Cappaert NLM. 2011. The Retrosplenial Cortex: Intrinsic Connectivity and Connections with the (Para)Hippocampal Region in the Rat. An Interactive Connectome. *Front Neuroinform* **5**. doi:10.3389/fninf.2011.00007

Sutherland GR, McNaughton B. 2000. Memory trace reactivation in hippocampal and neocortical neuronal ensembles. *Curr Opin Neurobiol*. doi:10.1016/S0959-4388(00)00079-9

Sutherland RJ, Lehmann H. 2011. Alternative conceptions of memory consolidation and the role of the hippocampus at the systems level in rodents. *Curr Opin Neurobiol* **21**:446–451. doi:10.1016/J.CONB.2011.04.007

Sutherland RJ, Sparks FT, Lehmann H. 2010. Hippocampus and retrograde amnesia in the rat model: A modest proposal for the situation of systems consolidation. *Neuropsychologia* **48**:2357–2369. doi:10.1016/J.NEUROPSYCHOLOGIA.2010.04.015

Tang W, Jadhav SP. 2019. Sharp-wave ripples as a signature of hippocampal-prefrontal

reactivation for memory during sleep and waking states. *Neurobiol Learn Mem* **160**:11–20. doi:10.1016/j.nlm.2018.01.002

Tang W, Shin JD, Frank LM, Jadhav SP. 2017. Hippocampal-prefrontal reactivation during learning is stronger in awake compared with sleep states. *J Neurosci* **37**:11789–11805. doi:10.1523/JNEUROSCI.2291-17.2017

Tatsuno M, Malek S, Kalvi L, Ponce-Alvarez A, Ali K, Euston DR, Gruen S, McNaughton BL. 2020. Memory reactivation in rat medial prefrontal cortex occurs in a subtype of cortical UP state during slow-wave sleep. *Philos Trans R Soc B Biol Sci* **375**:20190227. doi:10.1098/rstb.2019.0227

Teyler T J, DiScenna P. 1986. The hippocampal memory indexing theory. *Behav Neurosci* **100**:147–54.

Teyler Timothy J., DiScenna P. 1986. The hippocampal memory indexing theory. *Behav Neurosci* **100**:147–154. doi:10.1037/0735-7044.100.2.147

Teyler TJ, Rudy JW. 2007. The hippocampal indexing theory and episodic memory: Updating the index. *Hippocampus* **17**:1158–1169. doi:10.1002/hipo.20350

van de Ven GM, Trouche S, McNamara CG, Allen K, Dupret D. 2016. Hippocampal Offline Reactivation Consolidates Recently Formed Cell Assembly Patterns during Sharp Wave-Ripples. *Neuron* **92**:968–974. doi:10.1016/j.neuron.2016.10.020

Van Groen T, Wyss JM. 2003. Connections of the retrosplenial granular b cortex in the rat. *J Comp Neurol* **463**:249–263. doi:10.1002/cne.10757

Wang D V, Ikemoto S. 2016. Coordinated Interaction between Hippocampal Sharp-Wave Ripples and Anterior Cingulate Unit Activity. *J Neurosci* **36**:10663–10672. doi:10.1523/JNEUROSCI.1042-16.2016

Wheeler AL, Teixeira CM, Wang AH, Xiong X, Kovacevic N, Lerch JP, McIntosh AR, Parkinson J, Frankland PW. 2013. Identification of a Functional Connectome for Long-Term Fear Memory in Mice. *PLOS Comput Biol* **9**:e1002853. doi:10.1371/JOURNAL.PCBI.1002853

Wilber AA, Skelin I, Wu W, McNaughton BL. 2017. Laminar Organization of Encoding and Memory Reactivation in the Parietal Cortex. *Neuron* **95**:1406-1419.e5. doi:10.1016/J.NEURON.2017.08.033

Wilson MA, McNaughton BL. 1994. Reactivation of hippocampal ensemble memories during sleep. *Science* **265**:676–9.

Winocur G, Moscovitch M. 2011. Memory Transformation and Systems Consolidation. *J Int Neuropsychol Soc* **17**:766–780. doi:10.1017/S1355617711000683

Wolansky T, Clement E a, Peters SR, Palczak M a, Dickson CT. 2006. Hippocampal slow oscillation: a novel EEG state and its coordination with ongoing neocortical activity. *J Neurosci* **26**:6213–6229. doi:10.1523/JNEUROSCI.5594-05.2006

Wu C-T, Haggerty D, Kemere C, Ji D. 2017. Hippocampal awake replay in fear memory

retrieval. *Nat Neurosci*. doi:10.1038/nn.4507

Wu X, Foster DJ. 2014. Hippocampal replay captures the unique topological structure of a novel environment. *J Neurosci* **34**:6459–69. doi:10.1523/JNEUROSCI.3414-13.2014

Wyass JM, Van Groen T. 1992. Connections between the retrosplenial cortex and the hippocampal formation in the rat: A review. *Hippocampus* **2**:1–11. doi:10.1002/hipo.450020102

Xie Y, Chan AW, McGirr A, Xue S, Xiao D, Zeng H, Murphy TH. 2016a. Resolution of High-Frequency Mesoscale Intracortical Maps Using the Genetically Encoded Glutamate Sensor iGluSnFR. *J Neurosci* **36**:1261–72. doi:10.1523/JNEUROSCI.2744-15.2016

Xie Y, Chan AW, McGirr A, Xue S, Xiao D, Zeng H, Murphy TH. 2016b. Resolution of High-Frequency Mesoscale Intracortical Maps Using the Genetically Encoded Glutamate Sensor iGluSnFR. *J Neurosci* **36**:1261–72. doi:10.1523/JNEUROSCI.2744-15.2016

Xu H, Baracskay P, O'Neill J, Csicsvari J. 2019. Assembly Responses of Hippocampal CA1 Place Cells Predict Learned Behavior in Goal-Directed Spatial Tasks on the Radial Eight-Arm Maze. *Neuron* **101**:119-132.e4. doi:10.1016/J.NEURON.2018.11.015

Yamawaki N, Li X, Lambot L, Ren LY, Radulovic J, Shepherd GMG. 2019. Long-range inhibitory intersection of a retrosplenial thalamocortical circuit by apical tuft-targeting CA1 neurons. *Nat Neurosci 2019 224* **22**:618–626. doi:10.1038/s41593-019-0355-x

Yang G, Lai CSW, Cichon J, Ma L, Li W, Gan W-B. 2014. Sleep promotes branch-specific formation of dendritic spines after learning. *Science* **344**:1173–8. doi:10.1126/science.1249098

Yüzgeç Ö, Prsa M, Zimmermann R, Huber D. 2018. Pupil Size Coupling to Cortical States Protects the Stability of Deep Sleep via Parasympathetic Modulation. *Curr Biol* **28**:392-400.e3. doi:10.1016/J.CUB.2017.12.049

Zingg B, Hintiryan H, Gou L, Song MY, Bay M, Bienkowski MS, Foster NN, Yamashita S, Bowman I, Toga AW, Dong HW. 2014. Neural networks of the mouse neocortex. *Cell* **156**:1096–1111. doi:10.1016/j.cell.2014.02.023